

**CHEMICAL HETEROGENEITY IN THE MANTLE FROM ARRAY  
OBSERVATIONS OF SHORT PERIOD P, PDIFF AND THEIR CODA**

Yan Xu, M.S.

An Abstract Presented to the Faculty of the Graduate  
School of Saint Louis University in Partial  
Fulfillment of the Requirements for the  
Degree of Doctor of Philosophy

2009

## Abstract

I apply array processing techniques to study the slowness and coda of P/Pdiff for 1,371 shallow earthquakes ( $< 200$  km) that occurred in Asia, South America, Tonga-Fiji, and Indonesia, and were recorded by the medium-aperture array, YKA, in Canada. The slowness analysis shows lateral variations in Earth structure at the base of the mantle across the north Pacific. I observe an Ultra-Low Velocity Zone (ULVZ) with up to 6% P velocity reduction in this region. The ULVZ can be explained as partial melt created by disaggregated mid-ocean ridge basalt (MORB) material that was subducted many millions of year ago beneath East Asia. It is currently being swept laterally towards the large, low shear velocity province (LLSVP) in the south-central Pacific by mantle convection currents. I also measure the coda decay rate (CDR) of the P/Pdiff energy. The radial variation of the CDR suggests that more fine-scale scatterers exist in the lowermost mantle compared to the mid-mantle. The CDR also has lateral variation, with the lowermost mantle beneath subduction regions having a smaller value (decays more slowly) than that corresponding to a nonsubduction region. The lateral variations of both the slowness and the CDRs at the base of the mantle support the hypothesis that mantle convection sweeps segregated subducted MORB laterally, due to the density and the melting temperature of the MORB, and it possibly accumulates to form the LLSVP. Synthetic simulations of Pdiff coda waves using a single scattering method also prefer the whole mantle scattering model with 1%  $dv/v$  in  $D''$ . The synthetic tests also constrain other important properties of the lowermost mantle. A non-smooth CMB is indicated which leads to topographical scattering, and  $Q_p$  for the lowermost mantle is estimated to be quite low at 150-250.

**CHEMICAL HETEROGENEITY IN THE MANTLE FROM ARRAY  
OBSERVATIONS OF SHORT PERIOD P, PDIFF AND THEIR CODA**

Yan Xu, M.S.

A Dissertation Presented to the Faculty of the Graduate  
School of Saint Louis University in Partial  
Fulfillment of the Requirements for the  
Degree of Doctor of Philosophy

2009

© Copyright by

Yan Xu

ALL RIGHTS RESERVED

2009

i

COMMITTEE IN CHARGE OF CANDIDACY:

|                     |   |
|---------------------|---|
| Associate Professor | Keith D. Koper,<br><u>Chairperson and Advisor</u> |
| Professor           | <u>Robert B. Herrmann</u>                         |
| Associate Professor | John Encarnación                                  |

## Dedication

This dissertation is dedicated to my parents and my husband.

## **Acknowledgments**

I would like to thank my advisor, Dr. Keith Koper, for his advise and support. He opened a door to the wonderful world of seismology to me, encouraged me to explore, and trained me to be professional in all directions.

I am grateful to Dr. David Crossley who gave me the opportunity to come to Saint Louis University. I would like to thank Dr. Rober Herrmann and Dr. Lupei Zhu for their help during my studying life in SLU and the suggestions for my research.

I thank Eric Haug and Bob Wurth for their help in computer techniques. I also thank Cynthia Wise and Laurie Hausmann for their office-related assistance.

I am so glad to meet and work with all graduate students. We come from different places, but we have the same dream. Because of you guys, my life here is full of fun.

I will send my greatest thanks to my parents, my husband, and my sister. Without their support and encouragement I could not have finished my studies.

## Table of Contents

|   |      |
|---|------|
| List of Figures . . . . .   | vii  |
| List of Tables . . . . .  | xiii |
| Chapter 1: Introduction . . . . .   | 1    |
| Chapter 2: Data . . . . .   | 6    |
| 2.1 Yellowknife Array . . . . .   | 7    |
| 2.2 Data sets . . . . .   | 7    |
| Chapter 3: Detection of a ULVZ at the Base of the Mantle Beneath the North-<br>west Pacific . . . . . | 11   |
| 3.1 Data and Methods . . . . .  | 12   |
| 3.2 Results . . . . .   | 15   |
| 3.3 Discussion and Conclusions . . . . .  | 18   |
| Chapter 4: Observation of the Coda Decay Rate . . . . .   | 22   |
| 4.1 Source Location of the P/Pdiff Coda . . . . .   | 22   |
| 4.1.1 The VESPA Process . . . . .   | 23   |
| 4.1.2 Sliding window analysis . . . . .   | 28   |
| 4.2 Coda Decay Rate (CDR) Measurement . . . . .   | 29   |
| 4.2.1 Radial Variation of CDR . . . . .   | 33   |
| 4.2.2 Lateral variation of CDR . . . . .  | 38   |
| 4.3 Amplitude of the P or Pdiff . . . . .   | 41   |
| Chapter 5: Synthetic Simulation and Modeling of Coda Waves . . . . .                                  | 43   |
| 5.1 Basics of Single Scattering Approach . . . . .  | 44   |
| 5.2 Incorporating Diffraction Into the Synthetic Codas . . . . .                                      | 46   |
| 5.3 Effect of PcP . . . . .   | 50   |
| 5.4 Effect of Voxel Size of Synthetic Codas . . . . .   | 51   |
| 5.5 Effect of Source Time Function . . . . .  | 52   |

|               |   |    |
|---------------|---|----|
| 5.6           | Effect of Q in the Lower Mantle . . . . .                 | 52 |
| Chapter 6:    | Forward Modeling of Observed P/Pdiff Coda Waves . . . . . | 55 |
| 6.1           | The Effect of CMB Topography . . . . .                    | 55 |
| 6.2           | Constraining Q in the Lowermost Mantle . . . . .          | 57 |
| 6.3           | Radial Extent of Heterogeneity . . . . .                  | 62 |
| 6.4           | Strength of the Scatterers in D'' . . . . .               | 65 |
| 6.5           | Preferred Model . . . . .                                 | 65 |
| Chapter 7:    | Conclusion . . . . .                                      | 69 |
| Appendix A:   | . . . . .   | 76 |
| References    | . . . . .   | 82 |
| Vita Auctoris | . . . . .   | 91 |

## List of Figures

|  |    |
|--|----|
| <p>Figure 1.1: Wave path and example synthetic seismograms of P and Pdiff at 90 and 110 deg respectively. The red triangle is the receiver and the red dot represents the source (modified from Edward Garnero, <a href="http://garnero.asu.edu">http://garnero.asu.edu</a>). . . . .</p>  | 4  |
| <p>Figure 2.1: Location of the Yellowknife array (red star). Pink triangles are major cities in Canada and the inset shows the array geometry. . . .</p>   | 9  |
| <p>Figure 2.2: (a) Distributions of the events used in this study. Blue stars are the events from Asia; ginger represent events from South America; green are Tonga-Fiji. Black stars are the events from Sumatra. The insert is the geometry of YKA. (b) Backazimuth and bottoming depth of all the data. The red line represents core-mantle boundary (CMB).</p> | 10 |
| <p>Figure 2.3: Pdiff legs (golden lines) along CMB for the events from Sumatra and Tonga data sets (green circles). Black triangle, YKA. . . . .</p>   | 10 |
| <p>Figure 3.1: (a) Example of the slowness and backazimuth detection using beam-packing method. The two circles from inside to outside represent the ray parameter of <math>PKiKP</math> and <math>P_{diff}</math> respectively. (b) The corresponding waveforms used for the slowness and backazimuth detection.</p>  | 15 |
| <p>Figure 3.2: The binned slowness observations (black dots) against the theoretical values from AK135 Earth model (red curve). . . . .</p>  | 16 |
| <p>Figure 3.3: <math>\delta V_p</math> variation at 2 Hz, and the location of ULVZ. . . . .</p>  | 19 |

|   |    |
|---|----|
| Figure 3.4: (a) Observed $P$ velocity variation against $P$ tomography models, MITP08 [Li <i>et al.</i> , 2008a], (b) temperature in the bottom 1000 km of the mantle [Trampert <i>et al.</i> , 2004], (c) perovskite anomaly at the bottom of the mantle [Trampert <i>et al.</i> , 2004], and (d) the observed ULVZ [Thorne and Garnero, 2004]. . . . .              | 21 |
| Figure 4.1: Example of traces used for the slantstack (VESPA) and sliding window analysis. . . . .  | 24 |
| Figure 4.2: Example vespagram of the Ms 6.7 earthquake that occurred on February 8, 1990 by fixing the backazimuth to the theoretical value of the P phase, 301.7 deg. . . . .  | 26 |
| Figure 4.3: Examples of binned vespagrams at 70 and 105 deg respectively. (a) The binned slowness vespagram and (c) the backazimuth residual vespagram at 70 deg. (b) The binned slowness vespagram and (d) the backazimuth residual vespagram at 105 deg. The white stars are the slowness or backazimuth residual with the biggest beam power at that time. . . . . | 27 |
| Figure 4.4: Example sliding window analysis of the Ms 6.7 earthquake that occurred on February 8, 1990 by fixing the backazimuth to the theoretical value of the P phase (301.7 deg). . . . .   | 30 |
| Figure 4.5: Binned slowness (a,b,c) and backazimuth residuals (d,e,f) from three different regions. The red line is the mean value of the binning, the gray area represents the $1\sigma$ standard deviation. . . . .   | 31 |
| Figure 4.6: Amplitude shapes for the events from Tonga-Fiji. . . . .  | 34 |
| Figure 4.7: Example of the coda decay rate measurement (a,b,c). Coda decay rate from three regions (d). Green: Tonga-Fiji; blue: Asia; brown: South America. The nominal core-mantle depth is 2891 km based on the AK135 Earth model. . . . .   | 36 |

|  |    |
|--|----|
| Figure 4.8: Sampling regions (orange line) in the lowermost mantle for the data from (a) South America, (b) Tonga-Fiji, (c) and Asia. The green dots are the event locations. The blue open circles are the paleo-subducted slabs in the lowermost mantle [Ricard <i>et al.</i> , 1993; Lithgow-Bertelloni and Richards, 1998]. The red open circle is the location of the Hawaii hotspot. . . . . | 37 |
| Figure 4.9: (a) Lateral variation of CDR. (b) The binned radiation pattern of all events from Sumatra-Andaman and Tonga-Fiji. (c) The CDR from the deep events occurring in Sumatra-Andaman subduction zone. The thick black line along the ray path represents the sampling region in the lowermost mantle. The brown dots are the paleo-subducted slabs. . . . .                                 | 40 |
| Figure 4.10: The change of the expected amplitude of P/Pdiff as a function of distance. . . . .  | 42 |
| Figure 5.1: Example of the synthetic envelope of the vertical component of P and its coda at 76 deg using the single scattering method described in the text. The time is relative to the theoretical P arrival time. . .  | 47 |
| Figure 5.2: Synthetic seismograms for the P/Pdiff phase from the frequency-wavenumber method [Herrmann, 2007] using the AK135 earth model.   | 48 |
| Figure 5.3: Example of the effect of the half distance. The black curves are the synthetics at 100 deg. Red curves are the synthetics at 110 deg.  | 49 |
| Figure 5.4: Example of synthetics at 78 deg, bottom panel, and 98 deg, top panel. Black: the synthetics without PcP phase. Red: the synthetics with PcP phase. . . . .   | 50 |
| Figure 5.5: Example of synthetics at 78 deg using different voxel size. Black: $100^3 km^3$ . Green: $50^3 km^3$ . Red: $200^3 km^3$ . . . . .   | 51 |

|   |    |
|---|----|
| Figure 5.6: Example of synthetics at 78 deg. Solid line, synthetic without source time function. Dashed line, synthetic convolved with a 5 sec long triangle source time function. Dotted line, synthetic convolved with an 8 sec long trapezoidal source time function. . . . .  | 53 |
| Figure 5.7: Synthetics at 110 deg from different attenuation model of D". Solid line: ak135. Thick line: ak135.chQ9. . . . .  | 54 |
| Figure 6.1: Bottom: The effect of the half distance using the whole mantle scattering model and the AK135 Earth model. Top: Example of the synthetics at 110 deg using different half distance. Black: 10 deg half distance. Green: 4.0 deg half distance. Red: 2.0 deg half distance. . .  | 58 |
| Figure 6.2: Bottom: CDR using different half distance: 2.0 deg half distance, dotted line; 1.0 deg half distance, dash line; 0.5 deg half distance, solid line; 0.1 deg half distance, dash-dot line. Top: Example of the synthetics at 110 deg using different half distance. Black: 2.0 deg half distance. Blue: 1.0 deg half distance. Red: 0.5 deg half distance. Green: 0.1 deg half distance. . . . . | 60 |
| Figure 6.3: Bottom: CDR using different Q model for the lowermost mantle, Table 6.2. Top: Example of the synthetics at 110 deg using different Q model. Black: ak135. Blue: ak135.chQ9. Red: ak135.chQ11. Green: ak135.chQ10. . . . .   | 63 |
| Figure 6.4: Detecting the distribution of scatterers by using the 2.0 half distance and the earth model with high attenuation in D", chQ13, by matching the CDR observations. . . . .   | 64 |

|  |    |
|--|----|
| Figure 6.5: Bottom: CDRs uses different strength of the scatterers in D'', left. Expected amplitude, right. Top: Synthetic envelopes from different strength of the scatterers in D''. Red: 3% velocity perturbation in the D''. Blue: 0.5% velocity perturbation. Green: 0.05% velocity perturbation. Black: 1% perturbation. . . . .   | 66 |
| Figure 6.6: The best fit using 2.0 deg half distance, chQ13 attenuation model, Table 6.2, and the whole mantle scattering with $dv/v$ equals 1%. . . . .   | 68 |
| Figure A.1: $\delta V_p$ variation at 1 Hz, and the location of ULVZ. . . . .  | 77 |
| Figure A.2: Observed $P$ velocity variation against $P$ tomography model, MITP08 [ <i>Li et al.</i> , 2008a](a), temperature in the bottom 1000 km of the mantle [ <i>Trampert et al.</i> , 2004](b), perovskite anomaly at the bottom of the mantle [ <i>Trampert et al.</i> , 2004](c), and observed ULVZ [ <i>Thorne and Garnero</i> , 2004](d) at 1 Hz. . . . .  | 78 |
| Figure A.3: $P$ tomography models and observed lateral velocity variation in the bottom 20 km. BDP00 [ <i>Becker and Boschi</i> , 2002], HWE97P [ <i>van der Hilst et al.</i> , 1997], KH00P [ <i>Kárason and van der Hilst</i> , 2001], MK12WM13P [ <i>Su and Dziewonski</i> , 1997], PB10L18 [ <i>Masters et al.</i> , 2000], SPRD6P [ <i>Ishii and Tromp</i> , 2004], MITP08 [ <i>Li et al.</i> , 2008a], Zhao09 [ <i>Zhao</i> , 2008]. . . . . | 79 |
| Figure A.4: $S$ tomography models. sprd6s [ <i>Ishii and Tromp</i> , 2004], mk12wm13s [ <i>Su and Dziewonski</i> , 1997], s20a [ <i>Ekström and Dziewonski</i> , 1998], s20rts [ <i>Ritsema and van Heijst</i> , 2000], sb10l18 [ <i>Masters et al.</i> , 2000], sb4118 [ <i>Masters et al.</i> , 1999], saw24b16 [ <i>Mégnin and Romanowicz</i> , 2000], grand [ <i>Grand et al.</i> , 1997], s362d1 [ <i>Gu et al.</i> , 2001]. . . . .          | 80 |

Figure A.5: *P* tomography models. BDP00 [*Becker and Boschi, 2002*],  
HWE97P [*van der Hilst et al., 1997*], KH00P [*Kárason and van der  
Hilst, 2001*], MK12WM13P [*Su and Dziewonski, 1997*], PB10L18 [*Mas-  
ters et al., 2000*], SPRD6P [*Ishii and Tromp, 2004*], MITP08 [*Li et al.,  
2008a*], Zhao09 [*Zhao, 2008*]. . . . . 81

## List of Tables

|   |    |
|---|----|
| Table 2.1: Coordinates for all Yellowknife Array stations. . . . .            | 8  |
| Table 5.1: Q models in D'' used to explore the effect of the attenuation. . . | 53 |
| Table 6.1: Three scattering models. . . . .                                   | 59 |
| Table 6.2: Five Q models of D''. . . . .                                      | 62 |

## Chapter 1: Introduction

Seismology is one of the best tools for studying the current structure of the Earth, especially the deep Earth. The deepest borehole reaches a depth of 12 km, and compared to the radius of the Earth (6371 km) this only samples the very shallowest part of the Earth. Additionally, this is only the view for one hole from which it is hard to interpret the 3D Earth. Therefore, since we cannot directly sample the interior of the Earth, we can choose to analyze seismic waves generated by passive or active sources, and traveling through the body of the Earth, to learn about the properties of the Earth.

A lot of seismic imaging is focused on the Earth's mantle. This is the highly viscous layer beneath the brittle and rocky crust. The viscous mantle plays an important role in plate tectonics. Owing to convection in the mantle, the tectonic plates floating atop it are carried away or towards one another. Understanding plate tectonics is important for understanding earthquakes. However, precisely how mantle convection works we still do not know. Seismologists provide images of the mantle at different scales, large-scale from tomography and small-scale from scattered energy, through analyzing seismograms. In addition to images, seismologists also derive the physical parameters of the mantle. The structural images and constraints help us to understand the dynamics of the mantle and the history of the Earth.

Traditional mantle imaging is based on travel-time tomography, free oscillation and surface wave tomography, and waveform tomography. These methods have been successful at imaging long-wavelength structures. For instance, tomography has shown slabs sinking back into the mantle [*van der Hilst et al.*, 1991, 1997; *Kárason and van der Hilst*, 2000; *Li et al.*, 2006, 2008b], and plumes rising from various depths within the mantle [*Bijwaard et al.*, 1998; *Mégnin and Romanowicz*, 2000;

*Zhao, 2004; Lei and Zhao, 2006; Nolet et al., 2007*].

A second type of seismic imaging uses scattered energy to map the short-wavelength features. Examples of this are the fine-scale heterogeneity studies of the coda and precursors to teleseismic body waves [*Bataille and Flatté, 1988; Cormier, 1995; Tono and Yomogida, 1996; Bataille and Lund, 1996; Cormier, 1999; Hedlin and Shearer, 2000; Margerin and Nolet, 2003a*]. This approach is complementary to tomography because even though tomography studies show the heterogeneity of the mantle, they only reveal long wavelength ( $\sim 100$  km) information, which is not enough to constrain patterns of mantle convection. Images of fine-scale ( $\sim 10$  km) heterogeneity, such as disaggregated slabs, can help constrain the mixing efficiency of mantle flow and shed light on the chemical evolution of the planet.

The precise depth distribution of fine-scale heterogeneity in the mantle remains open for debate. Some studies suggest the heterogeneities are concentrated at or near the CMB [*Cleary and Haddon, 1972; Haddon and Cleary, 1974; Bataille and Flatté, 1988; Bataille et al., 1990; Tono and Yomogida, 1996, 1997; Wen and Helmberger, 1998a; Thomas et al., 1999, 2002*]. Other studies propose a more uniform distribution of the small-scale heterogeneities throughout the mantle [*Doornbos and Vlaar, 1973; Hedlin et al., 1997; Shearer et al., 1998; Cormier, 1999; Hedlin and Shearer, 2000; Earle and Shearer, 2001; Hedlin and Shearer, 2002; Margerin and Nolet, 2003a*].

In this work, I specifically address what can be learned about mantle heterogeneity from the coda waves of Pdiff. Pdiff is compressional energy diffracted along the core-mantle boundary (CMB) that is recorded at distances of about  $98^\circ - 130^\circ$ . Coda of Pdiff, the slowly-decaying energy train following the main phase, is thought to be scattered energy generated by the heterogeneities somewhere in the mantle. Fig 1.1 is a cartoon showing the Pdiff wave path and an example of

synthetic seismograms of P and Pdiff, at 90 and 110 degrees respectively.

Previous Pdiff coda studies give conflicting interpretations on the location of the heterogenites that create Pdiff coda waves. By reviewing previous scattering studies in the lowermost mantle *Bataille et al.* [1990] suggested the long tail following the  $P_{diff}$  arrival is caused by scattering at the CMB. *Bataille and Lund* [1996] used a simple multiple scattering theory to interpret the short-period Pdiff and concluded that the long tail of Pdiff originates in D". *Tono and Yomogida* [1996] studied 15 deep events ( $h > 300$  km) at distances of 103 to 120 deg, and pointed out that the coda of the Pdiff is caused by deep earth scattering. *Tono and Yomogida* [1997] studied the 1994 Bolivian deep earthquake recorded at distances from 100 to 122 deg. They filtered the IRIS broad-band and New Zealand short-period data to frequencies of 1 to 2 Hz. Then through a study of the particle motion and spectra, they concluded that the Pdiff coda waves are generated by heterogeneities in the deep mantle. However, *Earle and Shearer* [2001] suggested an alternative interpretation, a whole mantle scattering model on the basis of stacking 924 Pdiff envelopes from global broadband seismograms.

There are two goals of this study, both related to the issue of fine-scale mantle heterogeneities. One goal is to try to identify the average radial distribution of the heterogeneities. A second, which also is an intriguing question, is to map out any lateral variation of scatterers in the lower mantle. The large-scale velocity anomaly at the CMB has a degree two pattern, with two large low-shear-velocity provinces beneath the central Pacific ocean and Africa, each surrounded by fast velocity regions. The anticorrelation between S wave velocity and bulk sound speed in the lowermost mantle [*Masters et al.*, 2000] can be reconciled with the phase transition from perovskite to post-perovskite. Thermally-equilibrated subducted MORB is denser than the surrounding mantle at all depths except between 660 and 720 km [*Hirose et al.*, 2005]. At the lowermost mantle the density contrast can reach 3%

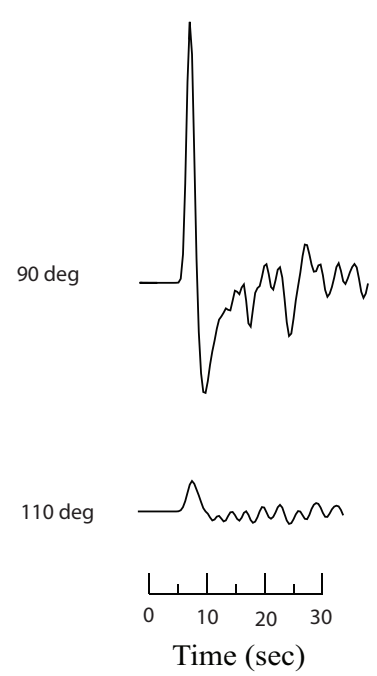
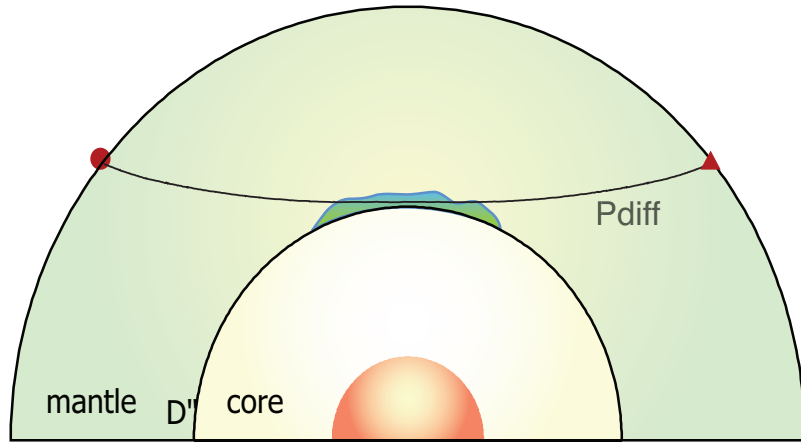


Figure 1.1: Wave path and example synthetic seismograms of P and Pdiff at 90 and 110 deg respectively. The red triangle is the receiver and the red dot represents the source (modified from Edward Garnero, <http://garnero.asu.edu>).

which makes the MORB material stable in the D". Stable MORB material is separated, swept by the mantle flow, and accumulated in piles beneath the upwellings at the base of the mantle suggested by the geodynamical simulations [Christensen and Hofmann, 1994; McNamara and Zhong, 2004; Nakagawa and Tackley, 2005]. Another goal of this study is to try to address the lateral variation of the fine-scale heterogeneities at the base of the mantle beneath the northwest Pacific. The study of the radial and lateral variations of the fine-scale scatterers can help constrain the geodynamical simulations, and allow us to get a better understanding of 3D mantle convection.

My thesis is organized in the following manner. After this introduction, the second chapter describes the data set used for this study. The third chapter describes properties of the direct Pdiff phase. Studying this will help us understand the coda properties and also provide independent constraints on P velocity from 800 km depth to the core-mantle boundary. This chapter has been submitted to Geophysical Research Letters (GRL) as a standalone paper. In the fourth chapter, after studying the direct phase, I analyze the coda of the P/Pdiff recorded by the medium aperture array, YKA, to detect the radial and lateral variations in coda properties. In Chapter 5, I use a single scattering method to forward model the coda decay rate measurements. Through the modeling, I get constraints on the distribution and the strength of the scatterers, intrinsic attenuation in the lowermost mantle, and possible topography on the CMB. The final chapter provides a summary of the conclusions reached in this work.

## Chapter 2: Data

Previous studies of  $P_{diff}$  and its coda were done using broadband records from the IRIS (Incorporated Research Institutions for Seismology) GSN (Global Seismographic Network) [Bataille *et al.*, 1990; Bataille and Lund, 1996; Tono and Yomogida, 1996, 1997; Earle and Shearer, 2001]. As the information provided by the data is integrated along the whole ray path, it is not easy to separate the deep mantle anomalies from the anomalies created by shallow structures, beneath the event and station. Another limitation of the GSN data is station bias. Owing to the station location, the structure beneath the station and the surrounding environment,  $P_{diff}$  and its coda may appear with low signal-to-noise ratio from moderate magnitude seismic events.

In this study, I use the Yellowknife Seismic Array (YKA) to build a data set of teleseismic P and Pdiff waves. YKA has an aperture of 20 km and so is very sensitive to teleseismic P waves around 1 Hz. It has a uniform geological environment at all seismometer sites, and efficient array techniques can be applied to enhance weak signals. Specifically, a good tool to enhance the signal-to-noise ratio is stacking individual traces of the array stations into a beam. Arrays also have a second advantage that makes them suitable for studying small-scale structure in Earth's interior, i.e. the slowness and backazimuth constraints from array data processing. Owing to these two advantages, arrays have been widely used in the studies of the Earth's interior [Hedlin *et al.*, 1997; Rost and Weber, 2002; Koper *et al.*, 2003; Koper and Pyle, 2004; Koper *et al.*, 2004; Rost *et al.*, 2006a; Leyton and Koper, 2007a].

## 2.1 Yellowknife Array

The 1958 Geneva Disarmament Conference promoted research on the discrimination between earthquakes and underground explosions. Since that time, a number of seismic arrays were built to support this mission by increasing signal-to-noise ratios. The Yellowknife Array (YKA) was built in 1962 and sponsored by the UK Atomic Energy Authority. YKA lies in the solid Precambrian crystalline rock of the stable Canadian Shield, with a quiet environment far away from coastlines and major urban areas (Figure 2.1). The gross crustal structure beneath the array was shown to be horizontal [Weichert and Whitham, 1969], and the site has very little dependence on azimuth [Corbishley, 1970] and small slowness error [Manchee and Weichert, 1968]. The recent slowness-azimuth station correction study for the IMS seismic network [Bondár *et al.*, 1999] also shows that YKA is a good array with only small biases on slowness and azimuth measurements. YKA has 18 vertical-component, short-period instruments with equal interstation distance of 2.5 km, forming two orthogonal lines oriented north-south and east-west (see inset of Figure 2.1 for array geometry and Table 2.1 detailed information of YKA).

## 2.2 Data sets

We obtained waveforms from 1,371 earthquakes with magnitude 5.7 to 7.9 Mw, in the distance range 50 deg to 120 deg, over the years 1990 to 2006, using the CNDC AutoDRM (Figure 2.2). Figure 2.2(b) shows the sampled regions illustrated as a function of backazimuth and bottoming depth. This figure clearly shows the capability of studying the radial and lateral variation of mantle heterogeneities with our data set. One group of data is from Asia, Tonga-Fiji, and South America. Even though the data in this group are from different regions and will bring out the regional differences of the heterogeneity, the most important

Table 2.1: Coordinates for all Yellowknife Array stations.

| station | latitude | longitude | elevation<br>(m) | sample<br>rate | channel<br>component |
|---------|----------|-----------|------------------|----------------|----------------------|
| YKB1    | 62.4024  | -114.6029 | 1725             | 20             | SHZ                  |
| YKB2    | 62.42479 | -114.6054 | 1805             | 20             | SHZ                  |
| YKB3    | 62.44862 | -114.6052 | 1876             | 20             | SHZ                  |
| YKB4    | 62.47107 | -114.6049 | 1929             | 20             | SHZ                  |
| YKB6    | 62.51652 | -114.6050 | 2026             | 20             | SHZ                  |
| YKB7    | 62.53901 | -114.6053 | 2044             | 20             | SHZ                  |
| YKB8    | 62.56184 | -114.6047 | 1979             | 20             | SHZ                  |
| YKB9    | 62.58295 | -114.6039 | 2130             | 20             | SHZ                  |
| YKB0    | 62.60593 | -114.6050 | 2216             | 20             | SHZ                  |
| YKR1    | 62.49273 | -114.9456 | 1700             | 20             | SHZ                  |
| YKR2    | 62.49278 | -114.8964 | 1750             | 20             | SHZ                  |
| YKR3    | 62.49298 | -114.8477 | 1768             | 20             | SHZ                  |
| YKR4    | 62.49274 | -114.7995 | 1734             | 20             | SHZ                  |
| YKR5    | 62.49328 | -114.7499 | 1829             | 20             | SHZ                  |
| YKR6    | 62.49332 | -114.7014 | 1922             | 20             | SHZ                  |
| YKR7    | 62.49337 | -114.6537 | 1989             | 20             | SHZ                  |
| YKR8    | 62.49323 | -114.6053 | 1967             | 20             | SHZ                  |
| YKR9    | 62.49314 | -114.5557 | 2011             | 20             | SHZ                  |

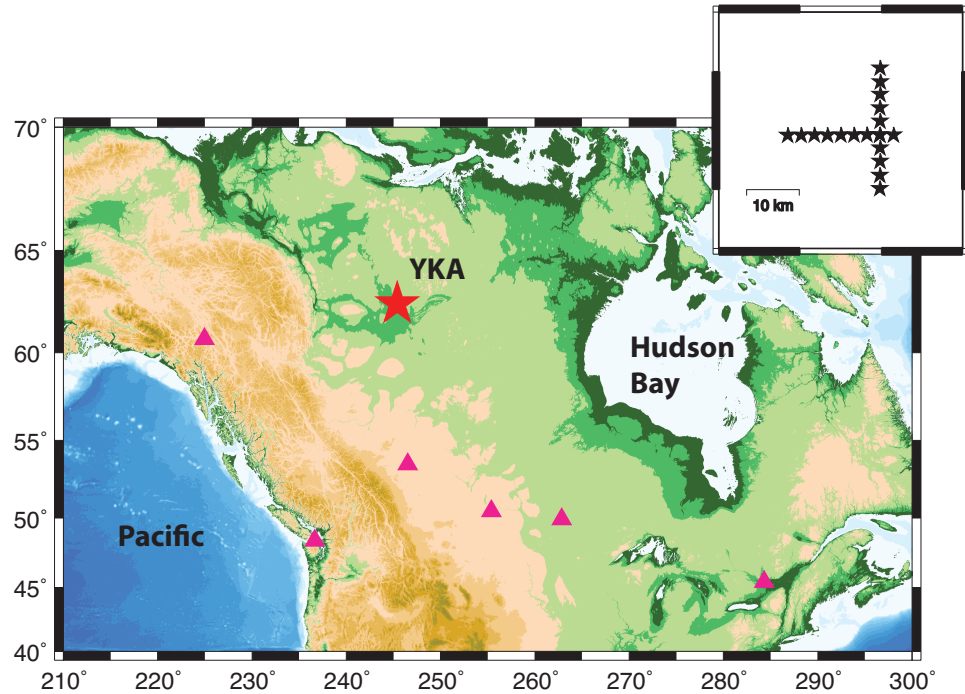


Figure 2.1: Location of the Yellowknife array (red star). Pink triangles are major cities in Canada and the inset shows the array geometry.

information that will be brought out is the radial distribution of the heterogeneities as the sampling depth varies from the bottom of the transition zone to the core-mantle boundary with very little change in backazimuth. Another group of data is combined by the events from Sumatra-Andaman and Tonga-Fiji as they sample the bottom of the mantle with backazimuth changing from 220 deg to 340 deg; this will give us the lateral variation of the heterogeneities in the lowermost mantle. Figure 2.3 shows in map view the sampling region along the CMB of the second group of data. They cover a wide region along the CMB from the Northwest Pacific, a current subduction region, to the northern edge of the Pacific large low shear velocity province (LLSVP). This data set might give clues on the distribution of mid-ocean ridge basalt (MORB) material in D''.

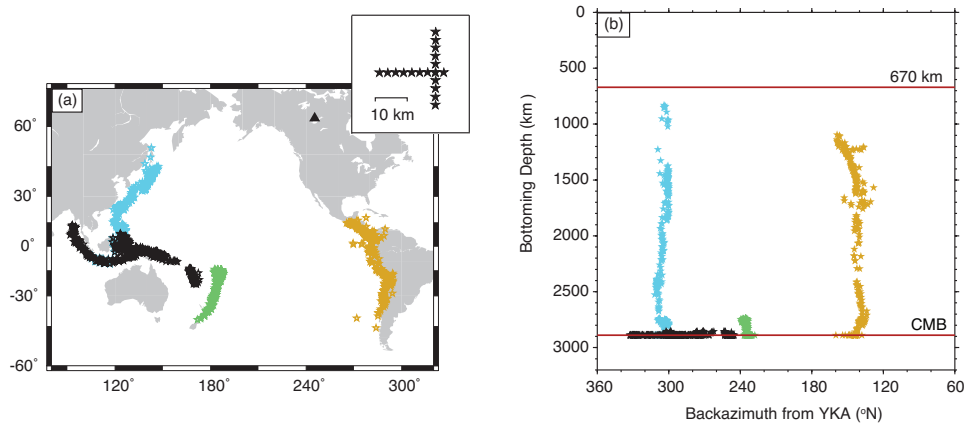


Figure 2.2: (a) Distributions of the events used in this study. Blue stars are the events from Asia; ginger represent events from South America; green are Tonga-Fiji. Black stars are the events from Sumatra. The insert is the geometry of YKA. (b) Backazimuth and bottoming depth of all the data. The red line represents core-mantle boundary (CMB).

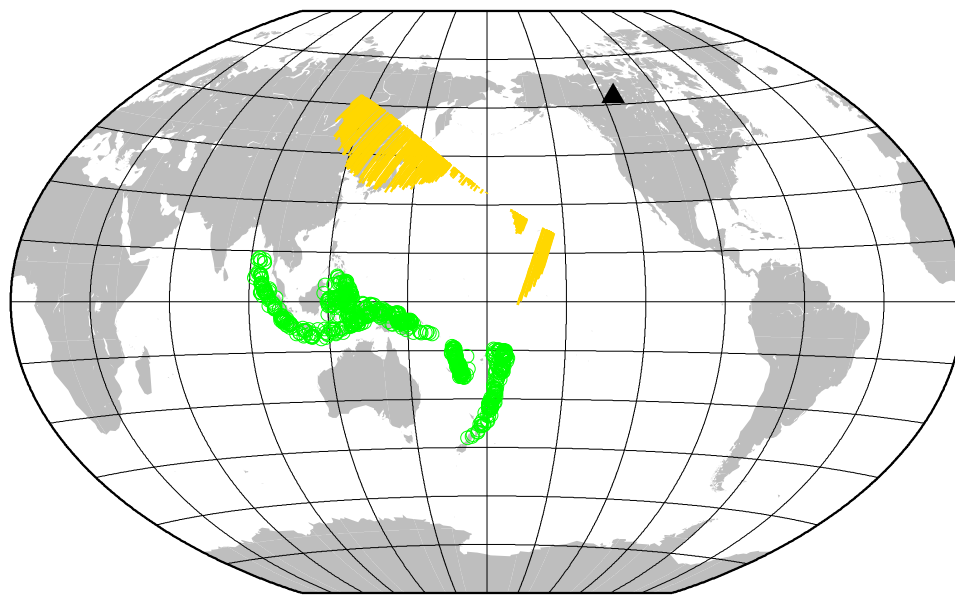


Figure 2.3: Pdiff legs (golden lines) along CMB for the events from Sumatra and Tonga data sets (green circles). Black triangle, YKA.

### Chapter 3: Detection of a ULVZ at the Base of the Mantle Beneath the Northwest Pacific

There is a large contrast in the chemical composition and physical properties across the Earth's core-mantle boundary (CMB), with silicates and oxides on the solid mantle side and an iron-nickel alloy on the fluid outer core side. The magnitude of this change separates (to first order) the dynamics of the mantle from the dynamics of the core, and the lowermost mantle (D'') acts as a thermal boundary layer. Over the last three decades, seismic studies have revealed a rich variety of structural features in D'' that rival in complexity the lithosphere, the mantle's upper thermal boundary layer. Seismic features observed in D'' include discontinuities in  $S$  and  $P$  velocities, extreme lateral gradients in  $S$  and  $P$  velocities, anisotropy, small wavelength scatterers, and topography on the CMB itself (see *Garnero and McNamara* [2008] for a recent review).

Of particular interest are regions just above the CMB that are designated as Ultra-Low-Velocity Zones (ULVZs) and have reductions in  $P$  and  $S$  velocity as high as 10% and 30% respectively [*Garnero et al.*, 1993; *Mori and Helmberger*, 1995; *Garnero and Helmberger*, 1995; *Revenaugh and Meyer*, 1997; *Garnero and Helmberger*, 1998; *Garnero et al.*, 1998; *Wen and Helmberger*, 1998a; *Rost and Revenaugh*, 2003; *Thorne et al.*, 2004; *Rost et al.*, 2005; *Avants et al.*, 2006]. Because ULVZs are localized and thin they are not apparent in long-wavelength, tomographic models of the mantle and instead they have been detected and studied mainly with waveform modeling of seismic phases such as  $ScP$  and  $SP_{diff}KS$  [*Rost and Revenaugh*, 2003; *Thorne et al.*, 2004]. Owing to the extreme velocity reductions, ULVZs have been interpreted as partial melt [*Williams and Garnero*, 1996; *Berryman*, 2000; *Akins et al.*, 2004] and so just like the lithosphere there may be magmatic systems operating in D''.

One model for the origin of ULVZs suggests that chemically distinct pieces of subducted oceanic crust sink all the way down to D” where they act to reduce the melting temperature of the ambient material and create partial melt [*Hirose et al.*, 2005, 1999]. Geodynamical simulations have shown that MORB material can maintain its negative buoyancy but still be swept around laterally by convection currents [*Christensen and Hofmann*, 1994; *McNamara and Zhong*, 2004; *Nakagawa and Tackley*, 2005]. In particular, there are geodynamical reasons to believe that the MORB material might preferentially accumulate along the borders of the chemically distinct, large low shear velocity provinces (LLSVPs) that have been detected by seismic tomography [*Masters et al.*, 2000; *Grand*, 2002].

There does appear to be a rough correlation between the location of ULVZs and the borders of LLSVPs [*Wen and Helmberger*, 1998a, b; *Thorne and Garnero*, 2004; *Rost et al.*, 2005, 2006a; *Lay et al.*, 2006; *Avants et al.*, 2006], but seismic mapping of D” is not yet complete enough to be conclusive. In this work we extend the mapping of ULVZ structure to a previously unsampled portion of D” beneath the North Pacific. As a probe we use ray parameters of short-period  $P$  waves that have diffracted around Earth’s core ( $P_{diff}$ ). Previous studies of long period  $P_{diff}$  “apparent” ray parameters have been effective at mapping out large-scale variations in D” velocities [*Wyssession and Okal*, 1989; *Wyssession et al.*, 1992, 1998], and the increased frequencies considered in this study lead to even higher resolution. Although our approach is not as precise as waveform modeling, it is capable of resolving the sharp lateral gradient in seismic velocity that is indicative of a ULVZ.

### 3.1 Data and Methods

Our data set consists of 1,371 shallow earthquakes (depth  $< 200$  km) that occurred at distances of 50 to 120 degrees from the Yellowknife Seismic Array (YKA) between the years of 1990 and 2006 (Figure 2.2a). We only used events that

were large enough to have a centroid moment tensor (CMT) solution and the minimum magnitude in our data set is  $5.7 M_w$ . The earthquakes occurred primarily in the subduction zones of the circum-Pacific region and the corresponding dip-slip focal mechanisms led to impulsive, coherent P waves for our distance range. This experimental geometry allows us to examine the depth variation in  $P$  velocity in the lower mantle along two fixed azimuthal corridors, as well as the lateral variation in  $P$  velocity at the base of the mantle in the North Pacific (Figure 2.2b). About half of our data set, 612 events, occurred in the Sumatra-Andaman subduction zone. All the YKA seismograms were obtained using the autodrm of the Canadian National Data Center (<http://earthquakescanada.nrcan.gc.ca/stndon/AutoDRM/index-eng.php>).

The Yellowknife seismic array has 18 vertical-component, short-period seismometers with equal interstation distances of 2.5 km. The sensors are arranged in two orthogonal lines oriented north-south and east-west (Figure 2.2a). This geometry makes YKA very effective at observing teleseismic  $P$  waves at frequencies near 1 Hz [Rost *et al.*, 2006b]. The array is sited in old, cratonic lithosphere and has uniform geologic structure and elevation across the seismometer sites; therefore, slownesses and backazimuths can be estimated at YKA with high accuracy without bias [Manchee and Weichert, 1968; Corbishley, 1970; Bondár *et al.*, 1999].

One of the key advantages in using an array is the ability to measure the vector slowness of an incoming phase [Rost and Thomas, 2002]. For body waves at high frequency, the magnitude of the slowness vector is interpreted as the ray parameter,  $p$ , where  $p = dT/d\Delta = R/V$ , and  $T$  is the travel time,  $\Delta$  is the distance,  $R$  is the normalized radius at the turning or bottoming point of the ray, and  $V$  is the corresponding velocity at  $R$ . Therefore, in the limit of infinite frequency a ray parameter observation can be directly mapped to the seismic wavespeed at the ray's turning point. At finite frequencies the sensitivity of  $p$  is broadened both laterally

and in depth and it is not simply a point measurement; however, the peak sensitivity is still at the ray-theoretical turning point, and for the short periods considered in this study (near 1 s), the smearing is not severe.

To infer the slowness of  $P$  waves recorded at YKA we used a time-domain beam-packing method appropriate for transient signals. A 14 s window of data around the  $P/P_{diff}$  arrival, 4 sec before the theoretical arrival time and 10 sec after that, was extracted from each element. The waveforms were detrended, tapered, resampled from 0.05 s to 0.01 s, and filtered with a 3-pole Butterworth bandpass with corner frequencies of 0.67 and 1.33 Hz or 1.33 and 2.67 Hz. Phase stack weighted beams of order 3 were calculated across a 2D Cartesian slowness grid with spacing of 0.05 s/deg in both directions. Power was calculated as the mean square value of the beam, and the grid point with the highest power was selected as the observed slowness vector.

Figure 3.1a shows an example of our slowness inference technique for a typical earthquake in the data set. The waveforms (Figure 3.1b) were taken from a 6.7  $M_s$  event that occurred in Asia, where the Philippine sea plate subducted beneath the Sunda plate, at a distance of 94.8° and a depth of 31 km on February 8, 1990. The maximum energy comes from the northwest, backazimuth of 302°, with a ray parameter of 4.36 s/deg. Expected values are 301.7° and 4.552 s/deg respectively. We used a bootstrap technique [*Koper and Pyle, 2004*] to estimate the error of the observations, and found standard errors of 0.07 s/deg in slowness and 0.9° in backazimuth. The cross shape in Figure 3.1a, is caused by the geometry of the array (Figure 2.1) and can be mitigated by using variable weights during beamformation; however, for the purposes of this study, in which large, coherent, earthquake-generated body waves are being studied, there is no advantage to using a more sophisticated technique.

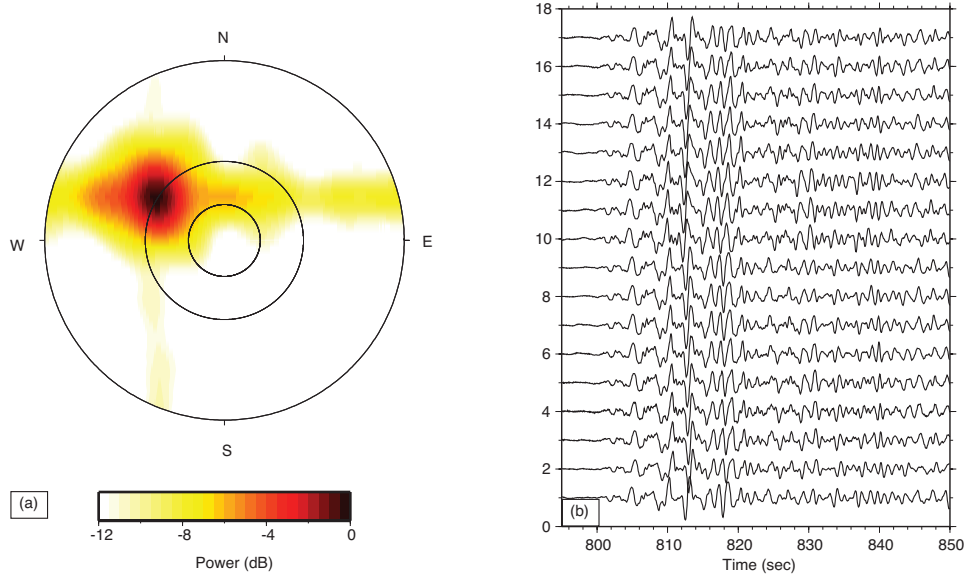


Figure 3.1: (a) Example of the slowness and backazimuth detection using beam-packing method. The two circles from inside to outside represent the ray parameter of  $PKiKP$  and  $P_{diff}$  respectively. (b) The corresponding waveforms used for the slowness and backazimuth detection.

### 3.2 Results

The ray parameters of the  $P/P_{diff}$  phases for all 1371 events are presented in Figure 3.2. The individual values are binned in terms of bottoming depth (calculated using AK135 [Kennett *et al.*, 1995]) and so variations in source depth are naturally accounted for. Each bin is 50 km wide and the number of data included in each bin is shown in the top panel. The ray parameters show the expected decrease with depth and are well-matched by the AK135 predictions. The overall mean ray parameter residual is between -0.54 and 0.19 s/deg. The magnitude of this residual is slightly larger than what is expected for site effects, indicating some variation from AK135 along these paths. However, the strongly negative residuals at the shallowest depths are not robust because of the small number of observations in those bins.

As shown in Figure 3.2 the largest concentration of our observations occurs with bottoming depths in the lower 200 km of the mantle. There are enough data in

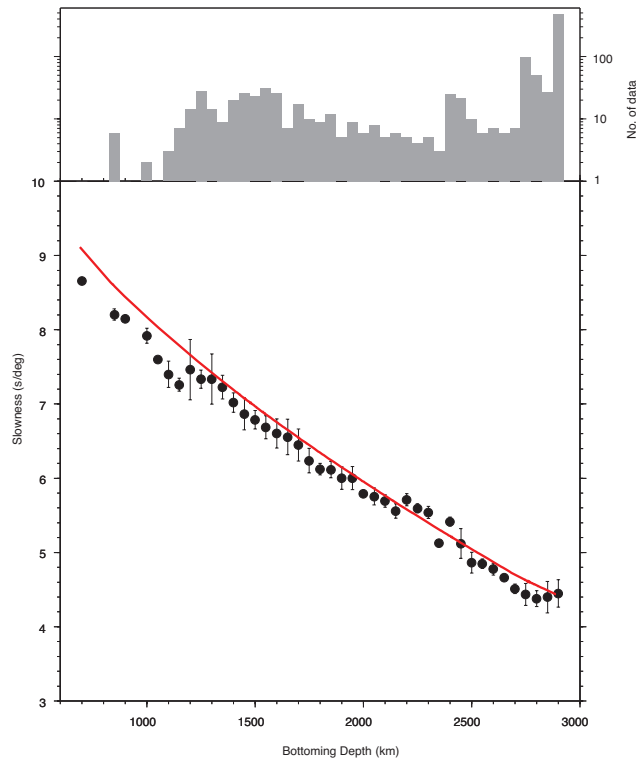


Figure 3.2: The binned slowness observations (black dots) against the theoretical values from AK135 Earth model (red curve).

these bottom four bins to examine robustly any lateral variations in  $P$  velocity. We present this in Figure 3.3 in which we average the slowness observations at 2 Hz, bottoming just 50 km above the CMB which also is the last dot in Figure 3.2, in 5 deg bins of backazimuth, going from Tonga-Fiji in the east to Sumatra-Andaman in the west, corresponding to a range of backazimuths of 230 to 330. The number of observations in each bin are shown by the histogram on the top and the slowness anomalies are converted to velocity anomalies using the relationship,

$$V = (R_{CMB} * 111.19)/(p * R_{Earth}).$$

From 230 to 290 deg in backazimuth  $\delta V_p$  gradually decreases from 3% to -6 %. The mean value is negative in this region which can be attributed to a relatively high temperature region. Continuing to larger backazimuths,  $\delta V_p$  changes its gradually decreasing trend and rises to a value above or around zero after 295 deg. The mean  $\delta V_p$  change is slightly higher than zero between 295 to 330 deg which can be attributed to a relatively low temperature region. The change in  $\delta V_p$  between the two regimes is about 6%, from -6% at the edge of high-temperature region to 0% at the edge of low-temperature region. The magnitude of this change is huge, especially considering it occurs in a narrow region, about 10 deg or 600 km. This huge and sharp velocity change is a hallmark of ULVZs and is hard to explain as purely thermal because diffusion would tend to smear the anomaly over a broad area. However, a chemical or phase anomaly could have such a sharp change.

Our observations also show a frequency dependent  $P$  velocity lateral variation. Figure A.1 in Appendix A shows the velocity variation using the same event, the same data processing, but filtering centered at 1 Hz compared to Figure 3.3. The  $\delta V_p$  are not exactly the same for 2 Hz and 1 Hz. Still, the two frequency bands show the same pattern: the obviously sharp change of  $P$  velocity, and the declining trend in the high temperature region from east to west. However, the  $P$  velocity anomalies for 1 Hz only reach 3% reduction at the edge of high temperature region.

We think the different sensitivity to depth could be the reason for the difference. Although we bin the same data which represent the velocity in the bottom 50 km of the mantle, different centering frequencies can lead to different sensitivity in depth. We see that the higher the frequency, the deeper sensitivity. Since 2 Hz is more sensitive to the bottom than 1 Hz and the ULVZ exists right above the CMB, 1 Hz averages the velocity variation over a relatively large depth and shows a smaller velocity reduction comparing with 2 Hz.

### 3.3 Discussion and Conclusions

The 6% lateral change in P velocity over 600 km horizontally that we observe in the lowermost mantle beneath the North Pacific is much stronger than what appears in global tomographic models of the mantle. We illustrate this in Figure 3.4 by plotting our results on top of the a recent tomographic image [*Li et al.*, 2008a] in which velocities vary by only +/- 1.5% relative to the background model. Other tomographic models have similar dynamic range and we plot our results against seven other recent P models in Appendix A. An interesting observation that is apparent in both Figure 3.4 and many of the models in the supplement is that the ULVZ identified here appears to correlate with a boundary between a low velocity province to the north and east and a high velocity province to the south and west.

The location of the ULVZ and the apparent boundary in P velocity is well north of the Pacific LLSVP that has been identified in several recent tomographic models. We show this in Appendix A by plotting the lowermost mantle layer for nine recent tomographic models. However, the anticorrelation in P and S velocities in the lower mantle is well accepted and indeed in one of the strongest pieces of evidence for pervasive chemical heterogeneity in D". One of the most useful studies in this regard in that of *Trampert et al.*, in which density and shear and bulk sounds models are jointly determined and the chemical and thermal anomaly components

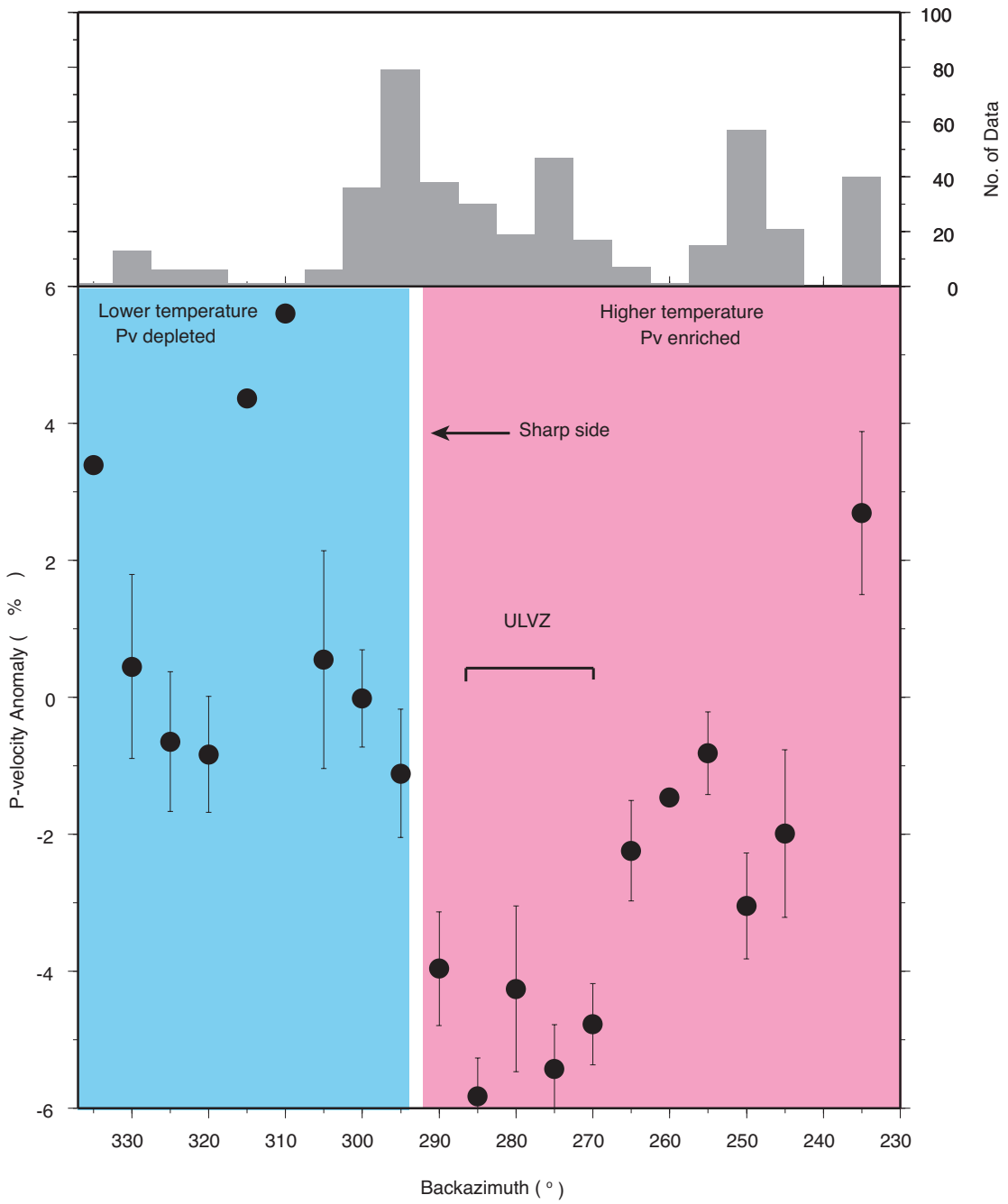


Figure 3.3:  $\delta V_p$  variation at 2 Hz, and the location of ULVZ.

are explicitly separated. Plotting our results against these images, which are admittedly long-wavelength and averaged through the lower 1000 km of the mantle, we see that our ULVZ occurs nicely at the boundary between a compositionally and thermally distinct patches of the lower mantle. Those characteristics can all be seen in the 1 Hz variation, Figure A.2 in Appendix A.

We note that not only the ULVZ observed in this study but also many previously observed ULVZs tend to occur around the bounds of the compositional distinct pile of material beneath most of the Pacific. Our observations extend to the southeast of the ULVZ that has previously been observed near Kamchatka, filling out perhaps the northern boundary of the blob. Our interpretation then is that MORB, transported into the deep mantle beneath East Asia [*Ricard et al.*, 1993; *Lithgow-Bertelloni and Richards*, 1998], has been pushed towards the chemically distinct blob beneath the Pacific. The interaction of the MORB with the warmer and enriched blob material then leads to partial melt and the formation of our ULVZ.

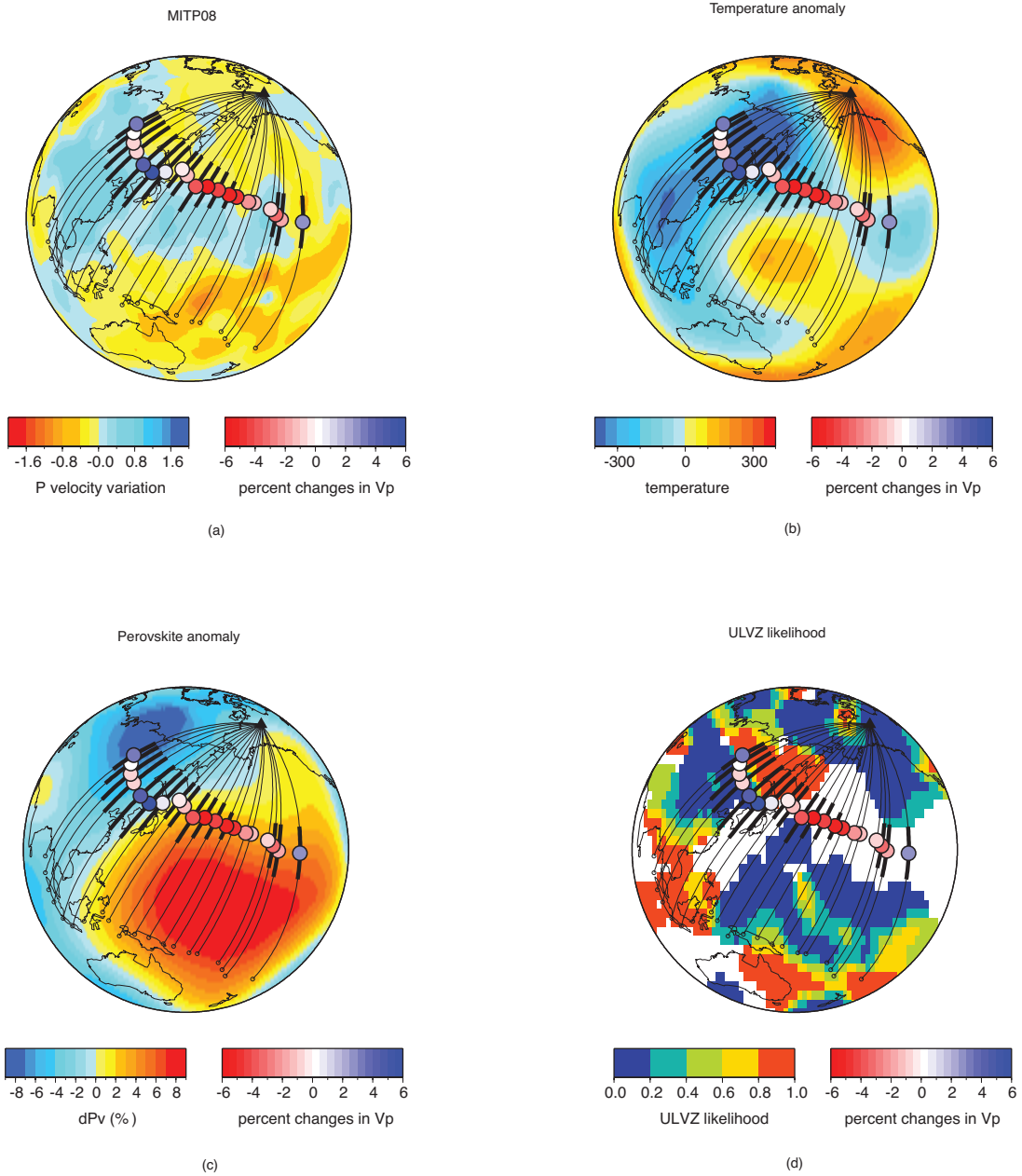


Figure 3.4: (a) Observed  $P$  velocity variation against  $P$  tomography models, MITP08 [Li *et al.*, 2008a], (b) temperature in the bottom 1000 km of the mantle [Trampert *et al.*, 2004], (c) perovskite anomaly at the bottom of the mantle [Trampert *et al.*, 2004], and (d) the observed ULVZ [Thorne and Garnero, 2004].

## Chapter 4: Observation of the Coda Decay Rate

In chapter 3, I applied array techniques on the first arrival to detect lateral velocity perturbations and heterogeneity in the lowermost mantle beneath the north Pacific. On the seismogram after the main phase, the subsequent slowly-decaying energy train also includes important information about the Earth. *Aki* [1969] first studied this wave train, called “coda”, and proposed that the scattered waves are created from randomly distributed small-scale inhomogeneities in the earth. These high-frequency scattered waves are interesting due to their sensitivity to the fine-scale heterogeneities within the Earth. In this chapter I study the P/Pdiff coda waves in order to reveal the hidden story of the heterogeneous mantle.

As the coda waves are not regular plane waves travelling directly from the epicenter [*Aki et al.*, 1958; *Aki and Tsujiura*, 1959; *Aki and Chouet*, 1975], it is difficult to numerically simulate coda waves. Because of this, waveform analysis is unsuitable for the study of coda waves, and instead the coda energy or envelope is commonly observed and modeled. The energy level of the coda does not require accurate waveform information, and is a good and proper tool to study the scattered waves. Here I apply array techniques to observe the beam power of the P/Pdiff coda, then by comparing the coda power from different regions and different depths I constrain the lateral and radial distribution of fine-scale heterogeneities in the mantle.

### 4.1 Source Location of the P/Pdiff Coda

Since the coda waves are generated by randomly distributed scatterers, whether they come from the same sagittal plane (great-circle ray-path direction) as the first-arriving P/Pdiff phase is the first question I have to check. In order to examine the direction from which the coda waves arrive, I infer the slowness and

backazimuth using two array techniques. If the coda waves have the same slowness and backazimuth as the main phase, it implies the coda waves are created mainly near the source or along the path, and not dominantly at the receiver.

#### 4.1.1 The VESPA Process

*Davies et al.* [1971] defined the first version of the VELOCITY SPectrum Analysis (VESPA) process. It can detect one of the two unknown parameters of an incoming wave, horizontal slowness and backazimuth, by inputting one to the beamforming equation and plotting the beam energy as a function of the other parameter and time. For Nth root stacking the relevant equations are:

$$B'(t) = \frac{1}{M} \sum_{j=1}^M |b_j(t + \tau_j)|^{1/N} \cdot \text{sign} b_j(t) \quad (4.1)$$

$$B(t) = |B'(t)|^N \cdot \text{sign}\{B'(t)\} \quad (4.2)$$

$$\tau_j = \frac{-x_j \cdot \sin \Phi - y_j \cdot \cos \Phi}{s} \quad (4.3)$$

where  $B(t)$  is the final beam,  $B'(t)$  is an intermediate stack,  $b_j(t + \tau_j)$  is the amplitude of the  $j^{\text{th}}$  trace,  $\tau_j$  is the time shift for the  $j^{\text{th}}$  trace,  $x_j$  and  $y_j$  are the coordinates of the  $j^{\text{th}}$  seismometer to the reference point,  $\Phi$  is the backazimuth,  $s$  is the horizontal slowness,  $N$  is the stacking exponent, and  $M$  is the number of seismometers.

First, I filter the data with a three-pole Butterworth band-pass filter with corner frequencies of 1.67 and 2.33 Hz. I use the theoretical backazimuth or the slowness of the main phase as the input, and the second order phase weighted stack method to form the beam. The phase weighted stacking can efficiently increase the signal-to-noise ratio and cause less phase distortion than Nth root stacking [*Rost and Thomas, 2002; Schimmel and Paulssen, 1997*]. Fig 4.2 is an example of a

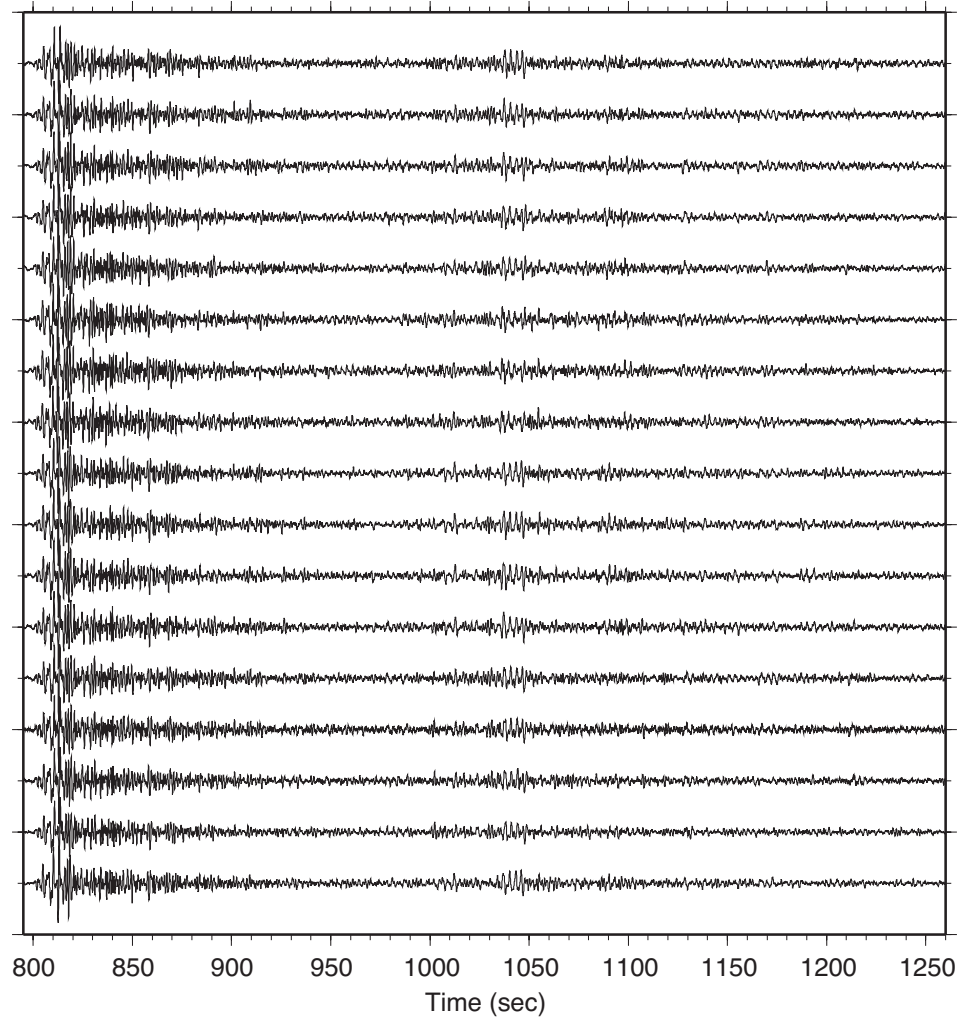


Figure 4.1: Example of traces used for the slantstack (VESPA) and sliding window analysis.

vespagram search for the slowness using the same event in Chapter 3. In the slowness vespagram we can clearly see three phases separated by different slowness, P, PP, and PKiKP. The coda of the P phase is another noticeable feature in the vespagram because of its long-lasting time and high energy.

I process all the coda using the VESPA process to get slowness and backazimuth vespagrams. Then I bin the slowness observations and the backazimuth residuals, subtracting the theoretical backazimuth from the observation, in 5 deg bins. One thing that needs to be pointed out is that I only use shallow events ( $< 200$  km) as we do not want the depth phase and its coda to contaminate the observations.

Fig 4.3 is an example of binning vespagrams for South American events in the 70-75 (Fig 4.3 a,c) and 105-110 (Fig 4.3 b,d) deg distance bins. The white dot represents the maximum value at its corresponding time. For the smaller distance bin (70-75 deg), we can clearly see the P phase at 0 sec and its coda lasts for about 150 sec with the same slowness. Then, another phase appears with larger slowness. This phase is the P wave bouncing once at the surface, PP. The backazimuth residuals are essentially zero for the P coda. At the larger distance (105-110 deg), we can see the same feature of the stacked slowness and backazimuth residual except that PP shows up at a reasonably later time. The two distance bins have another common feature that is the gradually increasing slowness right before the arrival time of PP. Those gradual increasing slowness energies are precursors to PP. Therefore, I find that the existence of the PP precursors contaminates the observation of P/Pdiff coda, in agreement previous studies [*Tono and Yomogida, 1997; Earle and Shearer, 2001*].

However, the vespagram will miscalculate the slowness if an incorrect backazimuth is given [*Rost and Weber, 2001; Rost and Thomas, 2002*]. Thus, when we do the VESPA process we depend on the theoretical value from a 1D earth model which is not always accurate for the real Earth. Therefore, we apply another technique, sliding window slowness analysis, which will search for the two unknowns

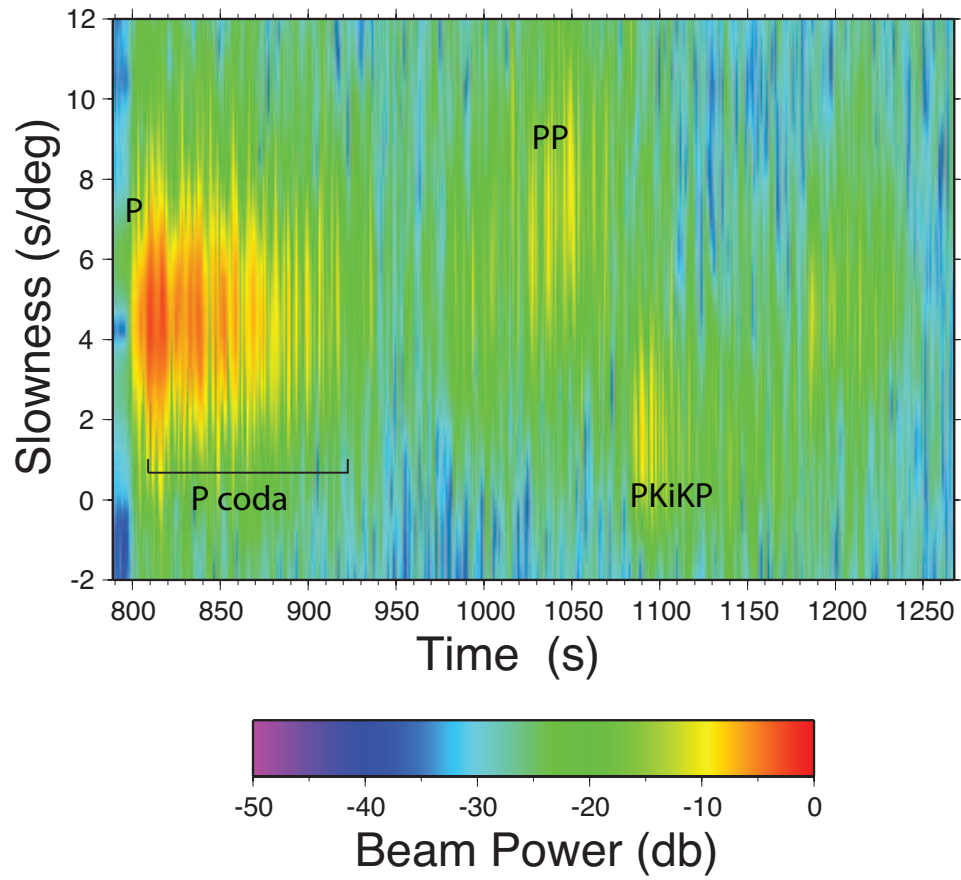


Figure 4.2: Example vespagram of the Ms 6.7 earthquake that occurred on February 8, 1990 by fixing the backazimuth to the theoretical value of the P phase, 301.7 deg.

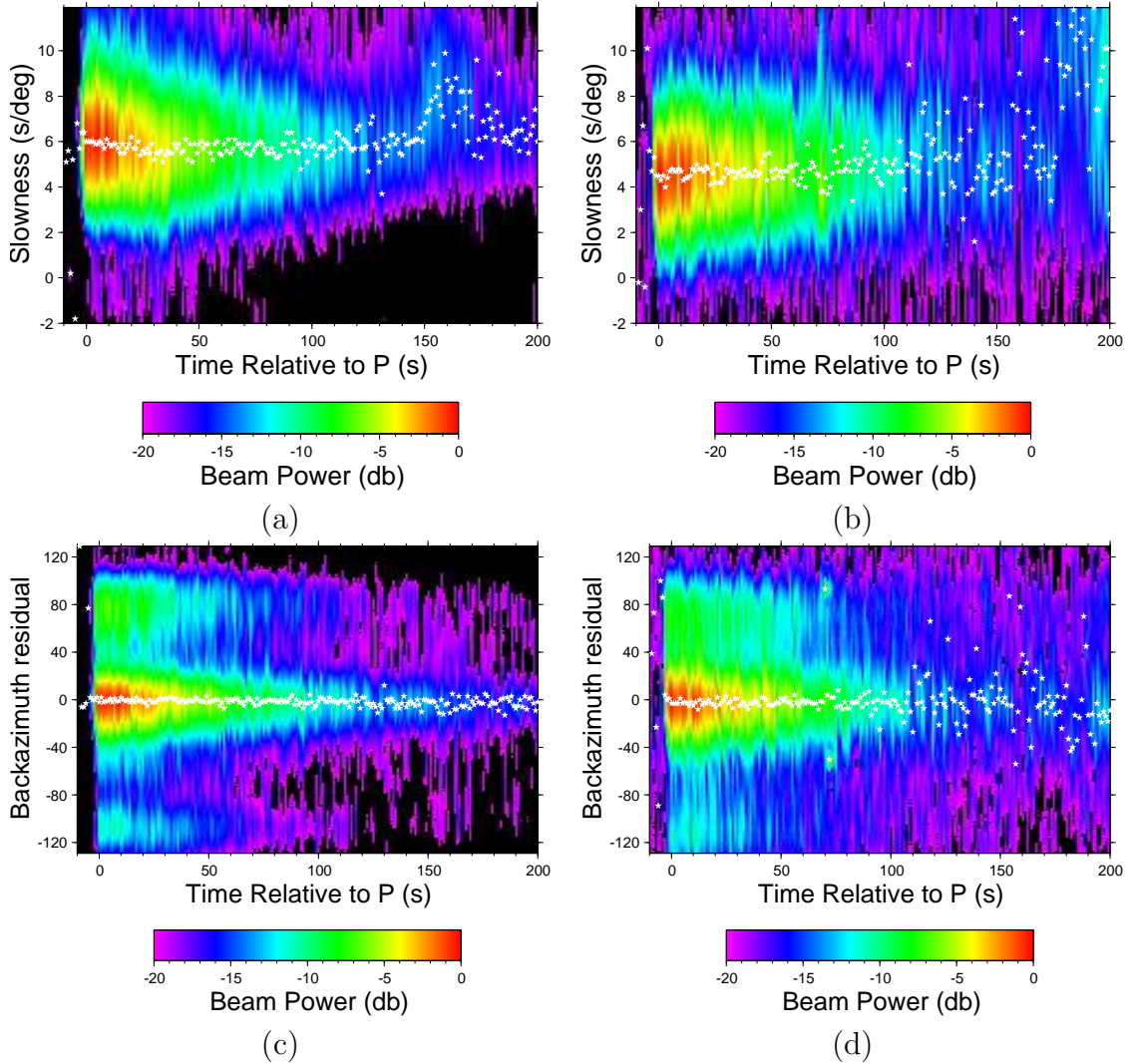


Figure 4.3: Examples of binned vespagrams at 70 and 105 deg respectively. (a) The binned slowness vespagram and (c) the backazimuth residual vespagram at 70 deg. (b) The binned slowness vespagram and (d) the backazimuth residual vespagram at 105 deg. The white stars are the slowness or backazimuth residual with the biggest beam power at that time.

simultaneously, to check whether the coda of P/Pdiff is arriving from similar directions as the direct arrivals.

#### 4.1.2 Sliding window analysis

*Rost and Weber* [2001] first used the sliding window analysis to detect Earth structure at 200 km depth. Sliding window analysis does not have the problem that a vespagram does because it searches for the slowness and backazimuth simultaneously in a certain time window. The correct slowness and backazimuth combination will give the biggest energy in the time window. Next the time window is shifted with a constant step. The same search for the slowness and backazimuth is applied in the new time window. This method has been successfully used in PKiKP coda analysis [*Koper et al.*, 2004; *Leyton et al.*, 2005; *Leyton and Koper*, 2007a].

I choose a time window width of 2 s, a shifting step of 1 s, and a three-pole Butterworth bandpass filter centered at 2 Hz as the analysis parameters. As *Rost and Weber* [2001] mentioned, the width of the time window should be wide enough to include phases traveling over the array, and narrow enough to avoid too much noise. *Leyton and Koper* [2007a] pointed out that the window should only include a single phase and its coda, therefore the 2 s window is a suitable width for YKA to study P or Pdiff and its coda at 2 Hz. In each time window I choose linear stacking to measure the beam power (root mean square amplitude) as it maintains the original waveform information, which is used in the following study. Fig 4.4 is an example of the sliding window analysis for the same event that was used before. In addition to the backazimuth and slowness, the sliding window analysis also gives the beam power and coherence [*Schimmel and Paulssen*, 1997] as a function of time. When the P wave arrives, the beam power and coherence shoots up. For the P coda part, the beam power gradually decays due to the attenuation and loss of coherence relative to the main phase. However, the coda has the same slowness and

backazimuth as the main phase as shown in the flat part of the top two panels.

After applying the sliding window analysis to all of the data, I bin the observations in 5 deg arc distance bins as before. When I bin the slowness and backazimuth residuals, I also consider the coherence. If the coherence is less than 0.5 in its corresponding time window, the value is not included. Because we set this coherence criteria, some distance bins do not have values before the P/Pdiff arrival time, e.g. Fig 4.5(b), the stacked slownesses with error bounds for South America do not have a value before 0 sec relative to P arrival time for distances between 75 to 80 deg. As we set coherence criteria when we do the stacking, some distances don't have value before the P or Pdiff theoretical arrival time. Three regions show that the coda of P or Pdiff has the same slowness as the main phase. Fig 4.5(d,e,f) are the stacked backazimuth residuals which are zero at almost all the distances. The results of the sliding window analysis confirm that the codas of P/Pdiff come from nearly the same direction as the main phase.

## 4.2 Coda Decay Rate (CDR) Measurement

In comparing a moonquake with an earthquake, one outstanding difference is that the moonquake has an extremely long tail (coda) owing to the strong heterogeneity and low absorption in the Moon. This example tells us that we can, through study of the decay behavior of coda, learn about the heterogeneity inside the Earth. In fact, this fine-scale heterogeneity can only be revealed by studying the high frequency waves, such as coda.

Sliding window analysis provides the beam power of P or Pdiff and its coda as a function of time. This sort of envelope analysis has been widely adopted to the study of scattered energy [Hedlin *et al.*, 1997; Koper *et al.*, 2004; Vidale and Earle, 2005; Leyton and Koper, 2007a]. In order to treat every event equally, I first remove the background noise from each beam power function by choosing 100 sec to 30 sec

### Sliding Window Slowness Estimation

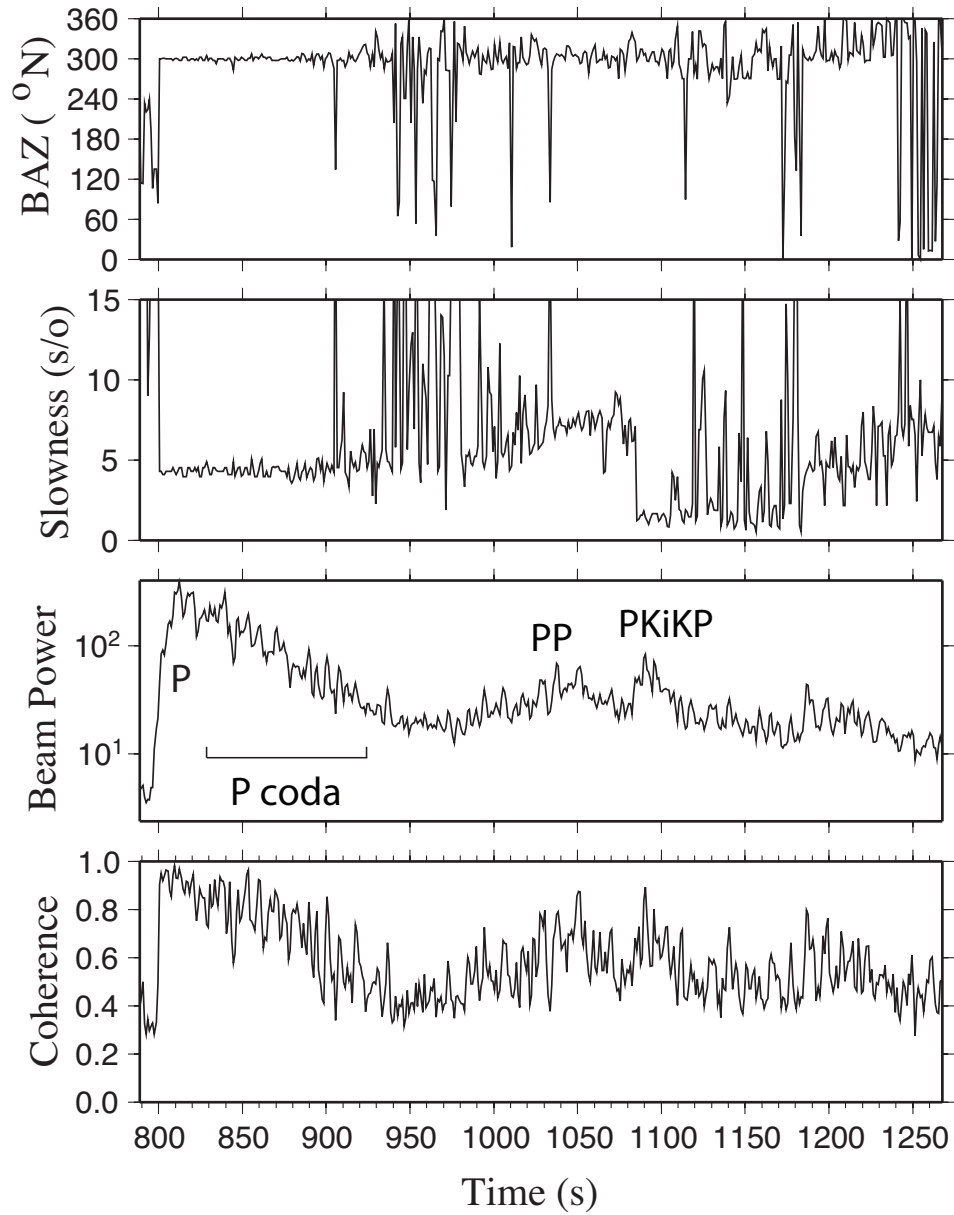


Figure 4.4: Example sliding window analysis of the Ms 6.7 earthquake that occurred on February 8, 1990 by fixing the backazimuth to the theoretical value of the P phase (301.7 deg).

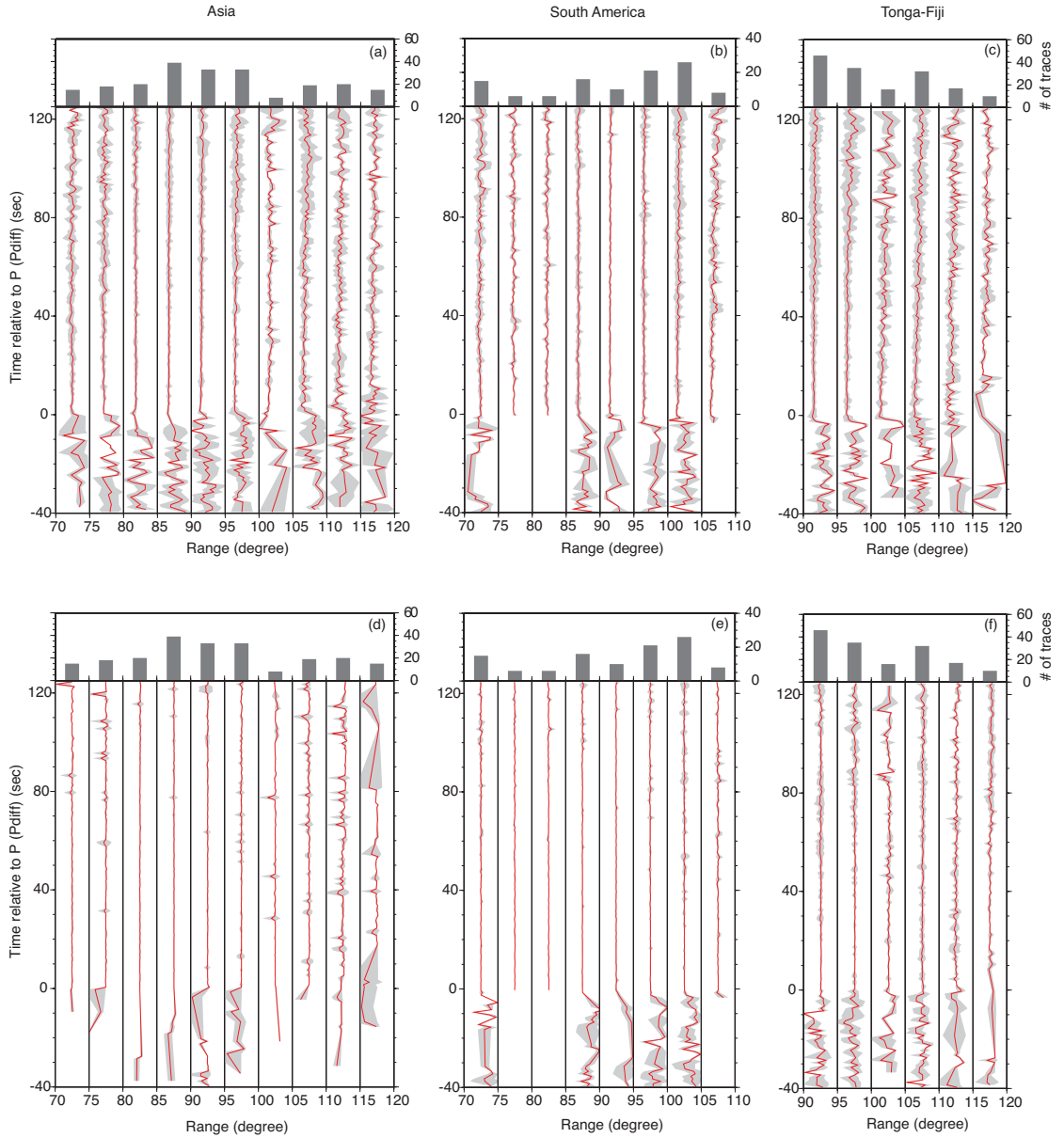


Figure 4.5: Binned slowness (a,b,c) and backazimuth residuals (d,e,f) from three different regions. The red line is the mean value of the binning, the gray area represents the  $1\sigma$  standard deviation.

before the P or Pdiff onset as the background noise window to get the average value, similar to procedures used in previous studies [Earle and Shearer, 2001; Xu and Vidale, 2003]. By assuming  $A^2 = N^2 + S^2$ , where  $A$  is the total amplitude,  $N$  is the noise, I can estimate  $S^2$ , where  $S$  represents the signal. Next, I correct the P and PP amplitude by the predicted radiation pattern to get rid of amplitude differences related to the focal mechanism; then, I normalize the beam power by its corrected PP amplitude, which has a decreasing amplitude with increasing distance and no effect of triplication [Earle and Shearer, 2001]. After the envelope preparation, I stack the noise-removed normalized beam power to eliminate the effects of variations of magnitude, source parameters, and depth. The CDR estimate means fitting the curve of the stacked beam power.

Energy density is proportional to the velocity squared [Sato and Fehler, 1998]

$$E(x, t) \propto v^2(x, t; f). \quad (4.4)$$

The coda energy can be expressed as exponential decay

$$E(t) = v^2(t) = A \cdot \exp(-2\pi Q_c^{-1} ft) \quad (4.5)$$

$$2\ln(v(t)) = \ln(A) - 2\pi Q_c^{-1} ft \quad (4.6)$$

$$\ln(v(t)) = C - \pi Q_c^{-1} ft \quad (4.7)$$

where  $C \equiv \frac{1}{2}\ln(A)$  which is a constant, and  $Q_c^{-1}f$  is called the CDR. Leyton and Koper [2007a] successfully applied this method to measure  $Q_c$ , the inverse of the CDR, of the PKiKP coda. In logarithmic space the relationship between velocity and the CDR becomes linear and can be solved using a least squares technique [Menke, 1989].

Even after eliminating the effects from differences in magnitude, focal mechanism, and depth by stacking, one source effect still will exist, which is the

source duration. As the earthquakes I chose have magnitudes between 5.7 and 7.9, I begin fitting the coda energy curve 20 sec after the P or Pdiff to avoid source time complexities. The total fitting window is 100 sec long since PP arrives at 150 sec after the P arrival in our shortest distance bin, 70 deg, which guarantees no PP precursor contamination.

#### 4.2.1 Radial Variation of CDR

Fig 2.2 shows that the data from Asia, South America, and Tonga-Fiji have a very good depth coverage. For each of those regions we bin the denoised and normalized beam power in 2 deg bins of epicentral distance, then fit the curve using a least squares approach. Binning multiple events with different focal mechanisms can mitigate the effect of radiation pattern as shown in previous studies [*Earle and Shearer, 2001*]. Fig 4.6 shows how the amplitude changes with increasing distance using the binned results from Tonga-Fiji. The trend of an impulsive first arrival followed by gradually decaying energy smoothly changes to the shape of an emergent first arrival followed by gradually increasing energy from 90 deg to 118 deg. This smooth shape change suggests that the radiation pattern does not significantly affect the observations.

Fig 4.7 gives an example of the curve fitting for three different geographical regions in the same distance bin. The time starts 40 sec before the theoretical P or Pdiff arrival time, and the coda level is shown in log scale. The red line is the fitted result. CDR, its error, and the residual are given on the figure. The energy level is pretty low before the zero sec, relative to the P or Pdiff arrival time, then as P or Pdiff arrives the energy shoots up before gradually decaying. At the same distance, the three regions' fitted results show different coda decay behavior. The Tonga-Fiji path has the biggest CDR, 0.009811, and the South American path has the smallest CDR, 0.005706. Fig 4.7(c), for Tonga-Fiji, and Fig 4.7(a), for South America,

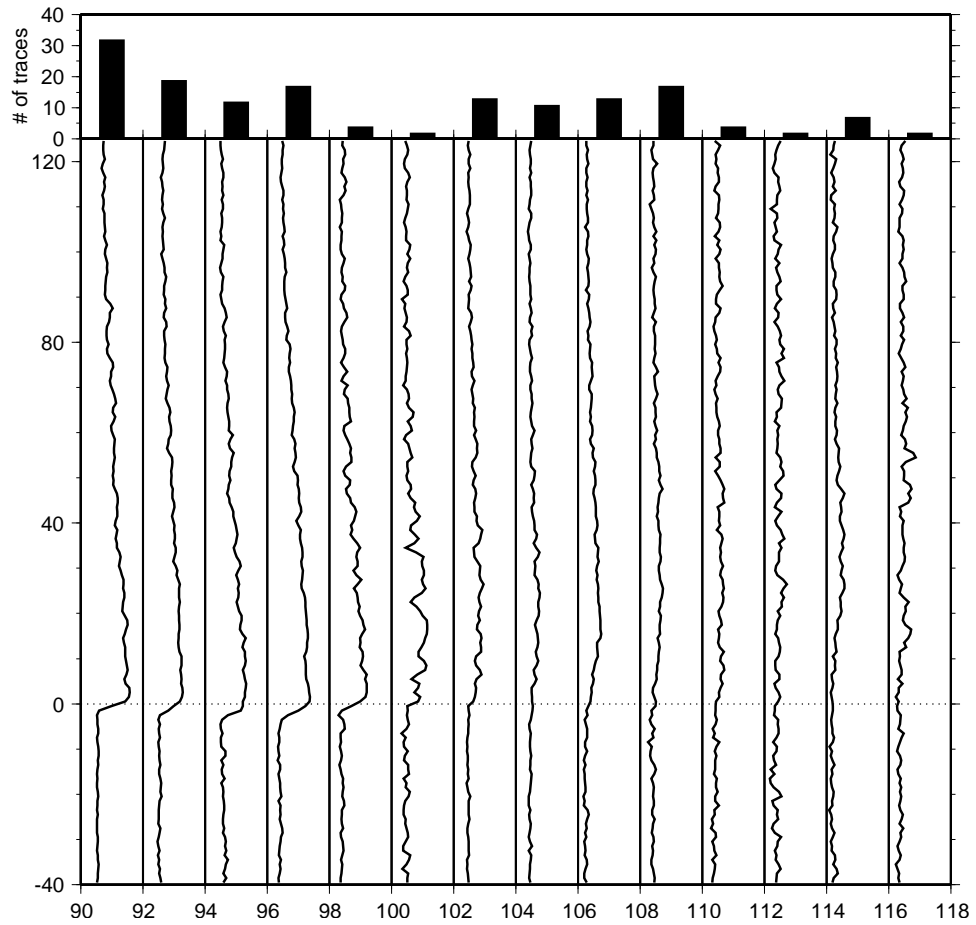


Figure 4.6: Amplitude shapes for the events from Tonga-Fiji.

clearly show how the coda energy decays differently between the biggest and the smallest CDR. Tonga-Fiji paths have the quickest coda energy decay. Its coda energy at 120 sec after the initial pulse is only 0.5 times higher than its pre-event energy level. In addition the coda energy at 120 sec only has about 3% of the maximum energy level. On the other hand, the South America path has the smallest CDR value. Its coda energy at 120 sec after the initial pulse still is 8 times stronger than its pre-event energy level. The coda at 120 sec still has about 9% maximum energy. Its coda energy decays much slower than the decay of the coda from the Tonga-Fiji path.

We plot all the CDRs of P and Pdiff between 70 and 120 deg from three regions in Fig 4.7(d). The red dots are the CDR measurements from Asia, black dots are from South America, and green are from Tonga-Fiji. Before 90 deg, the observed CDRs are around 0.009, however, this value is not constant at the larger distances. For the larger distances, which preferentially sample the lowermost mantle, the observed CDRs gradually decrease with increasing distance. This feature means that from 70 to 90 deg (at least 150 km above the CMB) the decay rate of coda is constant. But for the larger distances, the coda decays slower and slower when the distance becomes larger and larger, or as sampling depth gets deeper and deeper. An interesting question is the cause of the decreased coda decay.

If fine-scale scatterers are uniformly distributed throughout the mantle, we probably would not observe the CDR variation shown in Fig 4.7. The CDR shape as a function of distance suggests that the fine scale scatterers are not uniformly distributed in the mantle. The CDR decreases its value for bottoming depth greater than 150 km above the CMB (Fig 4.7). When the wave travels through and samples more of D'', the scattered energy becomes significantly higher than the scattered energy for paths above D''. It suggests that more fine scale scatterers exist in the lowermost mantle, which can contribute more energy to the coda.

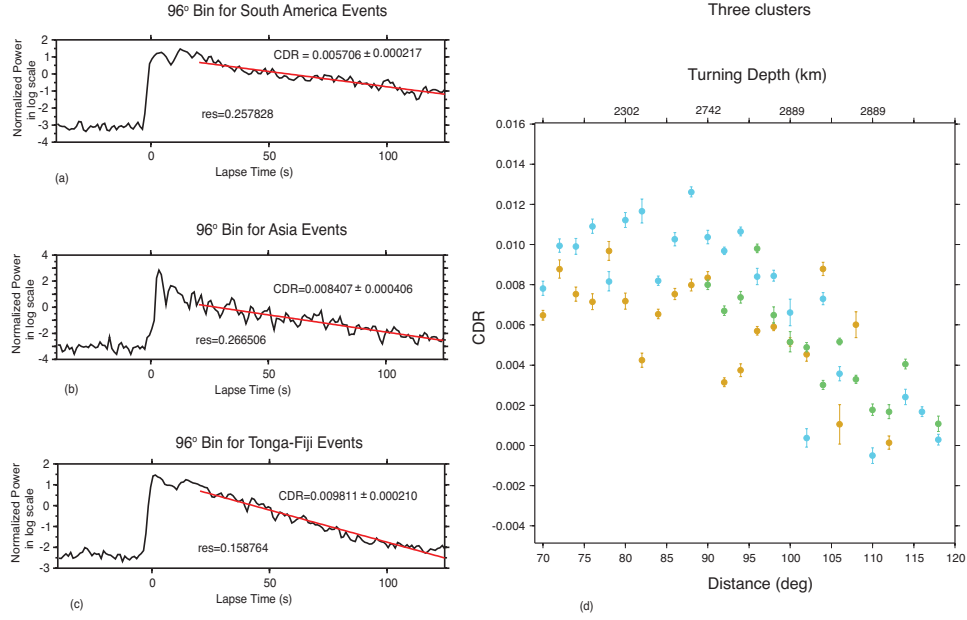


Figure 4.7: Example of the coda decay rate measurement (a,b,c). Coda decay rate from three regions (d). Green: Tonga-Fiji; blue: Asia; brown: South America. The nominal core-mantle depth is 2891 km based on the AK135 Earth model.

Fig 4.8 shows the sampling region in the lowermost mantle for Asia, South America, and Tonga-Fiji data set. By reconstructing plate motions over the past 180 Myr, *Ricard et al.* [1993] modeled the existence of a density heterogeneity in the lowermost mantle beneath central North America and northeast Eurasia, where it also has been shown that subducted slabs reach the CMB in tomography studies [*Li et al.*, 2008a; *Ren et al.*, 2007; *Zhao*, 2004; *Grand*, 2002, 1994]. The subducted slabs inject the source of the heterogeneity, and drive the mantle convection. Then, the convection segregates or disaggregates the slab into fine pieces. *Hirose et al.* [2005] has shown that thermally equilibrated subducted MORB is denser than the average mantle. Since the subducted MORB is denser and segregated, its existence in the lowermost mantle would scatter seismic energy traveling through it, and slow down the decay of the coda.

For the waves traveling through a hotter region, we also observe a reduced CDR.

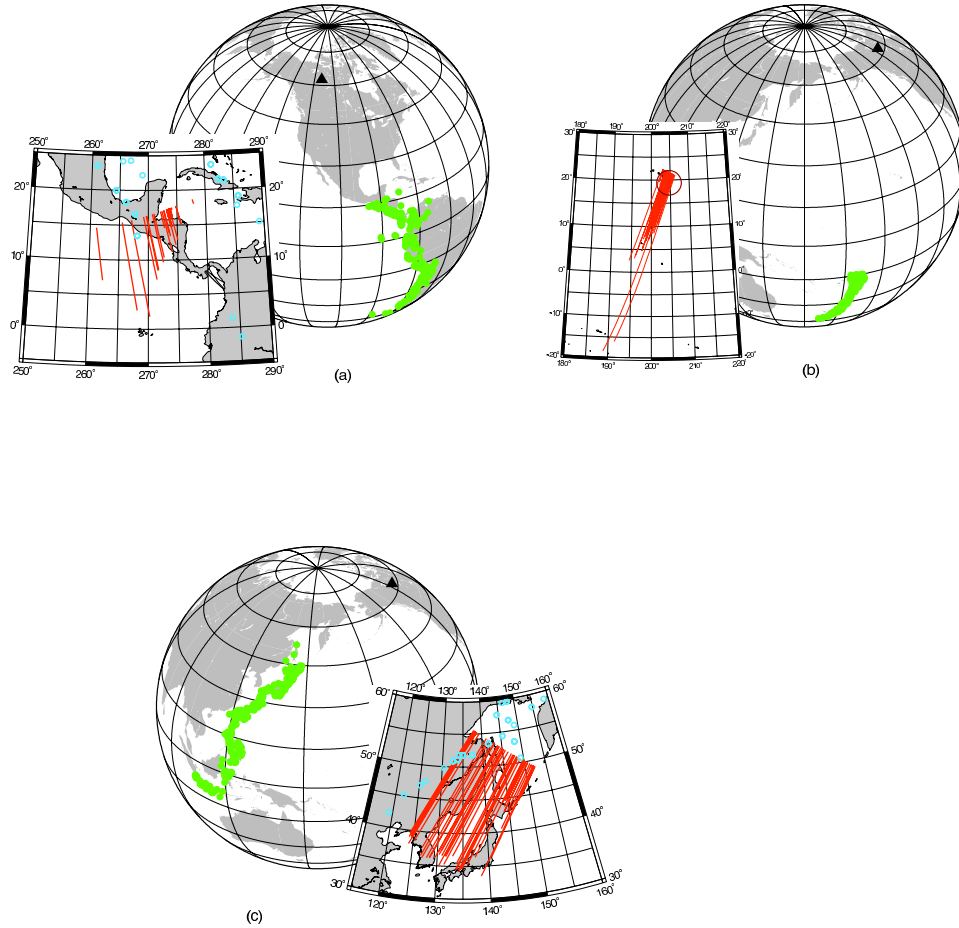


Figure 4.8: Sampling regions (orange line) in the lowermost mantle for the data from (a) South America, (b) Tonga-Fiji, (c) and Asia. The green dots are the event locations. The blue open circles are the paleo-subducted slabs in the lowermost mantle [Ricard *et al.*, 1993; Lithgow-Bertelloni and Richards, 1998]. The red open circle is the location of the Hawaii hotspot.

It also is possibly caused by the existence of the subducted denser and segregated MORB swept by the mantle convection. Geodynamic simulations [Christensen and Hofmann, 1994; McNamara and Zhong, 2004, 2005] have shown that the segregated denser MORB can be driven towards the large low shear velocity provinces (LLSVP) by mantle convection. The Hawaii hotspot is located inside the Pacific LLSVP. Our reduced CDR measurement supports the existence of small scale heterogeneities inside the LLSVP.

Our radial variation observations of CDR suggest more fine scale scatterers exist

in the lowermost mantle which agrees well with the previous studies [*Cleary and Haddon, 1972; Haddon and Cleary, 1974; Bataille and Flatté, 1988; Bataille et al., 1990; Tono and Yomogida, 1996, 1997*].

#### 4.2.2 Lateral variation of CDR

The radial variation of CDRs shows a decaying shape with increasing distance or bottoming depth. This leads to the question of potential lateral variations of CDR in the lowermost mantle. The data from Sumatra-Andaman and Tonga-Fiji mainly sample a wide region of the lowermost mantle beneath North Pacific. The CDRs from this data set might help us understand the lateral variation of the fine-scale scatterers. We stack the beam power in 5 deg bins of backazimuth for the events from Sumatra-Andaman and Tonga-Fiji. As the radial variation shows a linear relationship between CDRs and distance (declining CDR with increasing distance) after 90 deg, we remove this trend from the stacked results using the epicentral distance derived from the mean latitude and longitude of each bin. After the detrending, the negative values represent slower decay or higher coda energy level, and more fine scale scatterers relative to the positive values. Fig 4.9(a) shows the detrended CDRs for Sumatra-Andaman and Tonga-Fiji events. I also show the paleosubducted slabs (brown dots) and the sampling path in the lowermost mantle (thick line) in Fig 4.9(a). For the events sampling the lowermost mantle beneath the Pacific ocean, the detrended CDRs are positive compared to the deconvolved results for the events sampling the lowermost mantle beneath the northeastern Eurasia.

Since it is plausible that the radiation pattern may affect the coda decay rate in some non-correctable manner (with larger radiation patterns causing faster apparent coda decay rates) I compute the averaged radiation pattern for each bin and plot them in the same way as the CDRs to check for any radiation pattern effect (Fig 4.9(b)). The averaged radiation pattern has bigger value for the events

sampling northeastern Eurasia, which has small detrended CDRs, slow decaying. This opposite trend implies that there is no radiation pattern effect in our CDR observations. *Boatwright and Choy* [1986] studied the energy flux of the P wave groups (P + pP + sP) from the shallow earthquakes and pointed out that the energy flux of the P wave group is more affected by the takeoff angle for strike-slip faults compared to dip-slip faults. Fortunately, events used to infer the lateral variation in CDR are dominantly dip-slip at the ongoing subduction zones of Sumatra-Andaman and Tonga-Fiji.

In addition to the lowermost mantle, the lithosphere is another highly heterogeneous place. Therefore, it is possible that the observed lateral variation in CDRs may be influenced by lateral variations in the near-source environment. Since we mainly use shallow events, examining the CDR from the deep events is one thing that must be done to confidently identify the location of the scatterer. The depth phase complicates the CDR of deep events as it is apparent within the CDR measurement window of the direct phase. Because of this we only measure the CDR for events deeper than 500 km and occurring in a continuous region. Fig 4.9(c) shows the CDR measurements for the deep events satisfied by this criteria, processed exactly the same as the shallow events, binned in 5 deg increments of backazimuth, and detrended as the shallow events were. The deep events avoid the lithosphere scattering effect at the source side, but otherwise have the same path in the deep mantle as the shallow events. Although the CDRs from the deep events only cover 25 deg of backazimuthal space, they sample the most important region, in which the detrended CDRs change from positive to negative. The CDRs from the deep events also have negative deconvolved values beneath northeastern Eurasia, and positive values beneath the north Pacific. The same CDR pattern for shallow and deep events, suggests that the scatterers in the lowermost mantle are the main contributor of our observed coda decay anomalies.

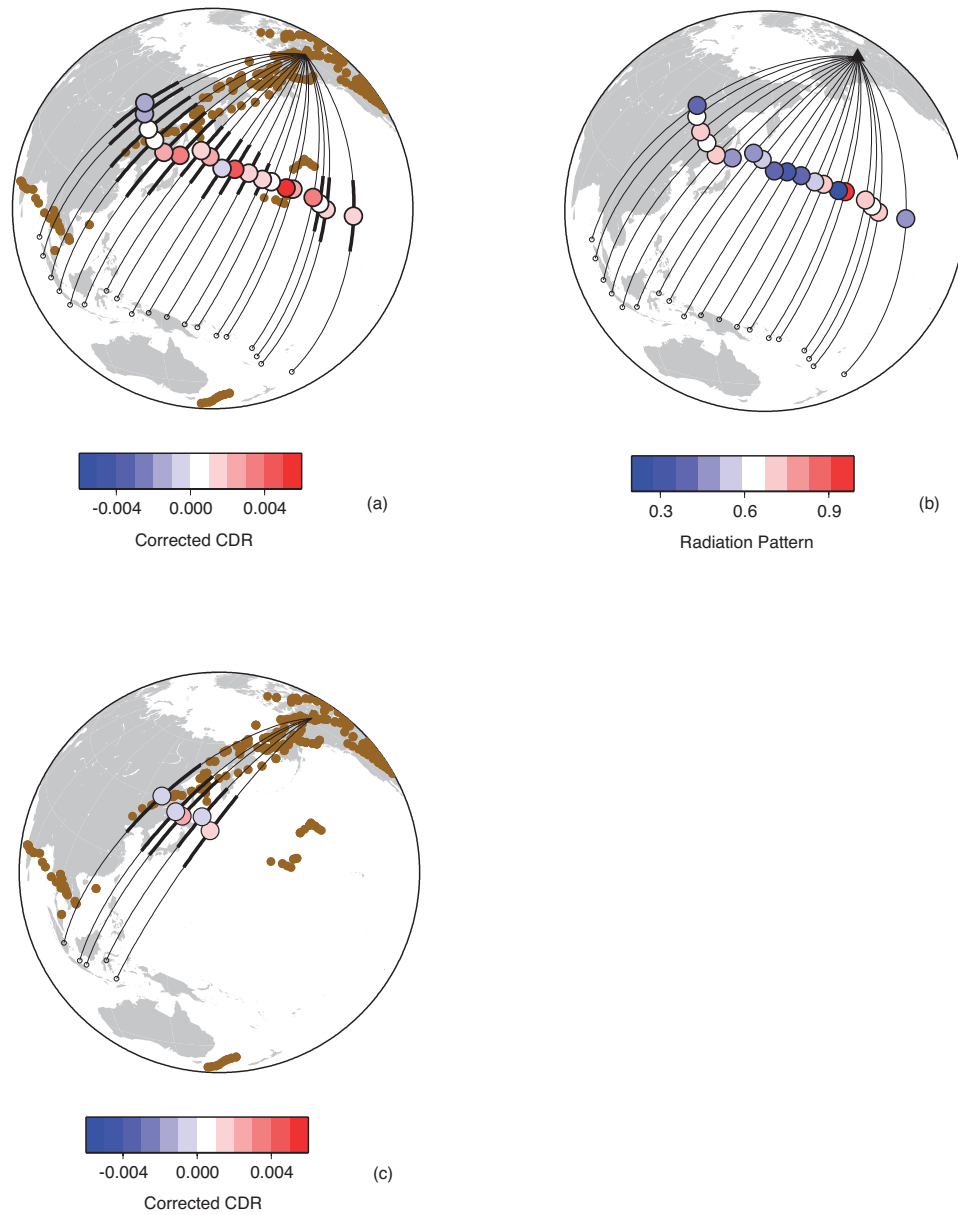


Figure 4.9: (a) Lateral variation of CDR. (b) The binned radiation pattern of all events from Sumatra-Andaman and Tonga-Fiji. (c) The CDR from the deep events occurring in Sumatra-Andaman subduction zone. The thick black line along the ray path represents the sampling region in the lowermost mantle. The brown dots are the paleo-subducted slabs.

### 4.3 Amplitude of the P or Pdiff

Elastic scattering will redistribute the energy to the coda from the direct pulse and so reduce the amplitude of the direct pulse. I plot the binned amplitudes of the direct pulse in Fig 4.10. Similar to the CDR values, the amplitudes also plunge at about 150 km above the CMB. When the P wave diffracts around the CMB, the amplitude of the direct pulse is reasonably smaller than the wave that turns above the CMB. However, our observations show that the amplitude of the direct pulse starts to decrease when the wave reaches the lowermost mantle, before it begins to diffract. This decreasing amplitude of the wave as it begins traveling through the lowermost mantle, further supports increased scattering in the lower mantle.

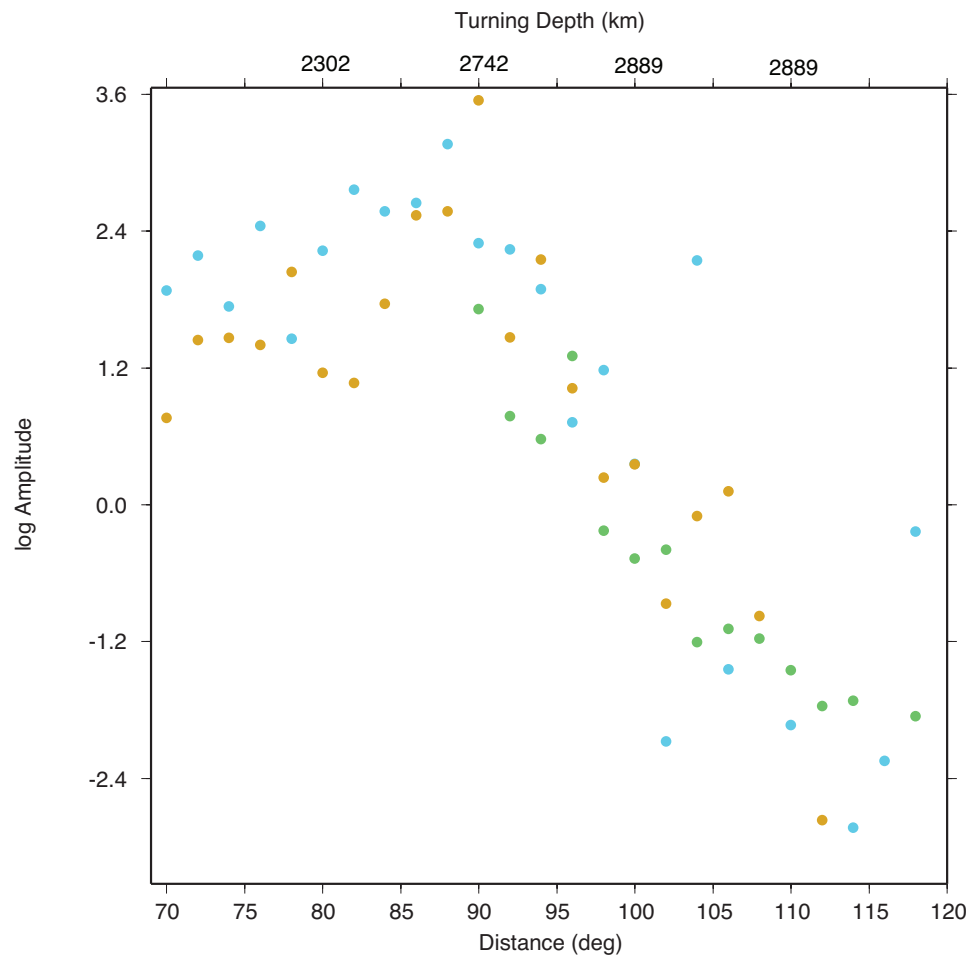


Figure 4.10: The change of the expected amplitude of P/Pdiff as a function of distance.

## Chapter 5: Synthetic Simulation and Modeling of Coda Waves

There are several techniques to generate synthetic seismograms for realistic earth models. Normal mode summation [*Knopoff et al.*, 1973; *Kennett and Kerry*, 1979], generalized ray theory [*Gilbert and Helmberger*, 1972], reflectivity [*Fuchs and Müller*, 1971], finite element [*Smith*, 1974], and finite difference [*Boore*, 1970]. However, these methods are computationally limited or suffer from approximations that limit their usefulness to short periods or radial Earth models. Scattering methods of generating seismograms originated from Kirchhoff theory and are suitable to simulate the heterogeneous Earth when the heterogeneity is described stochastically by a probability density function.

Analysis of coda at regional and local distances [*Aki et al.*, 1958; *Aki and Tsujiura*, 1959] was one of the earliest studies of heterogeneous Earth structure using high frequency seismic waves. At that time, a single scattering approximation was used to simulate the observed regional coda [*Aki and Chouet*, 1975; *Sato*, 1977]. Later, scattering theory was adapted to model teleseismic data and fine-scale heterogeneities in the deep earth, which includes the study of PKP precursors [*Haddon and Cleary*, 1974; *Doornbos*, 1978; *Bataille and Flatté*, 1988; *Hedlin et al.*, 1997; *Vidale and Hedlin*, 1998], Pdiff coda [*Earle and Shearer*, 2001], and PKiKP coda [*Vidale and Earle*, 2000; *Leyton and Koper*, 2007a].

In addition to single scattering methods, multiple scattering methods have also been used to model small-scale heterogeneities in the mantle [*Margerin and Nolet*, 2003b, a; *Shearer and Earle*, 2004]. But a single scattering method, which is computationally much faster, has been found adequate for whole mantle scattering [*Margerin and Nolet*, 2003b, a], and I will use the single scattering method to model the small-scale heterogeneities in the mantle. However, because all of these techniques inherit the disadvantages of ray theoretical approaches, it must be

properly modified to account for changes in amplitude associated with diffraction along the core-mantle boundary.

## 5.1 Basics of Single Scattering Approach

*Scott and Helmberger* [1982] were one of the first to apply the secondary source idea (the Kirchhoff theory) from optics to seismology. Kirchhoff theory provides a useful method to solve the situation when the wave interacts with a rough interface. An equivalent method related to Kirchhoff theory, known as the Born approximation, is used widely in the case of the weakly heterogeneous material [*Wu and Aki*, 1985a, b; *Hedlin et al.*, 1997; *Earle and Shearer*, 2001; *Leyton and Koper*, 2007b].

In the Born approximation, the heterogeneities (which act as secondary sources) have perturbations,  $\delta\rho$ ,  $\delta\lambda$ , and  $\delta\mu$  in density, P, and S velocity respectively, relative to the background velocity model,  $\rho_0$ ,  $\lambda_0$ , and  $\mu_0$ . Owing to the existence of the perturbation, the total displacement includes two parts, the primary waves and the scattered waves. Following *Aki and Richards* [1980], the single scattering Born approximation for the perturbed medium can be expressed as

$$\begin{aligned}\rho &= \rho_0 + \delta\rho \\ \lambda &= \lambda_0 + \delta\lambda \\ \mu &= \mu_0 + \delta\mu\end{aligned}\tag{5.1}$$

which are used in the equation of motion

$$\rho\ddot{u}_i = (\lambda\nabla \cdot \mathbf{u})_{,i} + [\mu(u_{i,j} + u_{j,i})]_{,j}\tag{5.2}$$

By substituting Eq(5.1) to Eq(5.2) and solving the equation, we can get the average power of the scattering waves

$$\langle |\Phi(\theta)|^2 \rangle = \frac{2k^4 a^3 \langle \mu^2 \rangle V A^2}{\pi r^2} * \frac{\frac{1}{4} [\cos(\theta) + \frac{1}{3} + \frac{2}{3} \cos^2(\theta)]^2}{[1 + 4k^2 a^2 \sin^2(\theta/2)]^2} \quad (5.3)$$

where  $\theta$  is the scattering angle,  $k$  is the wavenumber,  $a$  is the correlation distance,  $\langle \mu \rangle$  is the r.m.s. velocity perturbation,  $V$  is the volume of the scatterer,  $A$  is the incident wave amplitude, and  $r$  is the distance from the scatterer to receiver (e.g., Hedlin and Shearer, 2000). Note that this assumes that the heterogeneities are distributed stochastically according to an exponential auto-correlation function.

To implement this approach I divide the Earth’s mantle into a 3D grid of voxels that have approximately equal volume. For a given source receiver distance, a loop is performed over all voxels in which each is “connected” to the fixed source and receiver location by using ray theory in a background reference Earth model. Ray paths, ray parameters, and times are derived using the tau-p formalism, and the amplitudes account for the effect of geometrical spreading, intrinsic attenuation, and the change in amplitude upon scattering given above. Furthermore, reflection coefficients for waves interacting with the CMB and ICB are included. The sum of the effect of all the voxels yields coda energy as a function of time for a given source-receiver distance.

In practice, tables are used to store precomputed values of travel time, ray parameter, and relevant derivatives for a series of depths and distances. The program then needs only to “look up” the appropriate values for given voxel, source, and receiver locations and properly connect the two pieces. I tested integration steps of 1 km, 0.5 km, and 0.25 km in generating the ray theory tables and found that 0.5 km does provides highly accurate values.

Fig 5.1 shows an example of using this technique to generate a synthetic P-wave coda at 76 degree. I use the AK135 Earth model [Kennett *et al.*, 1995] as the

background reference model for raytracing, and use a slightly modified version of the whole mantle scattering model described by *Shearer and Earle* [2004]. In this whole mantle scattering model, D'' has scatterers with 1% velocity perturbation, 0.8% density perturbation, and the characteristic size of 2.0 km. The lower mantle above the D'' has the very weak scatterers with 0.05% velocity and 0.04% density perturbations. The characteristic size is also bigger than that in D''. I use 10.0 km for the size of the scatterers existing from 780 to 1780 km, and 5.0 km for those in the range of 1880 to 2480 km. As the upper mantle is another heterogeneous portion of the earth, we give a 2.0 km scatterer size between depths of 280 and 680 km with 2% velocity perturbation and 1.6% density perturbation. In my model the scatterers in the depth range, 80 to 180 km, have the strongest velocity and density perturbation, 3% and 2.4% respectively. The size of these strongest scatterers also is 2.0 km. Since my CDR observations are normalized by PP, I also normalize the synthetic coda by ray theoretical amplitude of PP.

## 5.2 Incorporating Diffraction Into the Synthetic Codas

I have described how single scattering works according to ray theory, however, it must be modified to account for the decrease in energy as a wave diffracts around the CMB, which is an indispensable part of my synthetic simulation. The diffracted energy is accounted for by applying a half-distance factor which controls how far the energy can diffract around the core-mantle boundary before it decays to half of its value after it began diffracting. For instance, if we assume a half-distance of 4.0 degrees then the ray theoretical amplitude will be reduced by 50% for every 4.0 degrees of distance a ray segment spends diffracting around the CMB.

To estimate a realistic value for the half-distance, I use the frequency-wavenumber method [*Herrmann, 2007*] to generate synthetic seismograms for 90 to 130 deg, Fig 5.2, using the AK135 earth model and a source depth of 0

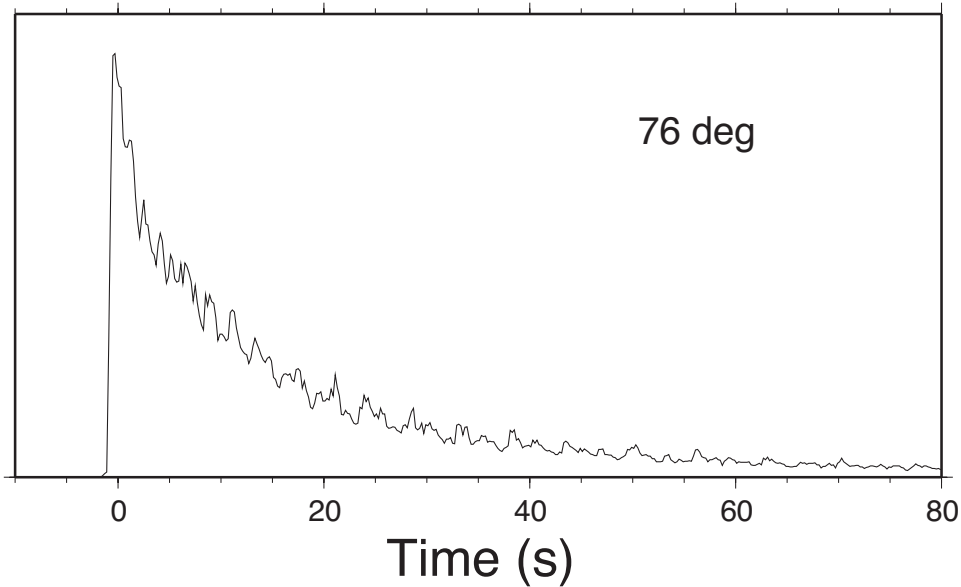


Figure 5.1: Example of the synthetic envelope of the vertical component of P and its coda at 76 deg using the single scattering method described in the text. The time is relative to the theoretical P arrival time.

km. Then, I measure the peak-to-peak amplitude of the P/Pdiff at 1 Hz. After this, I find the linear relationship between the log normalized amplitude and the distance using an L2 norm to fit the measurements. The slope derived from the linear fit and the assumption, the amplitude decays to its half after traveling one half distance, are applied to the equation,  $\log(0.5) = slope * half\ distance$ , to get the half distance. I find a value of about 4.0 deg for the half distance at 1 Hz.

Because the frequency-wavenumber method assumes a smooth boundary for the CMB, the 4.0 deg half distance at 1 Hz should be considered an upper limit. Rough topography on the CMB will also scatter energy away from the direct arrival and cause the effective half distance to be smaller. Therefore, I allow for some flexibility in the value of half-distance used in the forward modeling. Fig 5.3 provides an example of the effect of the half distance on synthetic envelopes. I compare the synthetics at 100 deg and 110 deg using 10 deg, 4 deg, and 2 deg half distances,

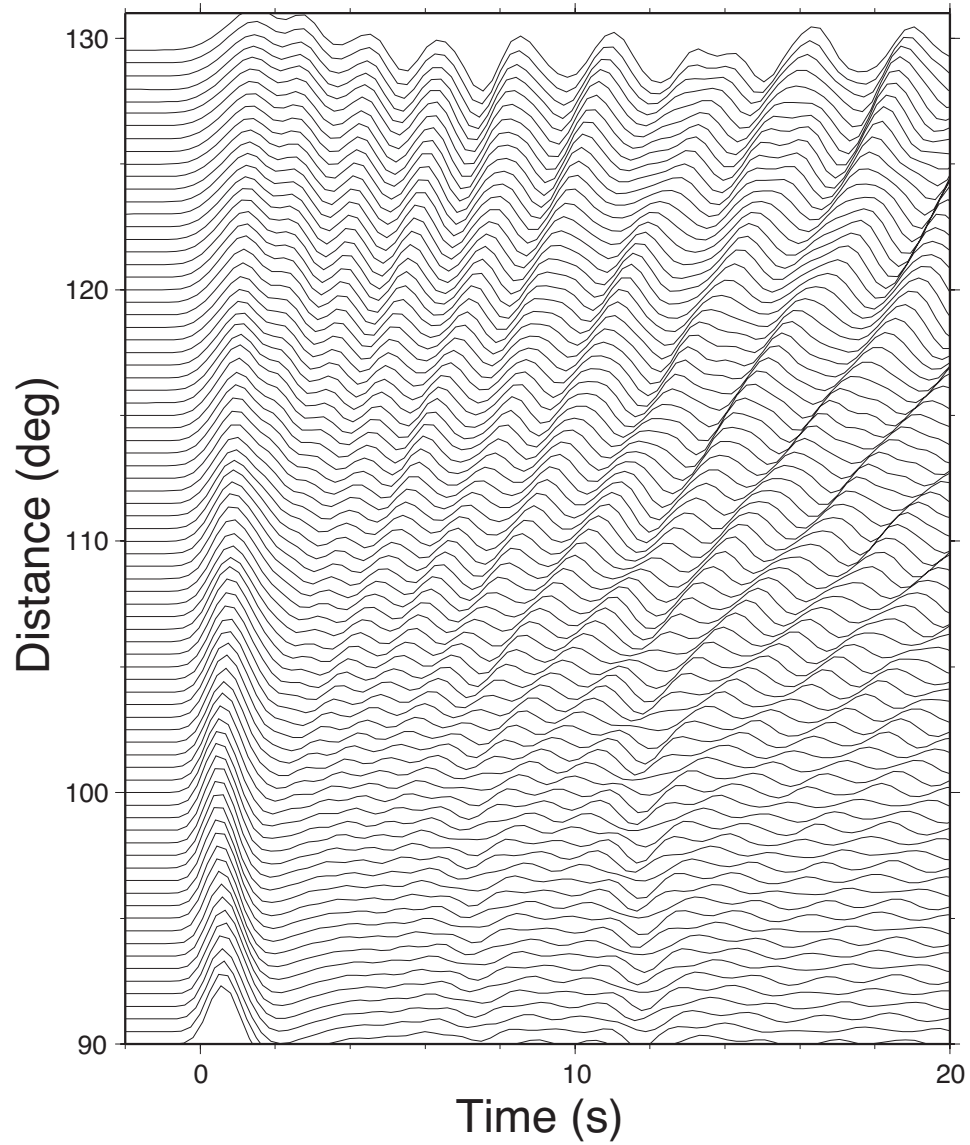


Figure 5.2: Synthetic seismograms for the P/Pdiff phase from the frequency-wavenumber method [Herrmann, 2007] using the AK135 earth model.

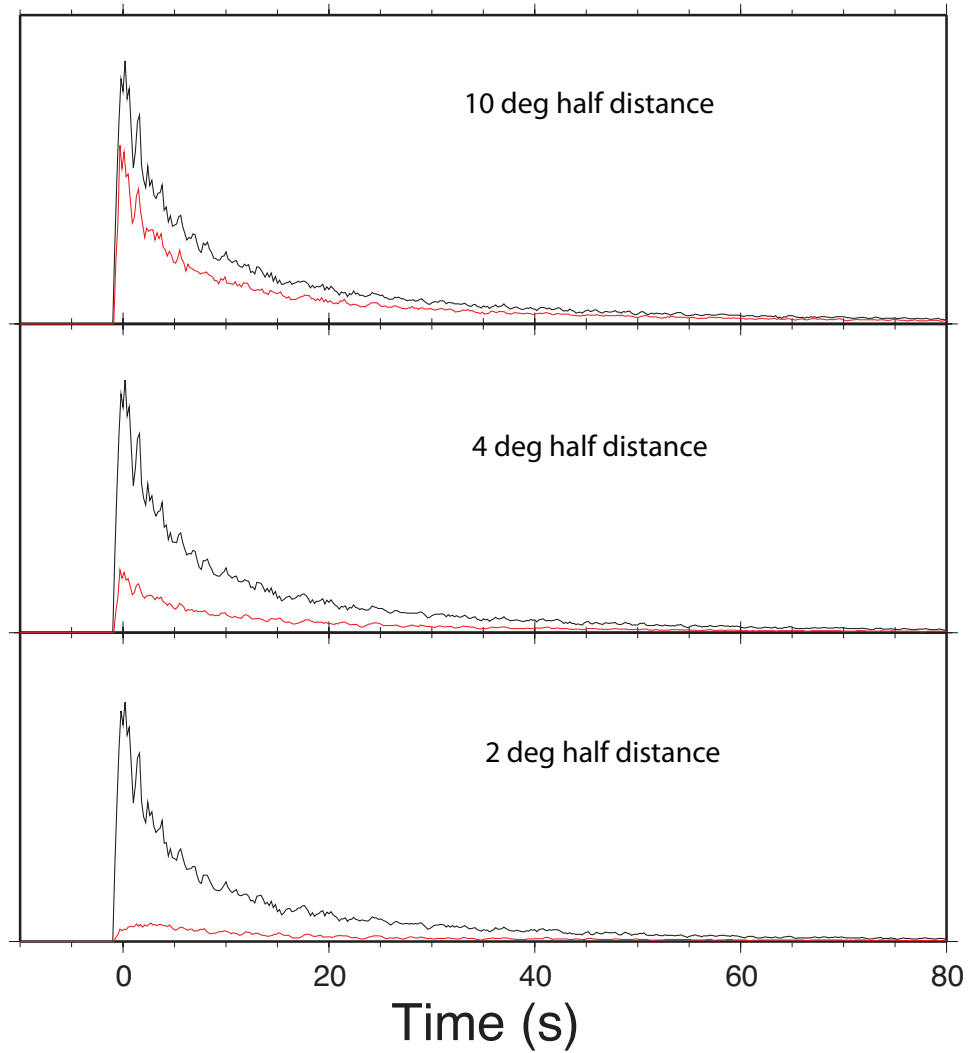


Figure 5.3: Example of the effect of the half distance. The black curves are the synthetics at 100 deg. Red curves are the synthetics at 110 deg.

which correspond to half,  $3/16$ , and  $1/32$  of the initial energy after traveling 10 deg along the CMB. The comparison shows that the larger half-distance does maintain more energy after traveling the same distance along the CMB. Through this comparison, the effect from the half distance is shown very clearly.

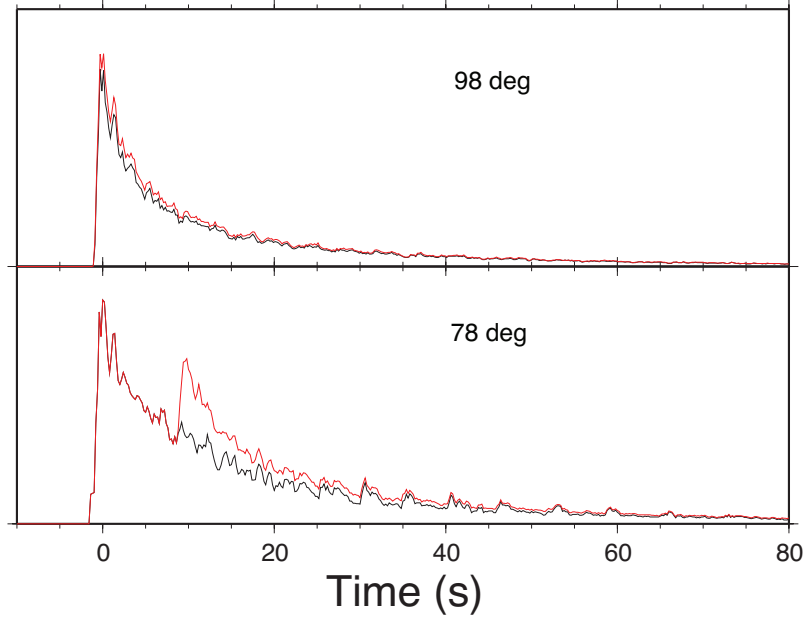


Figure 5.4: Example of synthetics at 78 deg, bottom panel, and 98 deg, top panel. Black: the synthetics without PcP phase. Red: the synthetics with PcP phase.

### 5.3 Effect of PcP

Another factor to consider in generating synthetic P codas is the energy created by reflections from CMB, denoted as PcP. At distances greater than 70 degrees, PcP arrives within 20 s of direct P. Therefore, I do a test to explore how significant the addition of scattered PcP branches is to synthetic P coda.

Fig 5.4 shows the effect of PcP coda on the synthetic P coda for a shorter distance, 78 deg, and a larger distance, 98 deg. At the larger distance, the effect from the PcP coda is very weak. Even though the PcP phase is clear for the shorter distance, the associated PcP coda does not have a big contribution in my CDR fitting window starting 20 sec after P arrival time. This test concludes that PcP coda does not have a significant effect on coda decay rate measurements of P/Pdiff.

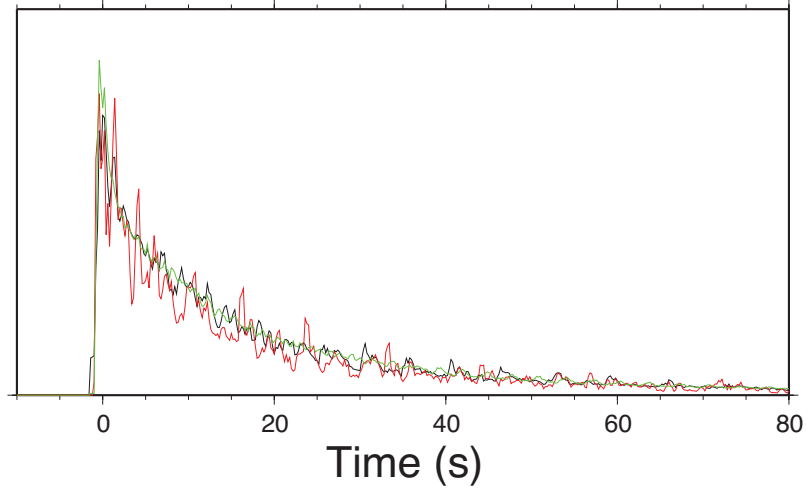


Figure 5.5: Example of synthetics at 78 deg using different voxel size. Black:  $100^3 km^3$ . Green:  $50^3 km^3$ . Red:  $200^3 km^3$ .

#### 5.4 Effect of Voxel Size of Synthetic Codas

The starting point of using the single scattering method is dividing Earth's mantle into series of approximately equal-volume voxels (integration elements). The size of the voxel might affect the coda simulation, just as the integration step can affect the computed travel time for a seismic ray. Here, I explore the effect of voxel size on synthetic codas.

I try three sizes: the big voxel,  $200^3 km^3$ , the medium voxel,  $100^3 km^3$ , and the small voxel,  $50^3 km^3$ . The small voxel yields a smooth coda compared to that from the bigger voxel, Fig 5.5. However, the trend of the coda from different voxel size is the same. The test also shows that it is not necessary to use the smallest voxel as the synthetic from the medium voxel does not have a big difference compared to that from the smaller voxel. Considering the savings in computation time (which scales as the cube of the voxel dimension),  $100^3 km^3$  is the proper size to use.

## 5.5 Effect of Source Time Function

The source time function of a seismic event might also affect the synthetic simulation. Until now, the synthetics are essentially Green's function for the scattering response of the Earth. I first compare the effect of the length of the source time. I try a 5 sec and a 10 sec triangle source time function. This comparison shows no difference after convolving with a synthetic coda. Next I compare a 5 sec long triangle and a 8 sec long trapezoid source time functions to study the effect of different shapes of the source time function. In Fig 5.6, convolving the source time function does smooth the synthetic envelope, but it also causes a delay of the peak energy. The trapezoidal source time function gives a bigger peak shift. Because my CDR fitting window starts 20 sec after the initial arrival time, the peak energy delay will contribute part of the energy to the fitting window and affect the coda decay rate measurement. However, if I consider the shift of the peak energy during the fitting, which means delaying the beginning time of the CDR fitting window with the same amount of value as the peak energy delay, I find no difference on the CDR fitting. This non-difference reveals that the source time function would not affect my CDR measurement because even convolving the source time function smooths and delays the synthetic, the shape of the synthetic coda keeps the same.

## 5.6 Effect of Q in the Lower Mantle

A final parameter to consider when generating synthetic Pdiff codas is the Q structure of the mantle, and in particular the Q structure of D". Seismically it is difficult to measure Q in the mantle, so there is some flexibility allowed relative to reference models. Here I compare synthetic envelopes at 110 deg using the AK135 Earth model and the chQ9 model with  $Q_p = 233$  and  $Q_s = 150$  in D", Table 5.1. The AK135 model has high quality factor in the crust and the mid-mantle and the

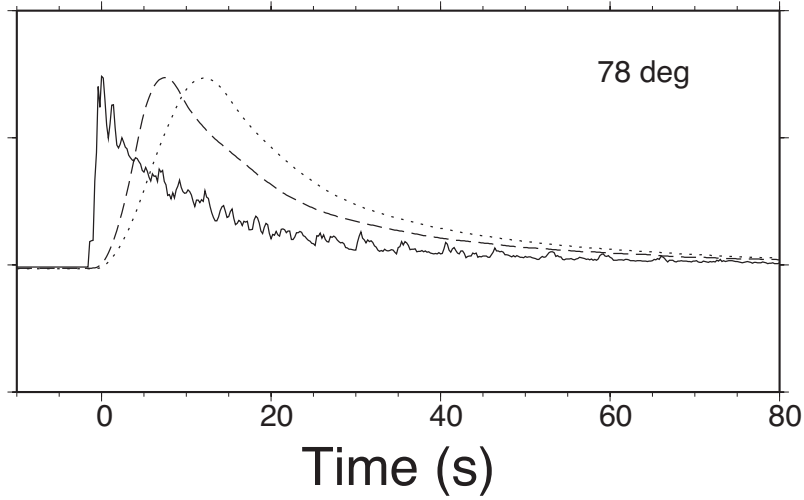


Figure 5.6: Example of synthetics at 78 deg. Solid line, synthetic without source time function. Dashed line, synthetic convolved with a 5 sec long triangle source time function. Dotted line, synthetic convolved with an 8 sec long trapezoidal source time function.

Table 5.1:  $Q$  models in  $D''$  used to explore the effect of the attenuation.

|               | 2740 km | 2789 km | 2839 km | 2891 km |
|---------------|---------|---------|---------|---------|
| $Q_p^{ak135}$ | 444     | 444     | 444     | 444     |
| $Q_s^{ak135}$ | 274     | 274     | 274     | 274     |
| $Q_p^{chQ9}$  | 233     | 233     | 233     | 233     |
| $Q_s^{chQ9}$  | 150     | 150     | 150     | 150     |

smallest quality factor in the asthenosphere. The quality factor in the upper mantle is obviously lower than the value in the crust and the mid-mantle. When the depth reaches the CMB, AK135 gives a relatively high attenuation for  $D''$ . These two models have a difference on the quality factor only in the lowermost mantle.

However, this small difference results in a big difference on the synthetic envelope. Decreasing the quality factor by half causes about a three times smaller amplitude, Fig 5.7.

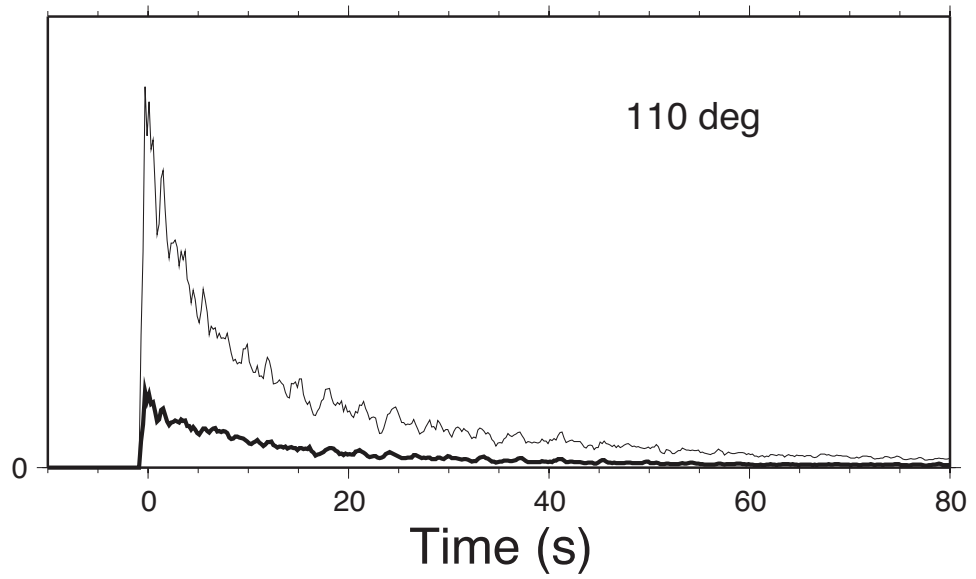


Figure 5.7: Synthetics at 110 deg from different attenuation model of D". Solid line: ak135. Thick line: ak135.chQ9.

## Chapter 6: Forward Modeling of Observed P/Pdiff Coda Waves

I now use the method described in Chapter 5 to model the observations described in Chapter 4. There are too many free parameters to perform a formal inversion for Earth structure. Instead, I focus on a forward modeling approach to find models that are consistent with the observations, though not necessarily unique. In order to compare to the observations, I use the same curve-fitting approach on synthetics as on data. After processing the synthetics, I focus on matching the CDR as a function of distance. I do not try to match the coda intercept, because it is affected by too many parameters unrelated to scattering in the Earth. Because the goal of my work is detecting heterogeneities in the mantle, coda generated by the scatterers in the mantle is a more appropriate tool to use than studying the main phase. By matching the distance variation of the CDR, I am able to constrain the radial distribution of fine-scale scatterers.

In Chapter 5, I described the synthetic method I use and some important parameters that need to be considered. In the forward modeling, I constrain the half distance, attenuation in the lowermost mantle, the distribution of the scatterers, and the strength of the scatterers by comparing them to the CDR observations. By constraining the half distance, I infer the degree of roughness of the core mantle boundary. By constraining attenuation in the lowermost mantle, I infer material properties near the CMB. By constraining the distribution of the scatterers and the strength of the scatterers, I can contribute to the existing debate on mantle convection and have a better understanding of mantle dynamics.

### 6.1 The Effect of CMB Topography

In Chapter 5, I examined the effect of the half distance on synthetic codas. Physically, the half-distance corresponds to all phenomenon affecting the amplitude

of Pdiff that are not accounted for by ray theory propagation in a radial model. The primary factor is amplitude reduction because of diffraction around the core, however, a second factor likely to play a role is amplitude reduction via scattering by CMB topography. This is the why the half-distance estimated from f-k synthetics in a radial Earth model should be considered an upper bound. In the real Earth we can expect energy to decay more quickly and thus have smaller half-distances. Here, I further examine this effect in comparison to the observed CDRs.

I use the AK135 Earth model and the whole mantle scattering model, Table 6.1, to model the half-distance. The test shows that the CMB cannot be smooth since a big half distance does not yield a reasonable CDR at the larger distances, e.g. the dash line in Fig 6.1. Additional evidence of a non-smooth CMB is the CDR simulation using the half distance measured from frequency-wavenumber synthetic seismograms, 4.0 deg. Because the frequency-wavenumber method assumes a smooth boundary, this value should be an upper limit for the real-Earth value. I find that the CDR using a 4.0 deg half-distance has a good match at the shorter distances, 70 to 95 deg, but yields too fast of a coda decay at the larger distances, 95 to 120 deg. The match for the shorter distances but not for the larger distances is a reasonable result because the half distance does not make a significant contribution at the shorter distances in which the direct arrivals turn in the mantle above the CMB. I find that a smaller CDR of 2.0 deg does a better job of fitting the data Fig 6.1.

In addition to the 2.0 deg half-distance fitting the CDR observations better than 4.0 and 10.0 deg, the shape of the synthetic envelope using 2.0 deg half-distance is closer to the real observations than the others. I plot the synthetic envelopes at 110 deg using 10, 4, and 2 deg half-distances in the top panel of Fig 6.1. Because of the existence of the low velocity outer core, the compressional energy can only travel along the core-mantle boundary through diffraction after 98 deg and up to 130 deg.

Owing to the diffraction, the Pdiff energy is weaker than the P energy. And the Pdiff energy becomes weaker as the distance becomes larger. When I plot the P/Pdiff envelopes from 90 to 120 deg, this change is very clear, Fig 4.6. At the shorter distance the P energy is very clear and strong. At the larger distance, the Pdiff energy does not have a very clear impulsive arrival as the P energy and is weak. The Pdiff energy gradually increases and slowly decreases back to the background noise energy level. The synthetic envelopes using 10 and 4 deg half distance at 110 deg both have an impulsive shape for Pdiff energy, and only the synthetic using 2 deg half-distance shows a gradual arrival of the Pdiff energy, as commonly observed in the data.

Now, the effect of the CMB topography is clear. The CDRs from the synthetics with CMB topography can have a better match at the larger distances compared to the CDRs from the one with a smooth boundary. Is this factor the only one that controls the scattering energy in  $D''$ ? To answer this question, I try some even smaller half-distances to examine the effect of CMB topography on my CDR observations. From 2.0 deg to 0.1 deg, the CDRs at the larger distances do have some changes, Fig 6.2. However, no matter how I change the half distance, this factor only can affect the CDR measurements at distances greater than about 98 deg. Prior to this, the synthetic CDRs flat, but in the data the CDR decline starts about 90 deg. This mismatch means that something else in the model must be changed to properly fit the data. A lower half distance can help the CDR fitting, but cannot provide an acceptable CDR fit on its own.

## 6.2 Constraining Q in the Lowermost Mantle

Quality factor (Q) can reveal information on the material properties of the Earth. However, due to poor sampling there still is a big uncertainty on quality factor in the mantle, especially for the lowermost mantle. The synthetic test on the

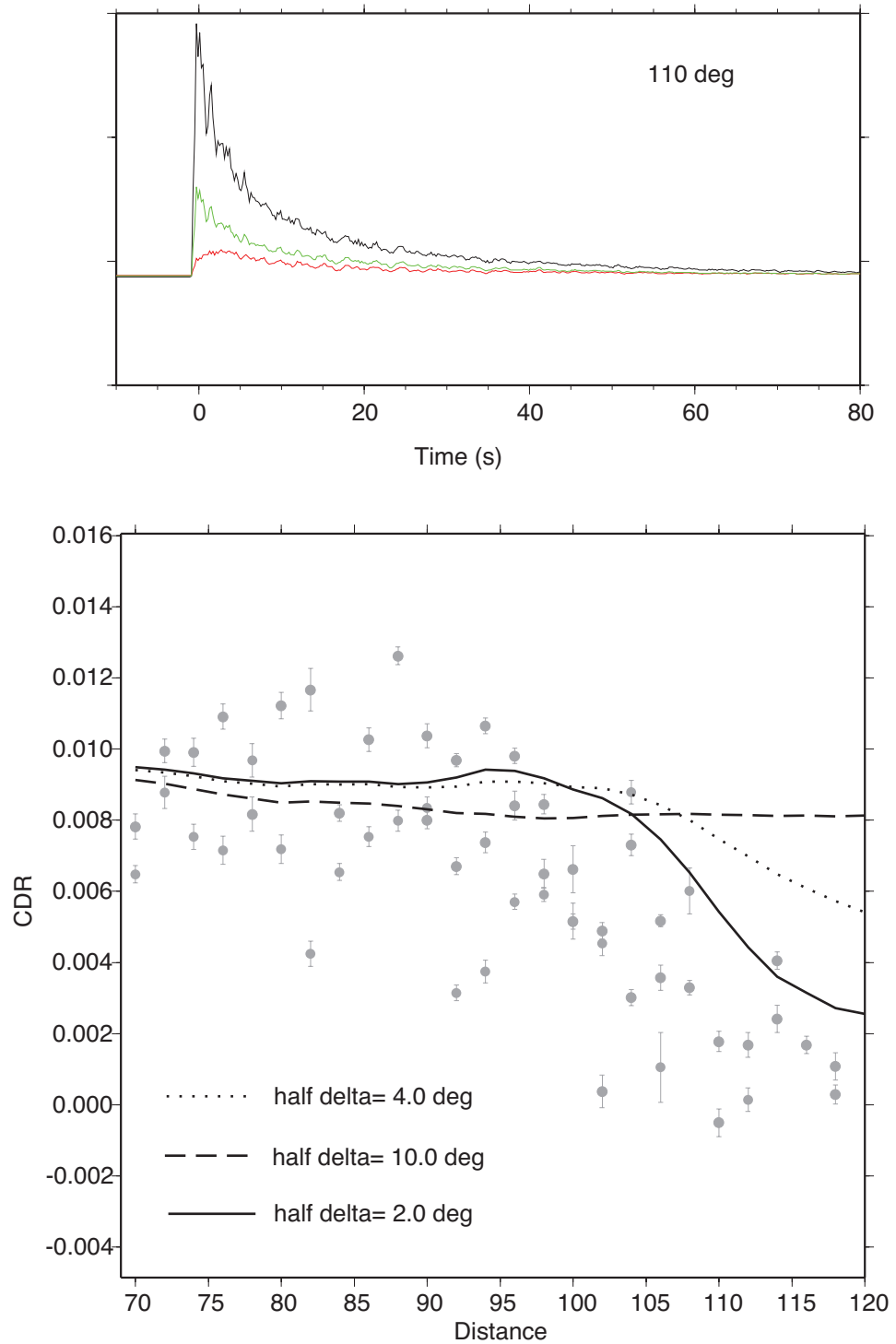


Figure 6.1: Bottom: The effect of the half distance using the whole mantle scattering model and the AK135 Earth model. Top: Example of the synthetics at 110 deg using different half distance. Black: 10 deg half distance. Green: 4.0 deg half distance. Red: 2.0 deg half distance.

Table 6.1: Three scatterering models.

| depth  | scatterer size | Whole mantle |              | Only D'' |              | Only upper mantle |              |
|--------|----------------|--------------|--------------|----------|--------------|-------------------|--------------|
|        |                | $dv/v$       | $d\rho/\rho$ | $dv/v$   | $d\rho/\rho$ | $dv/v$            | $d\rho/\rho$ |
| 2880.0 | 2.0            | 0.01         | 0.008        | 0.01     | 0.008        | -                 | -            |
| 2780.0 | 2.0            | 0.01         | 0.008        | 0.01     | 0.008        | -                 | -            |
| 2680.0 | 2.0            | 0.01         | 0.008        | 0.01     | 0.008        | -                 | -            |
| 2580.0 | 2.0            | 0.01         | 0.008        | 0.01     | 0.008        | -                 | -            |
| 2480.0 | 5.0            | 0.0005       | 0.0004       | -        | -            | -                 | -            |
| 2380.0 | 5.0            | 0.0005       | 0.0004       | -        | -            | -                 | -            |
| 2280.0 | 5.0            | 0.0005       | 0.0004       | -        | -            | -                 | -            |
| 2180.0 | 5.0            | 0.0005       | 0.0004       | -        | -            | -                 | -            |
| 2080.0 | 5.0            | 0.0005       | 0.0004       | -        | -            | -                 | -            |
| 1980.0 | 5.0            | 0.0005       | 0.0004       | -        | -            | -                 | -            |
| 1880.0 | 5.0            | 0.0005       | 0.0004       | -        | -            | -                 | -            |
| 1780.0 | 10.0           | 0.0005       | 0.0004       | -        | -            | -                 | -            |
| 1680.0 | 10.0           | 0.0005       | 0.0004       | -        | -            | -                 | -            |
| 1580.0 | 10.0           | 0.0005       | 0.0004       | -        | -            | -                 | -            |
| 1480.0 | 10.0           | 0.0005       | 0.0004       | -        | -            | -                 | -            |
| 1380.0 | 10.0           | 0.0005       | 0.0004       | -        | -            | -                 | -            |
| 1280.0 | 10.0           | 0.0005       | 0.0004       | -        | -            | -                 | -            |
| 1180.0 | 10.0           | 0.0005       | 0.0004       | -        | -            | -                 | -            |
| 1080.0 | 10.0           | 0.0005       | 0.0004       | -        | -            | -                 | -            |
| 980.0  | 10.0           | 0.0005       | 0.0004       | -        | -            | -                 | -            |
| 880.0  | 10.0           | 0.0005       | 0.0004       | -        | -            | -                 | -            |
| 780.0  | 10.0           | 0.0005       | 0.0004       | -        | -            | -                 | -            |
| 680.0  | 2.0            | 0.02         | 0.016        | -        | -            | 0.02              | 0.016        |
| 580.0  | 2.0            | 0.02         | 0.016        | -        | -            | 0.02              | 0.016        |
| 480.0  | 2.0            | 0.02         | 0.016        | -        | -            | 0.02              | 0.016        |
| 380.0  | 2.0            | 0.02         | 0.016        | -        | -            | 0.02              | 0.016        |
| 280.0  | 2.0            | 0.02         | 0.016        | -        | -            | 0.02              | 0.016        |
| 180.0  | 2.0            | 0.03         | 0.024        | -        | -            | 0.02              | 0.016        |
| 80.0   | 2.0            | 0.03         | 0.024        | -        | -            | 0.02              | 0.016        |

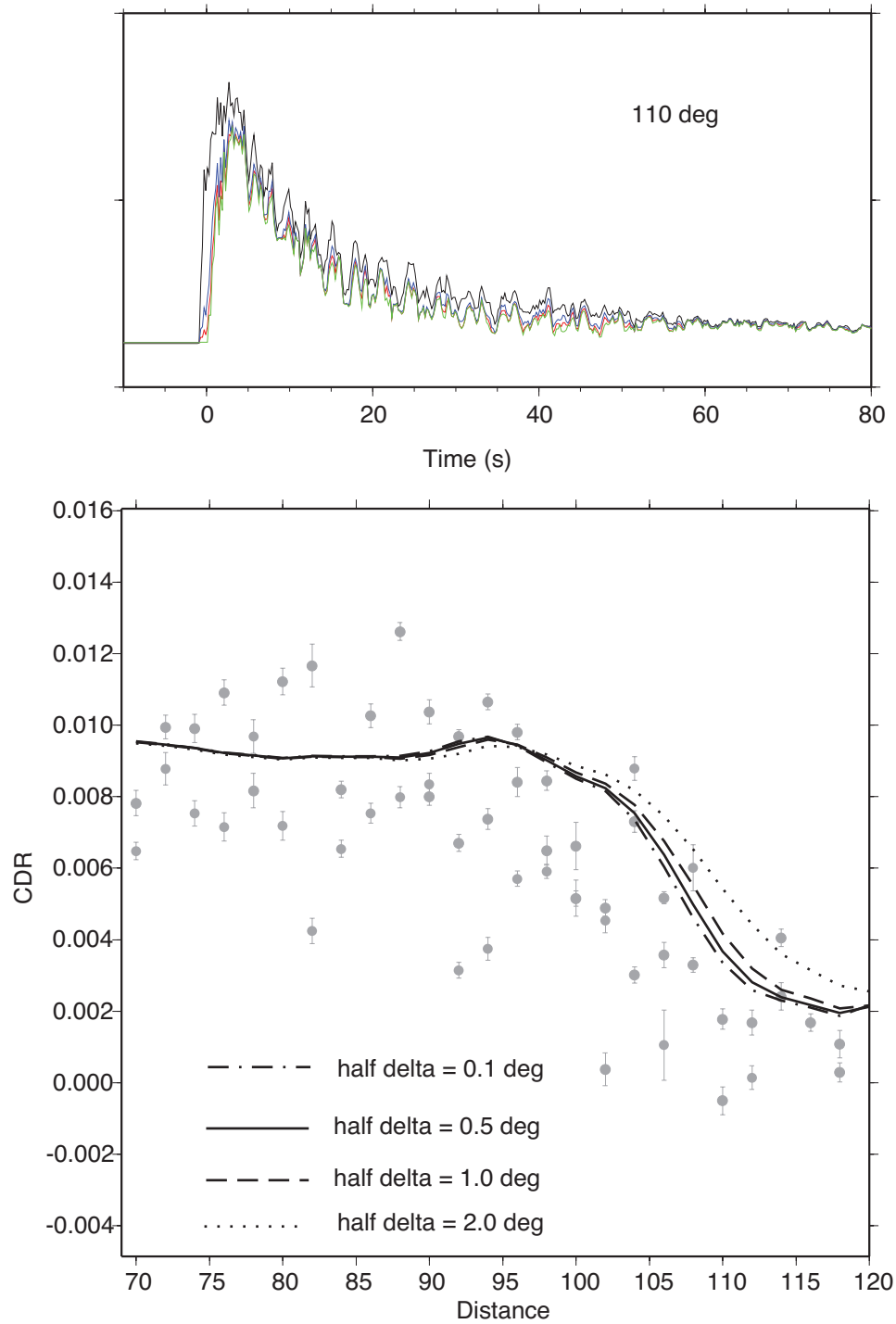


Figure 6.2: Bottom: CDR using different half distance: 2.0 deg half distance, dotted line; 1.0 deg half distance, dash line; 0.5 deg half distance, solid line; 0.1 deg half distance, dash-dot line. Top: Example of the synthetics at 110 deg using different half distance. Black: 2.0 deg half distance. Blue: 1.0 deg half distance. Red: 0.5 deg half distance. Green: 0.1 deg half distance.

quality factor in the lowermost mantle in Chapter 5 has clearly shown its effect on Pdiff envelopes. I will constrain Q in the lowermost mantle through matching the CDR observations.

I use a 4.0 deg half distance and the whole mantle scattering model to test the effect of different Q models in the lowermost mantle, Table 6.2. The test shows that attenuation in D'' plays an important role in the P/Pdiff coda decay rate simulation. Without changing the half distance, the CDR at the larger distances is dropped by lowering Q in the lowermost mantle, Fig 6.3. The AK135 Earth model gives a pretty fast Pdiff coda decay (i.e., a bigger CDR value). When I double the attenuation (lower half Q) in D'', ak135.chQ9 provides a CDR measurement with a significant change at the larger distance. A lower Q value in D'' really can affect the CDR measurement. And this effect is not only on the CDR at the largest distance, it also affects the CDR around 90 deg. This distance is an important area because it is a hinge connecting the flat CDRs at the shorter distances with the gradually declining CDRs at the larger distances. Although changing the half-distance can affect the CDR measurement at the larger distances, half-distance cannot provide a hinge at 90 deg, as seen in the observations. The model with lower Q value in D'' has the hinge at the same distance as the observations. Nevertheless, the attenuation in the lowermost mantle cannot be too high because the model ak135.chQ10 with the lowest Q value in all Q models, Table 6.2, results in a unfitable coda decay rate measurement at shorter and larger distances, a too small coda decay rate at larger distances, and relatively higher CDR at the shorter distance. And this test also shows that the Q value above D'' from the AK135 is proper to represent the attenuation in the mid-mantle because the CDR simulations using the chQ9 and chQ11 model can match the observations at the shorter distances.

Although lower Q in D'' can drop the CDR at the larger distances and generate the hinge connecting the flat and declining parts of the CDRs at the correct

Table 6.2: Five Q models of D".

|               | 2740 km | 2789 km | 2839 km | 2891 km |
|---------------|---------|---------|---------|---------|
| $Q_p^{ak135}$ | 444     | 444     | 444     | 444     |
| $Q_s^{ak135}$ | 274     | 274     | 274     | 274     |
| $Q_p^{chQ9}$  | 233     | 233     | 233     | 233     |
| $Q_s^{chQ9}$  | 150     | 150     | 150     | 150     |
| $Q_p^{chQ10}$ | 121     | 121     | 121     | 121     |
| $Q_s^{chQ10}$ | 80      | 80      | 80      | 80      |
| $Q_p^{chQ11}$ | 172     | 172     | 171     | 172     |
| $Q_s^{chQ11}$ | 110     | 110     | 110     | 110     |
| $Q_p^{chQ13}$ | 200     | 200     | 200     | 200     |
| $Q_s^{chQ13}$ | 130     | 130     | 130     | 130     |

distance, the shape of the synthetic envelope still differs from the observation, top panel of Fig 6.3. All the synthetic envelopes from different Q models have a sharp Pdiff arrival and a gradually decaying coda instead of the gradually increasing then slowly decaying energy. This means that attenuation in the lowermost mantle also is not the only control key of our CDR observations.

### 6.3 Radial Extent of Heterogeneity

I have explored the effect of the topography of the CMB and attenuation in the lowermost mantle on the CDR simulation. Based on these experiments, I use a 2.0 deg half-distance and the chQ13 Earth model (high attenuation in the lowermost mantle, Table 6.2) to examine the radial extent of heterogeneity in the mantle.

I compare three different scattering models (Table 6.1). One scattering model only has scatterers in D". However, for this model the simulated CDRs, dotted line in Fig 6.4, cannot fit the observations at all. This test means that the fine-scale scatterers cannot only be in the lowermost mantle. The second scattering model only has scatterers in the upper mantle. This model almost can generate a good match. But the CDRs at the larger distances, 105 to 120 deg, using this model are

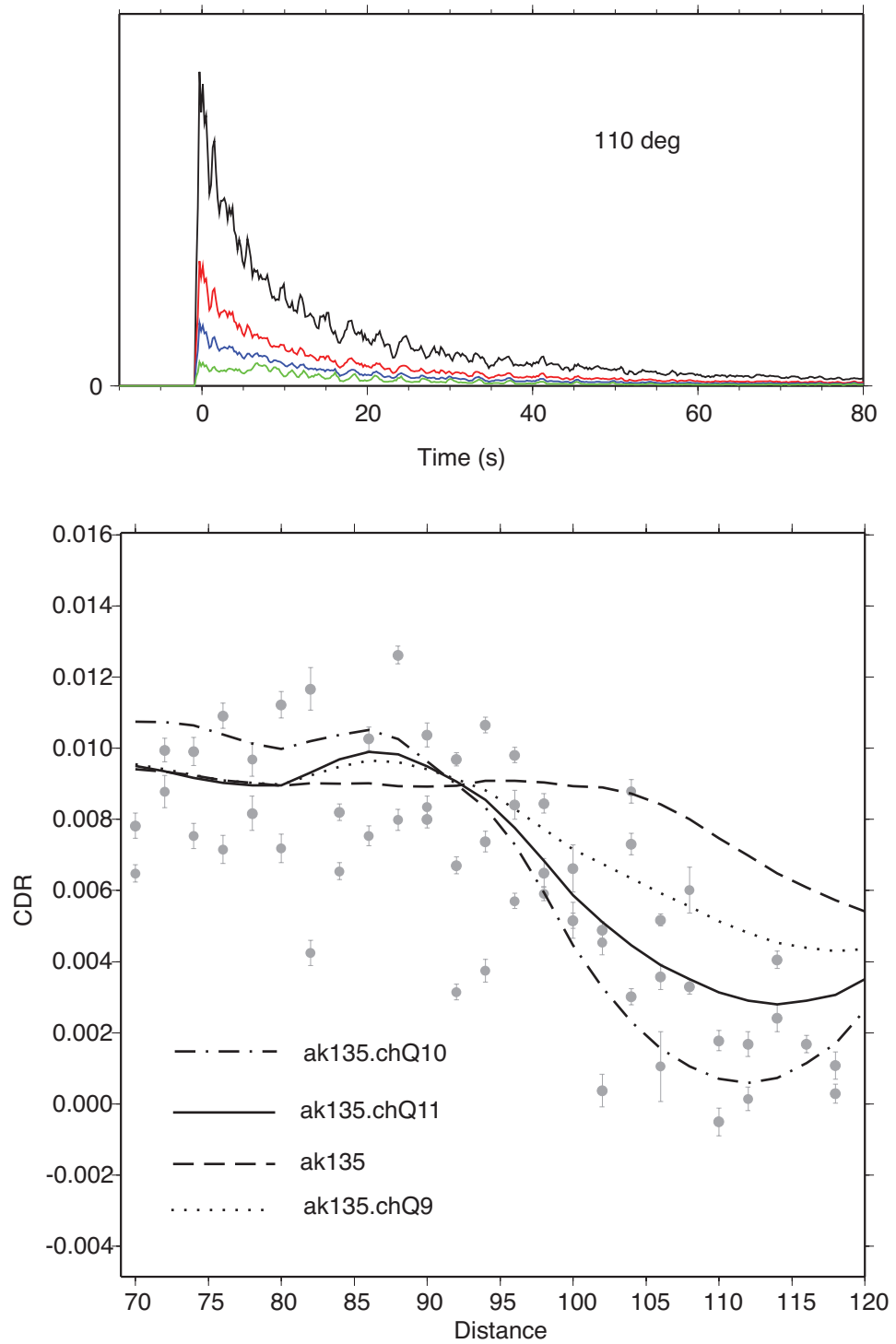


Figure 6.3: Bottom: CDR using different Q model for the lowermost mantle, Table 6.2. Top: Example of the synthetics at 110 deg using different Q model. Black: ak135. Blue: ak135.chQ9. Red: ak135.chQ11. Green: ak135.chQ10.

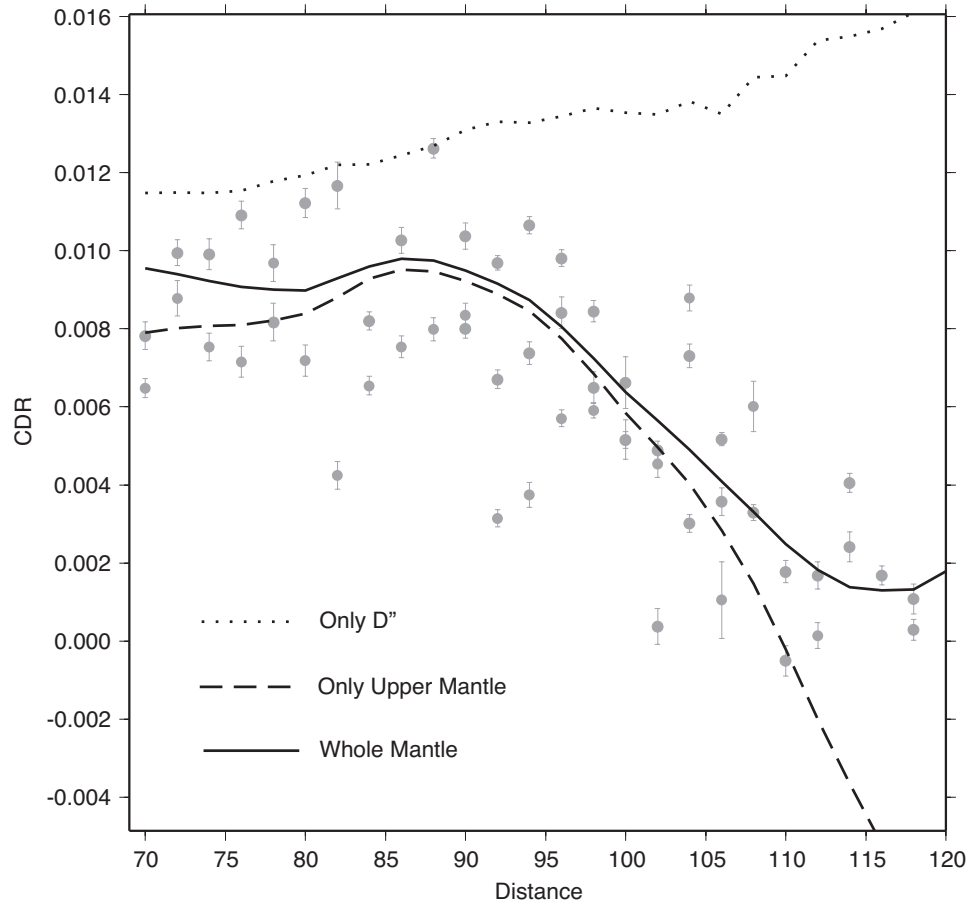


Figure 6.4: Detecting the distribution of scatterers by using the 2.0 half distance and the earth model with high attenuation in  $D''$ , chQ13, by matching the CDR observations.

obviously too small. After I add extra scatterers to the lowermost mantle to form a whole mantle scattering model, the CDR simulation can match the observations at all distances. Through this comparison, I can conclude that scatterers do not only exist in  $D''$ , but that scatterers in the upper mantle play a very important role in generating P/Pdiff coda. The whole mantle scattering model with two heterogeneous regions, upper mantle and  $D''$ , is the most reliable model.

## 6.4 Strength of the Scatterers in D''

Now I have explored the topography of the CMB, attenuation in D'', and the radial extent of the fine-scale heterogeneities. The next constraint on the deep mantle I try to address is the strength of the scatterers in D''. If D'' is a graveyard for slabs it might be expected that there is a high level of chemical heterogeneity here, and so the strength of the heterogeneity increases. Alternatively, perhaps a relatively mild level, such as that in the mid-mantle, is appropriate.

I use the chQ13 attenuation model, a 2.0 deg half distance, and the whole mantle scattering model with different  $dv/v$  in D'' to examine the effect of the strength of the scatterers. The test shows that it is not possible to have strong scatterers in the lowermost mantle, because the stronger scatterer provides too fast of a coda decay rate which cannot fit the observation, Fig 6.5. By comparing the synthetic envelopes, the reason for this is clear. The 3% velocity perturbation, the red curve in top panel of Fig 6.5, has the strongest coda energy compared to relatively weaker scatterers, black, blue, and green curves. However, the scatterer in D'' also cannot be too weak, for example the dotted line in Fig 6.5 using the scattering model with the same scatterer strength as the mid-mantle has a very slowly decaying coda energy between 110 to 120 deg. Very weak scatterers, 0.05% velocity perturbation, cannot preserve enough energy. Its energy quickly drops to a constant level, and ends in a very slow coda decay rate measurement.

## 6.5 Preferred Model

Through the exploration of the half-distance, attenuation in the lowermost mantle, the location of the fine-scale scatterers, and the strength of the small-scale scatterer in D'', I find that 2.0 deg half-distance,  $Q_p^{chQ13}$  in D'', and the whole mantle scattering model with 1% velocity perturbation in D'' is an adequate

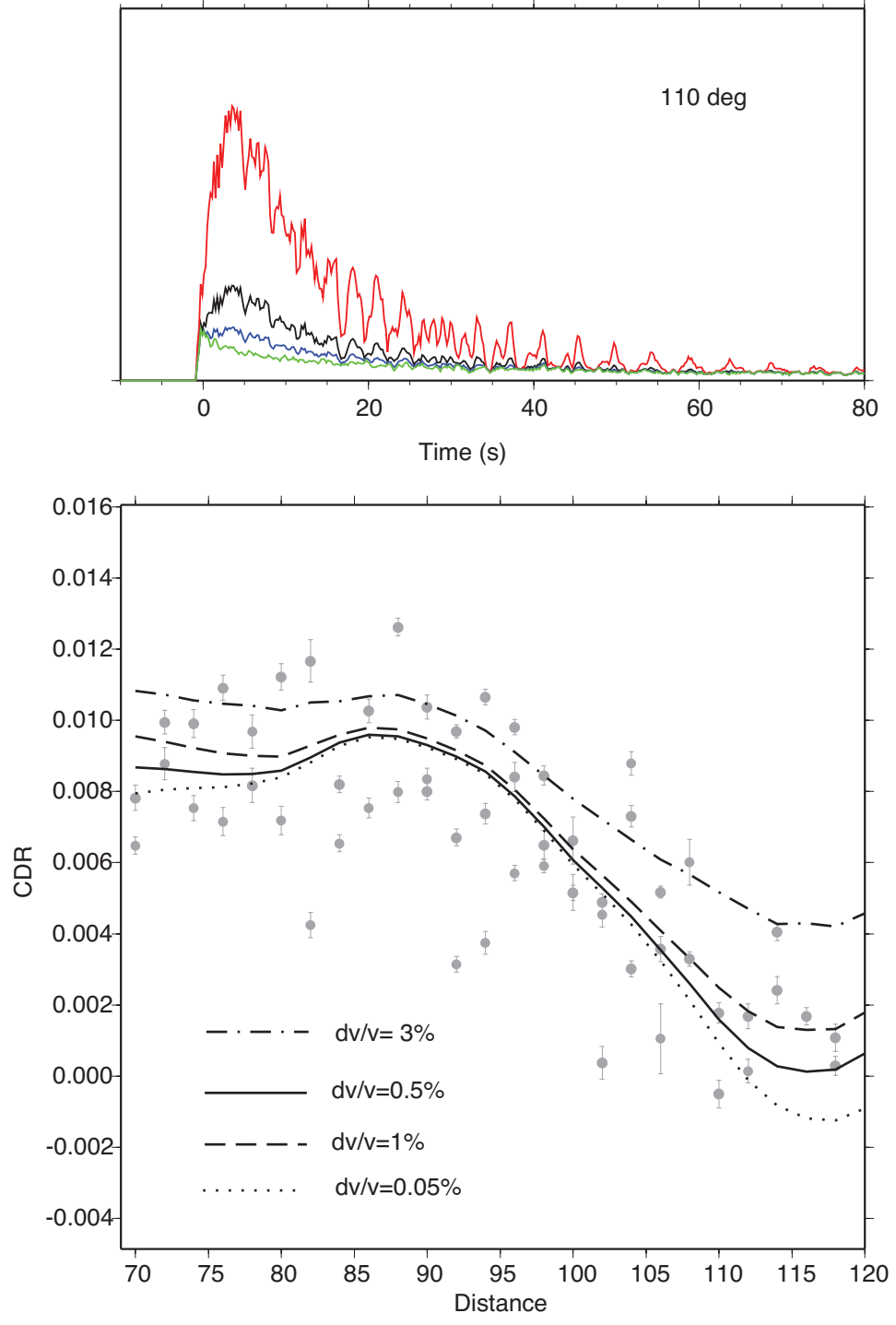


Figure 6.5: Bottom: CDRs uses different strength of the scatterers in  $D''$ , left. Expected amplitude, right. Top: Synthetic envelopes from different strength of the scatterers in  $D''$ . Red: 3% velocity perturbation in the  $D''$ . Blue: 0.5% velocity perturbation. Green: 0.05% velocity perturbation. Black: 1% perturbation.

combination, Fig 6.6.

However, this is not a unique combination. If I lower the half distance, or lower Q value in D'', or lower the scatterer strength in D'', I can provide a fit close to the observations. Around 2.0 deg,  $Q_p$  from 250 to 150, and  $dv/v$  from 1% to 0.5%, are the acceptable values for half distance, the attenuation in D'', and the scatterer strength in D'' respectively. Around 2.0 deg half distance suggests that the CMB has significant topography instead of a smooth boundary, consistent with previous work. The preferred attenuation model in D'' is close to the Q value in the asthenosphere. This reinforces the idea that D'' is a thermal boundary layer. Owing to the high temperature gradient in D'', a high attenuation is expected. My whole mantle scattering model agrees with previous work [*Earle and Shearer, 2001*]. This whole mantle scattering model supports the whole mantle convection hypothesis, that subduction injects the heterogeneity and the whole mantle convection segregates and brings the material down to the core mantle boundary.

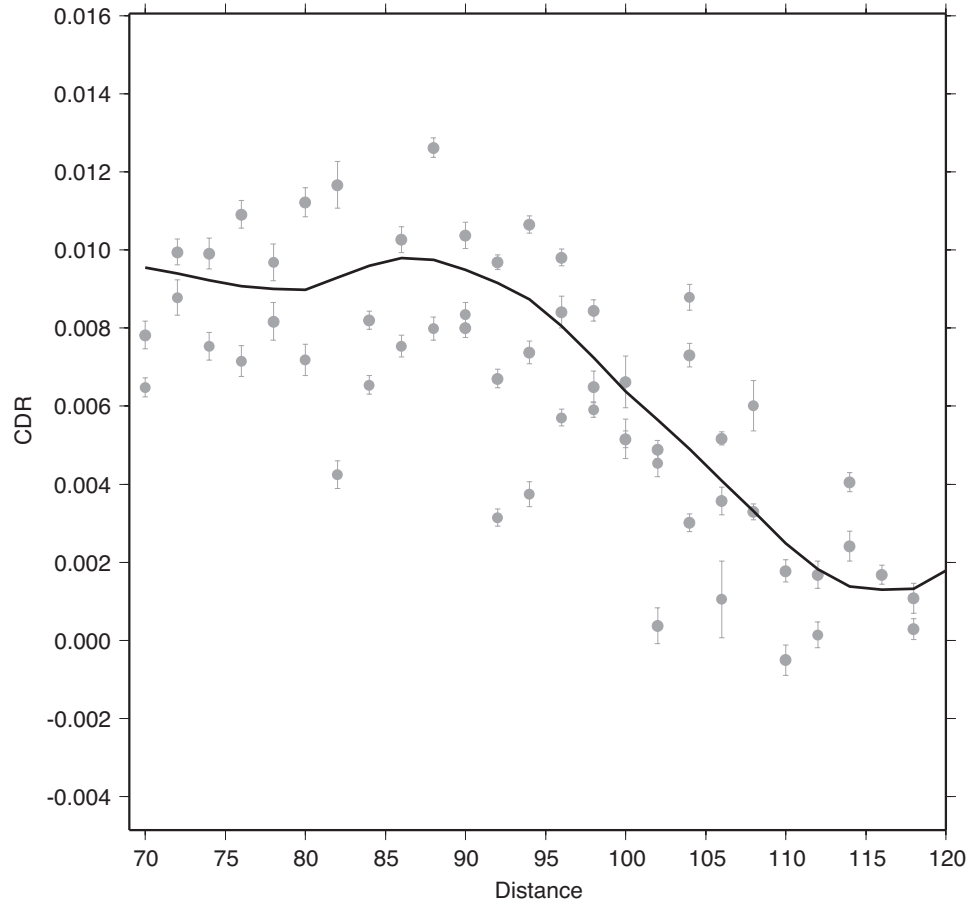


Figure 6.6: The best fit using 2.0 deg half distance, chQ13 attenuation model, Table 6.2, and the whole mantle scattering with  $dv/v$  equals 1%.

## Chapter 7: Conclusion

In this thesis, I analyzed seismograms recorded by the medium aperture array, YKA, in Canada, to determine P/Pdiff ray parameters and coda decay rates. This gave constraints about the distribution of scatterers in the mantle.

In Chapter 1, I described the goals of this thesis. The main goal is to detect the extent of fine-scale heterogeneities in the mantle. There is a debate about this question. Some studies suggest the lowermost mantle (D<sup>''</sup>) is a place concentrated with heterogeneities. Others prefer a more uniform, whole-mantle scattering model. Because this interesting question is important to understand mantle dynamics, it becomes the primary goal of my study. For the real Earth, the heterogeneity is not only one-dimensional. Instead, long-wavelength tomographic studies have shown the degree-two heterogeneity at the base of the mantle. Hence, my second goal is to detect the lateral variation of fine-scale heterogeneities in D<sup>''</sup> across the northwest Pacific.

In Chapter 2, I described the data set used in this thesis. Because the target of my study is fine-scale heterogeneity in the mantle, an array with uniform instruments and deployed in a geologically simple region can increase the signal-to-noise ratio and allow me to approach my goals. I downloaded 1,371 data with magnitudes 5.7 to 7.9 Mw in the distance range 50 deg to 120 deg for the years 1990 to 2006 recorded by the Yellowknife array in Canada from the CNDC AutoDRM. These 1,371 events occurred in the circum-Pacific “Ring of Fire”, Asia, Tonga-Fiji, South America, and Sumatra-Andaman regions, with mainly dip-slip focal mechanisms.

In Chapter 3, I used array processing techniques to detect the slowness of P/Pdiff for 1,371 earthquakes. I checked how velocity changes as a function of depth by binning the slowness observations for the events that occurred in Asia, South

America, and Tonga-Fiji. The radial comparison between the observed ray parameters and the predictions from the AK135 Earth model showed a good match. However, there is a significant lateral variation in ray parameter residuals for the bottom 50 km of the mantle. Events from Sumatra-Andaman and Tonga-Fiji reveal an Ultra-Low Velocity Zone (ULVZ) at the edge of the low P velocity region. From 230 to 290 deg in backazimuth,  $\delta V_p$  decreases from positive 2% to negative 6%. Then the  $\delta V_p$  remains the positive or near zero until 340 deg in backazimuth. The region with  $\delta V_p$  around negative 6% between 270 to 290 deg in backazimuth represents the ULVZ.

This ULVZ beneath the north Pacific is close to a boundary between the compositionally and thermally distinct patches of the lower mantle [Trampert *et al.*, 2004]. East of this boundary is a perovskite enriched, high-temperature region. West of the boundary is a perovskite depleted, low-temperature region. Previously, ULVZs have been interpreted as partial melt, and recent studies reveal the source for this partial melt. In this hypothesis, a ULVZ is caused by ponded, subducted mid-ocean ridge basalt (MORB) which is denser and has lower melting temperature than the surrounding material. The descending slabs beneath northeast Eurasia bring MORB deep in to the mantle, and mantle convection currents segregate and sweep the MORB. The ponded segregated MORB causes partial melt, which allows us to measure the velocity change.

The boundary of the chemically distinct pile from Trampert *et al.* [2004] is north of the boundary of the tomographically defined LLSVP. If we accept the tomographically defined LLSVP chemical boundary, the ULVZ detected in this work gives a clue about where the MORB comes from to form the ULVZ and the LLSVP. Several studies show that ULVZs occur near the edge of the LLSVP [Lay *et al.*, 2006; Rost *et al.*, 2005]. The ULVZ detected here is located in between the subduction regions of northeast Asia and the northern edge of the Pacific LLSVP.

This observation builds a bridge to connect the source, the subduction region, with the result, the ULVZ. This suggests that the ULVZ detected here is currently in transit, bringing segregated MORB to the edge of the Pacific LLSVP. In addition to the location of the ULVZ, the velocity reduction also supports this speculation. Usually, the P velocity reduction can reach up to 10% in the ULVZ, however, my ULVZ only has a 6% reduction. The edge of the chemically distinct LLSVP is thought to be the hottest region in the mantle, and as the MORB material approaches this spot the percentage of partial melt is expected to increase, thereby decreasing the velocity even more.

The detection of a ULVZ reported in Chapter 3 reveals existing chemical heterogeneities in the lowermost mantle. In Chapter 4, through examining the coda decay rate (CDR) changes, I get further details about the distribution of the fine-scale scatterers. Asia, South America, and Tonga-Fiji paths all show a negative relationship between the CDR and distance between 90 to 120 deg. This negative relationship for the larger distances suggests that there are more heterogeneities in the lowermost mantle. Considering their sampling region in the lowermost mantle, the segregated subducted slabs might be the main source causing this negative relationship. Asia and South America sample the subduction regions with the reconstructed paleosubducted slabs in the lowermost mantle [*Ricard et al.*, 1993; *Lithgow-Bertelloni and Richards*, 1998].

Nevertheless, in addition to the subducting regions my other data set from Tonga-Fiji samples the region beneath the Hawaii hotspot. Recent studies have shown that hotspots do not occur in the middle of the large low velocity anomalies. Hotspots more often locate at the edge of the chemically distinct LLSVP, as this is the hottest area. And this hottest area is due to the existence of the ponded segregated MORB swept from the subduction region. The root of the hotspot locates at the edge of LLSVP which is the accumulation region for the swept

MORB. Because of this I can observe the decreasing CDR as a function of increasing distance for the data set from Tonga-Fiji. Relative to the lowermost mantle, the mid-mantle is more homogeneous as the CDRs keep almost constant between 70 to 90 deg.

The CDRs from Asia, South America, and Tonga-Fiji paths show a radial distribution of fine-scale heterogeneities that is relatively homogeneous in the mid-mantle and heterogeneous in  $D''$ . The data set from Sumatra-Andaman and Tonga-Fiji regions sample the lowermost mantle. Its CDR variation character shows that there are more fine-scale scatterers beneath northeast Eurasia than beneath the north Pacific. As the radiation patterns for this data set do not have any correlation with the CDR variation feature, I can conclude that the observed lateral CDR feature is not due to the source. Since my CDR measurements are from the events shallower than 100 km, I also compare the CDR difference for the deep event and the shallow events to detect whether the anomaly comes from the deep mantle or the upper mantle near the sources. The deep events also yield the same CDR feature as the shallow event which means that the upper mantle heterogeneity is not the source of the observed CDR anomaly. However, my observed lateral CDR feature has a tight relationship with the reconstructed paleosubducted slabs in  $D''$ . The lowermost mantle beneath the northeast Eurasia with paleosubducted slabs has an even slower decaying coda compared to the lowermost mantle beneath the north Pacific.

After measuring the CDRs in Chapter 4, I describe a single scattering method for modeling them in Chapter 5. I divide the 3D Earth into equal voxels and connect each voxel, representing the location of the scatterer, to the fixed source and receiver. By summing all the possible source-voxel-receiver combinations, I produce a synthetic coda. In Chapter 5, I also tested some parameters to quantify their influence on the single scattering method, e.g. half distance for simulating

diffraction, adding PcP phases, the size of the voxel, source time function, and  $Q$  in the lower mantle. Since the single scattering method can save computational time and is accurate for whole mantle scattering, I use it to simulate the observed radial CDR anomaly and to constrain the properties of the scatterers in the mantle in Chapter 6.

The first parameter I constrained is the half distance. Using the synthetic seismograms from a frequency-wavenumber method (which assumes a smooth CMB) I find a 4.0 deg half distance. Based on this value, the compressional energy loses half of its energy for every 4.0 deg of travel along the CMB. However, this value cannot generate a good fit to the observations. The synthetic simulation prefers 2.0 deg half-distance. This smaller half distance suggests the existence of an irregular CMB that is not smooth.

In addition to this, I also constrained attenuation in the lowermost mantle. Constraining the attenuation in D'' is very helpful in understanding the relationship between core and mantle and the temperature in this region. My forward modeling results in a model with much higher attenuation in the lowermost mantle than the AK135 Earth model. *Fisher et al.* [2003] through studying the ScS-S differential attenuation and travel-time got high attenuation in D'' beneath Central America compared to PREM. *Resovsky et al.* [2005] gave the error bars for the global 1D  $Q$  file. Their study concluded that the  $Q_\kappa$  in the lowermost mantle is not infinity. The most likely  $Q_\kappa$  for the lower mantle is about 20000, and this value can yield a  $Q_p$  about 600. *Kazama et al.* [2008] also concluded that no attenuation,  $Q_p = \infty$  at the lower mantle cannot fit their travel time observations. However, high attenuation in the lowermost mantle,  $Q_p$  equals 585 or 40, can yield a very small travel-time error for their core phase observations.

In addition to the topography of the CMB and attenuation in D'', the synthetic simulation also gives a constraint on the radial distribution and strength of the

scatterers. My simulation prefers a whole mantle scattering model with the strongest scatterers in the upper mantle, a relatively homogeneous in the mid-mantle, and modest scattering in the lowermost mantle. The scatterers in the lowermost mantle play an important role in the modeling of the CDR. Without scatterers here, or weak scatterers, the model cannot provide a proper fit for the larger distances representing the very bottom of the mantle. However, the scatterer in the lowermost mantle also cannot be too strong as my simulation shows that 3% velocity perturbation for the lowermost mantle yields too rapid CDR for all distances from 70 to 120 deg. 1% to 0.5% velocity perturbation for the lowermost mantle, 400 km above the CMB, 2 - 3% velocity perturbation for the upper mantle is my preferred model.

The combination of whole mantle scattering with 1% velocity perturbation in D", 2.0 deg half distance, and  $Q_p = 200$  in D" is my favorite model for the CDR simulation. Nevertheless, this is not unique as three major parameters, velocity perturbation, attenuation, and the half distance, all affect the simulation. There is a range for these parameters to generate a good CDR fit. My simulation suggests that the velocity in D" cannot be too strong,  $dv/v$  can be varied between 1% and 0.5%; the attenuation in D" is very strong, varying from 250 to 150 for  $Q_p$ ; and the half distance is around 2.0 deg.

Through the observation and forward modeling, I have reached two goals of this study. However, this work just reveals part of the mystery of the heterogeneous mantle. There is much work to do in the future. For example, in Chapter 3 I observed an ULVZ, but the exact location and dimensions of the ULVZ are not clear, and the thickness of the ULVZ still is unknown. In the future, I can try to detect the thickness and the exact location of the ULVZ by using crossing ray paths and broader frequency band information. For the CDR observations, I gave the coda intercept as a function of distance in Chapter 4, but I didn't model it.

Modeling the coda intercept also can be a future work.

## **Appendix A:**

More ULVZ detection figures.

ULVZ detection at 1 Hz using YKA. Global P and S wave tomography results.

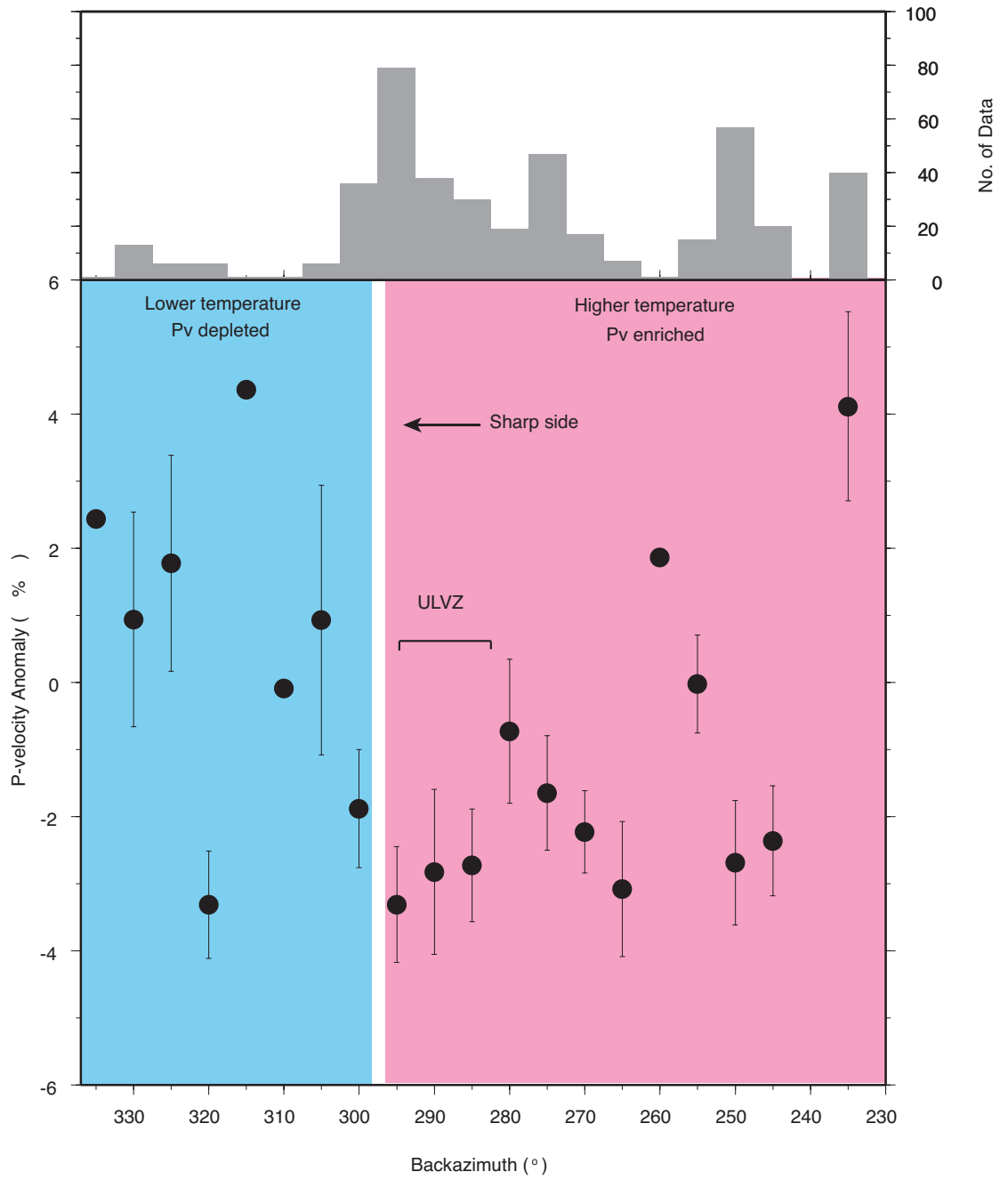


Figure A.1:  $\delta V_p$  variation at 1 Hz, and the location of ULVZ.

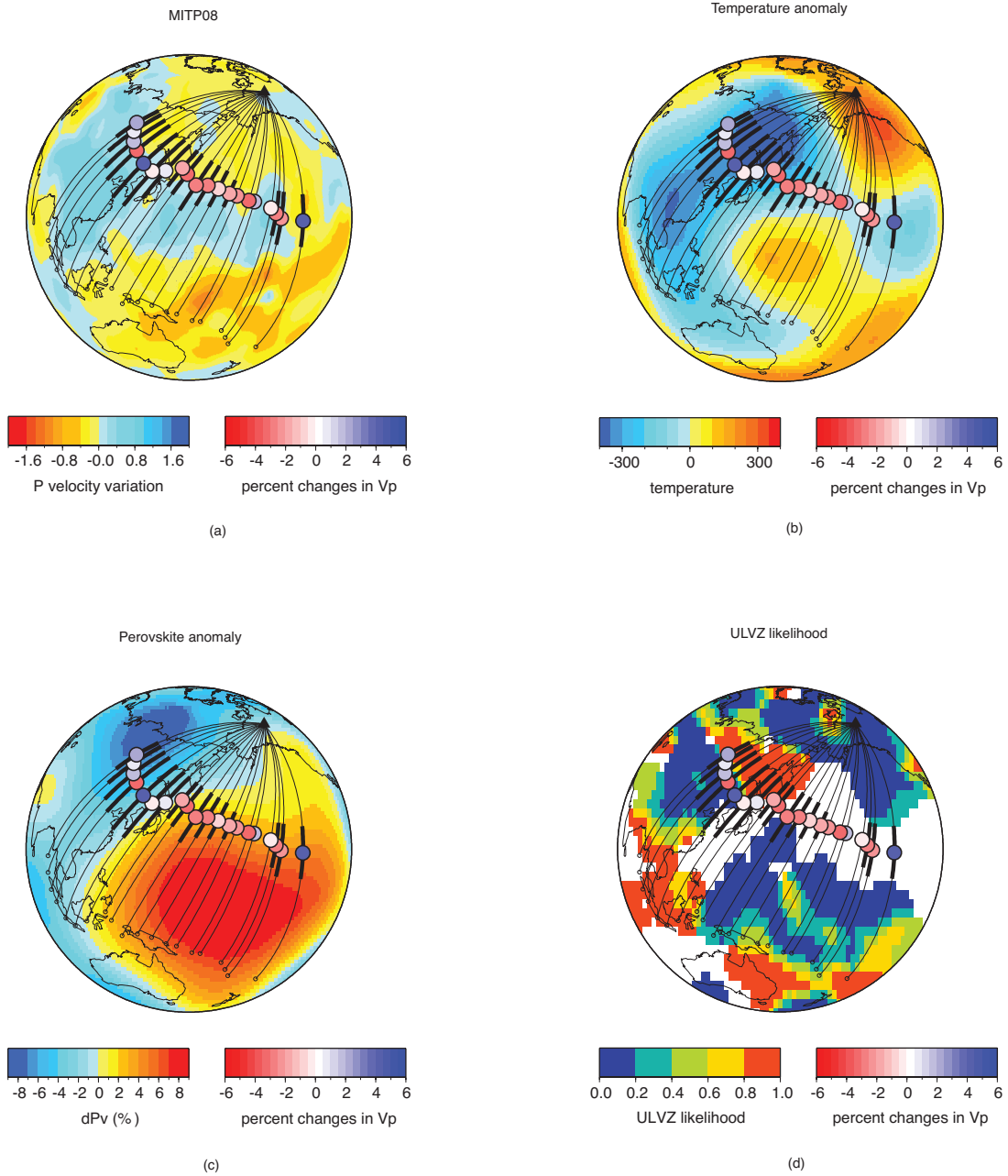


Figure A.2: Observed  $P$  velocity variation against  $P$  tomography model, MITP08 [Li *et al.*, 2008a](a), temperature in the bottom 1000 km of the mantle [Trampert *et al.*, 2004](b), perovskite anomaly at the bottom of the mantle [Trampert *et al.*, 2004](c), and observed ULVZ [Thorne and Garnero, 2004](d) at 1 Hz.

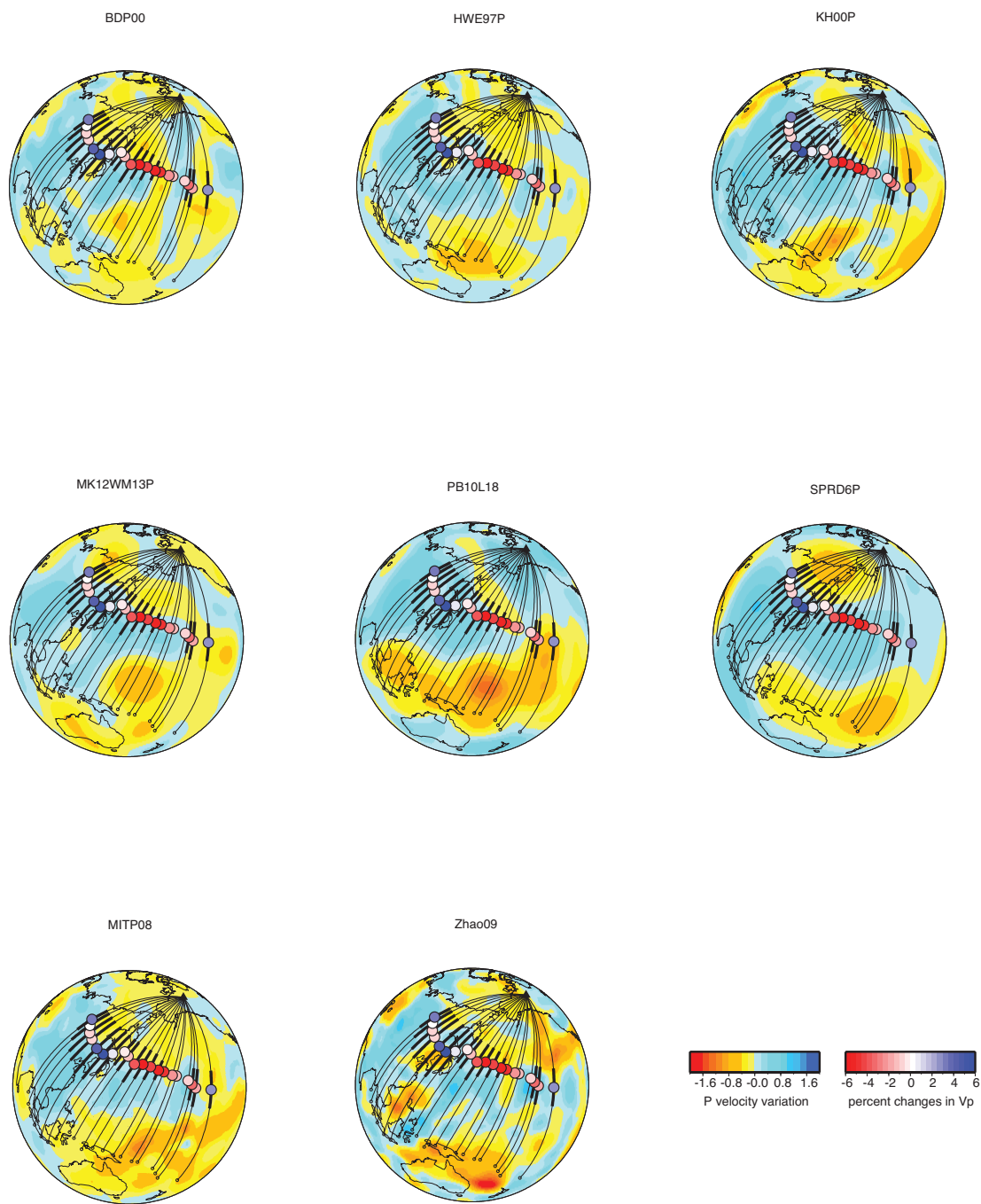


Figure A.3:  $P$  tomography models and observed lateral velocity variation in the bottom 20 km. BDP00 [Becker and Boschi, 2002], HWE97P [van der Hilst et al., 1997], KH00P [Kárason and van der Hilst, 2001], MK12WM13P [Su and Dziewonski, 1997], PB10L18 [Masters et al., 2000], SPRD6P [Ishii and Tromp, 2004], MITP08 [Li et al., 2008a], Zhao09 [Zhao, 2008].

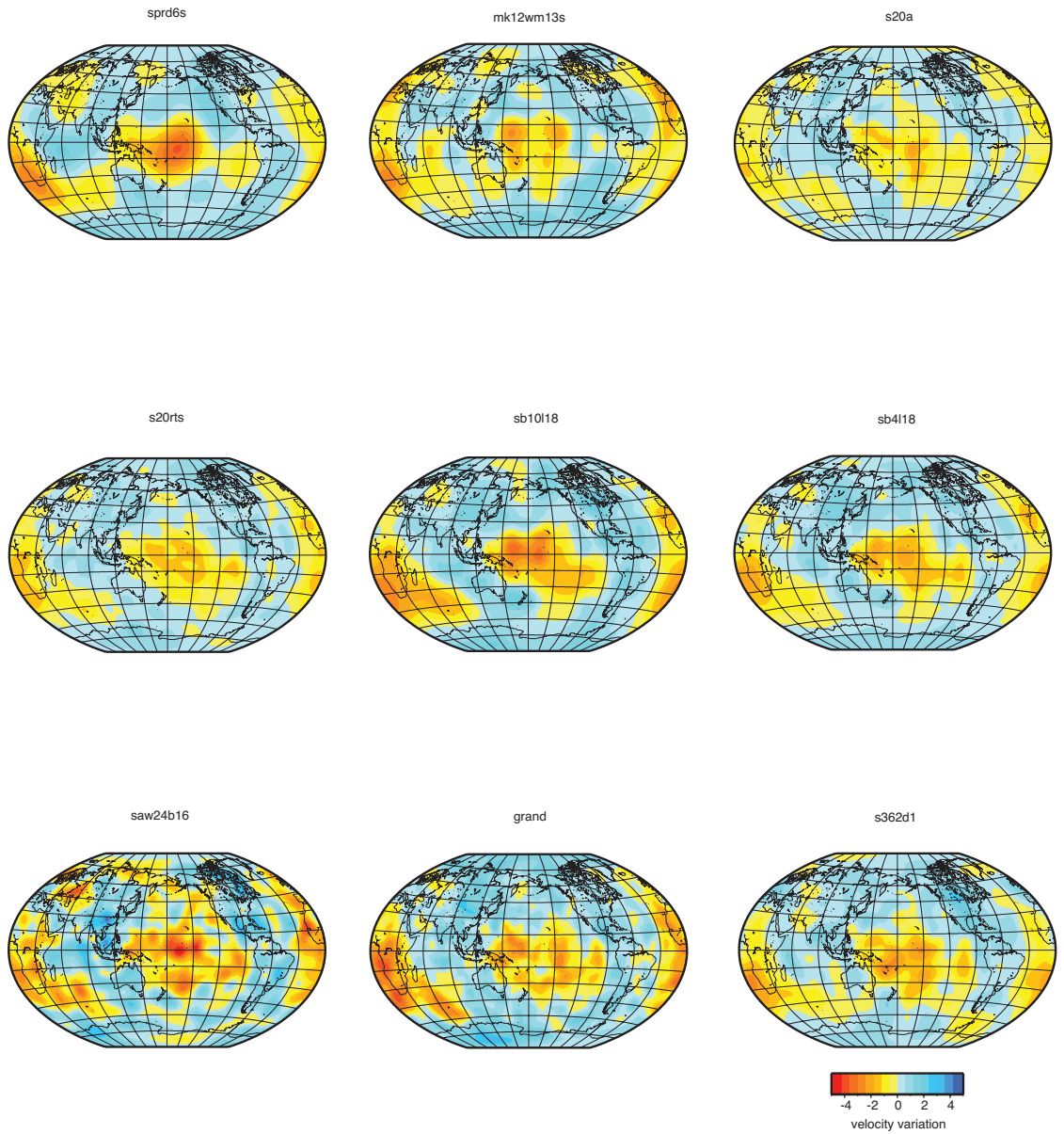


Figure A.4:  $S$  tomography models. sprd6s [Ishii and Tromp, 2004], mk12wm13s [Su and Dziewonski, 1997], s20a [Ekström and Dziewonski, 1998], s20rts [Ritsema and van Heijst, 2000], sb10118 [Masters et al., 2000], sb4118 [Masters et al., 1999], saw24b16 [Mégnin and Romanowicz, 2000], grand [Grand et al., 1997], s362d1 [Gu et al., 2001].

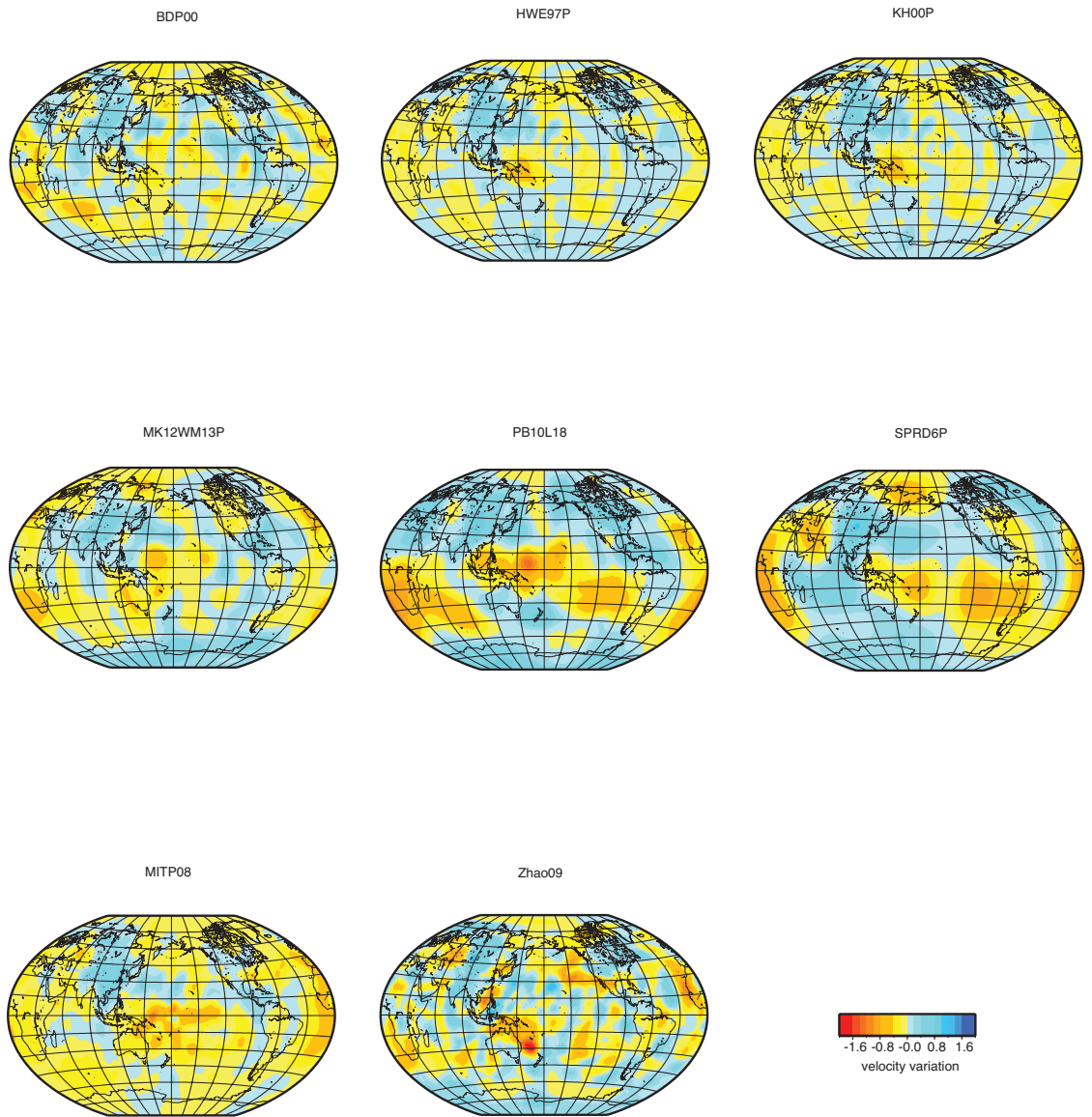


Figure A.5:  $P$  tomography models. BDP00 [Becker and Boschi, 2002], HWE97P [van der Hilst et al., 1997], KH00P [Kárason and van der Hilst, 2001], MK12WM13P [Su and Dziewonski, 1997], PB10L18 [Masters et al., 2000], SPRD6P [Ishii and Tromp, 2004], MITP08 [Li et al., 2008a], Zhao09 [Zhao, 2008].

## References

- Aki, K., Analysis of seismic coda of local earthquakes as scattered waves, *J. Geophys. Res.*, *74*, 615–631, 1969.
- Aki, K., and B. Chouet, Origin of coda waves: source attenuation and scattering effects, *J. Geophys. Res.*, *80*, 3322–3342, 1975.
- Aki, K., and P. G. Richards, *Quantitative seismology theory and methods*, W. H. Freeman and Company, 1980.
- Aki, K., and M. Tsujiura, Correlation study of near earthquake waves, *Bull. Earthq. Res. Inst. Univ. Tokyo*, *37*, 207–232, 1959.
- Aki, K., M. Tsujiura, M. Hori, and K. Gotô, Spectral study of near earthquake waves, *Bull. Earthq. Res. Inst. Univ. Tokyo*, *36*, 71–98, 1958.
- Akins, J. A., S. N. Luo, P. D. Asimow, and T. J. Ahrens, Shock-induced melting of MgSiO<sub>3</sub> perovskite and implications for melts in Earth's lowermost mantle, *Geophys. Res. Lett.*, *31*, doi:10.1029/2004GL020,237, 2004.
- Avants, M., T. Lay, and E. J. Garnero, A new probe of ULVZ S-wave velocity structure: Array stacking of ScS waveforms, *Geophys. Res. Lett.*, *33*, doi:10.1029/2005GL024,989, 2006.
- Bataille, K., and S. M. Flatté, Inhomogeneities near the core-mantle boundary inferred from short-period scattered *PKP* waves recorded at the global digital seismograph network, *J. Geophys. Res.*, *93*, 15,057–15,064, 1988.
- Bataille, K., and F. Lund, Strong scattering of short-period seismic waves by the core-mantle boundary and the P-diffracted wave, *Geophys. Res. Lett.*, *23*, 2413–2416, 1996.
- Bataille, K., R. Wu, and S. Flatte, Inhomogeneities near the core-mantle boundary evidenced from scattered waves: A review, *PAGEOPH*, *132*, 151–174, 1990.
- Becker, T. W., and L. Boschi, A comparison of tomographic and geodynamic mantle models, *Geochem. Geophys. Geosys.*, *3*, doi:2001GC000,168, 2002.
- Berryman, J. G., Seismic velocity decrement ratios for regions of partial melt in the lower mantle, *Geophys. Res. Lett.*, *27*, 421–424, 2000.
- Bijwaard, H., W. Spakman, and E. R. Engdahl, Closing the gap between regional and global travel time tomography, *J. Geophys. Res.*, *103*, 30,055–30,078, 1998.
- Boatwright, J., and G. L. Choy, Teleseismic estimates of the energy radiated by shallow earthquakes, *J. Geophys. Res.*, *91*, 2095–2112, 1986.

- Bondár, I., R. G. North, and G. Beall, Teleseismic slowness-azimuth station corrections for the international monitoring system seismic network, *Bull. Seismol. Soc. Am.*, *89*, 989–1003, 1999.
- Boore, D. M., Love waves in nonuniform wave guides: finite difference calculations, *J. Geophys. Res.*, *75*, 1512–1527, 1970.
- Christensen, U. R., and A. W. Hofmann, Segregation of subducted oceanic crust in the convecting mantle, *J. Geophys. Res.*, *99*, 19,867–19,884, 1994.
- Cleary, J. R., and R. A. W. Haddon, Seismic wave scattering near the core-mantle boundary: A new interpretation of precursors to *PKIKP*, *Nature*, *240*, 549–551, 1972.
- Corbishley, D. J., Structure under seismic arrays, *Geophys. J. R. astr. Soc.*, *21*, 415–425, 1970.
- Cormier, V. F., Time domain modeling of *PKIKP* precursors for constraints on the heterogeneity in the lowermost mantle, *Geophys. J. Int.*, *212*, 725–736, 1995.
- Cormier, V. F., Anisotropy of heterogeneity scale lengths in the lower mantle from *PKIKP* precursors, *Geophys. J. Int.*, *136*, 373–384, 1999.
- Davies, D., E. J. Kelly, and J. R. Filson, Vespa process for analysis of seismic signals, *Nature Phys. Sci.*, *232*, 8–13, 1971.
- Doornbos, D. J., On seismic wave scattering by a rough core-mantle boundary, *Geophys. J. R. astr. Soc.*, *53*, 643–662, 1978.
- Doornbos, D. J., and N. J. Vlaar, Regions of seismic wave scattering in the Earth's mantle and precursors to *PKP*, *Nature Phys. Sci.*, *243*, 58–61, 1973.
- Earle, P. S., and P. M. Shearer, Distribution of fine-scale mantle heterogeneity from observations of *Pdiff* coda, *Bull. Seismol. Soc. Am.*, *91*, 1875–1881, 2001.
- Ekström, G., and A. M. Dziewonski, The unique anisotropy of the Pacific upper mantle, *Nature*, *394*, 168–172, 1998.
- Fisher, J. L., M. E. Wysession, and K. M. Fischer, Small-scale lateral variations in *D''* attenuation and velocity structure, *Geophys. Res. Lett.*, *30*, doi:10.1029/2002GL016,179, 2003.
- Fuchs, K., and G. Müller, Computation of synthetic seismograms with the reflectivity method and comparison with observations, *Geophys. J. R. astr. Soc.*, *23*, 417–433, 1971.
- Garnero, E., and D. Helmberger, Further constraints and uncertainties in modeling a mantle basal layer of ultra-low velocities, *J. Geophys. Res.*, *103*, 12,495–509, 1998.

- Garnero, E. J., and D. V. Helmberger, A very slow basal layer underlying large-scale low velocity anomalies in the lower mantle beneath the Pacific: Evidence from core phases, *Phys. Earth Planet Int.*, *91*, 161–176, 1995.
- Garnero, E. J., and A. K. McNamara, Structure and dynamics of Earth’s lower mantle, *Science*, *320*, 626–628, 2008.
- Garnero, E. J., S. P. Grand, and D. V. Helmberger, Low P-wave velocity at the base of the mantle, *Geophys. Res. Lett.*, *20*, 1843–1846, 1993.
- Garnero, E. J., J. Revenaugh, Q. Williams, T. Lay, and L. H. Kellogg, Ultralow Velocity Zone at the Core-Mantle Boundary, in *The Core-Mantle Boundary Region*, edited by M. Gurnis, M. Wyssession, E. Knittle, and B. Buffett, pp. 319–334, American Geophysical Union Monograph, 1998.
- Gilbert, F., and D. V. Helmberger, Generalized ray theory for a layered sphere, *Geophys. J. R. astr. Soc.*, *27*, 58–80, 1972.
- Grand, S., Mantle shear structure beneath the Americas and surrounding oceans, *J. Geophys. Res.*, *99*, 11,591 – 11,621, 1994.
- Grand, S. P., Mantle shear-wave tomography and the fate of subducted slabs, *Phil. Trans. R. Soc. London*, *360*, 2475–2491, 2002.
- Grand, S. P., R. D. vander Hilst, and S. Widiyantoro, High resolution global tomography: a snapshot of convection in the Earth, *GSA Today*, *7*, 1–7, 1997.
- Gu, Y. J., A. M. Dziewonski, W. J. Su, and G. Ekström, Models of the mantle shear velocity and discontinuities in the pattern of lateral heterogeneities, *J. Geophys. Res.*, *106*, 11,169–11,199, 2001.
- Haddon, R. A. W., and J. R. Cleary, Evidence for scattering of seismic *PKP* waves near the mantle-core boundary, *Phys. Earth Planet Int.*, *8*, 211–234, 1974.
- Hedlin, M., and P. Shearer, Probing mid-mantle heterogeneity using PKP coda waves, *Phys. Earth Planet Int.*, *130*, 195–208, 2002.
- Hedlin, M. A. H., and P. M. Shearer, An analysis of large-scale variations in small-scale mantle heterogeneity using Global Seismographic Network recordings of precursors to PKP, *J. Geophys. Res.*, *105*, 655–673, 2000.
- Hedlin, M. A. H., P. M. Shearer, and P. S. Earle, Seismic evidence for small-scale heterogeneity throughout Earth’s mantle, *Nature*, *387*, 145–150, 1997.
- Herrmann, R. B., Computer programs in seismology, [www.eas.slu.edu/People/RBHerrmann/CPS330.html](http://www.eas.slu.edu/People/RBHerrmann/CPS330.html), 2007.
- Hirose, K., Y. Fei, Y. Ma, and H.-K. Mao, The fate of subducted basaltic crust in the Earth’s lower mantle, *Nature*, *397*, 53–56, 1999.

- Hirose, K., N. Takafuji, N. Sata, and Y. Ohishi, Phase transition and density of subducted MORB crust in the lower mantle, *Earth Planet. Sci. Lett.*, *237*, 239–251, 2005.
- Ishii, M., and J. Tromp, Constraining large-scale mantle heterogeneity using mantle and inner-core sensitive normal modes, *Phys. Earth Planet Int.*, *146*, 113–124, 2004.
- Káráson, H., and R. D. van der Hilst, Constraints on mantle convection from seismic tomography, pp. 277–288, 2000.
- Káráson, H., and R. D. van der Hilst, Tomographic imaging of the lowermost mantle with differential times of refracted and diffracted core phases (PKP,  $P_{diff}$ ), *J. Geophys. Res.*, *106*, 6569–6587, 2001.
- Kazama, T., H. Kawakatsu, and N. Takeuchi, Depth-dependent attenuation structure of the inner core inferred from short-period Hi-net data, *Phys. Earth Planet Int.*, *167*, 155–160, 2008.
- Kennett, B. L. N., and N. J. Kerry, Seismic waves in a stratified half space, *Geophys. J. R. astr. Soc.*, *57*, 557–583, 1979.
- Kennett, B. L. N., E. R. Engdahl, and R. Buland, Constraints on seismic velocities in the Earth from travel times, *Geophys. J. Int.*, *122*, 108–124, 1995.
- Knopoff, L., F. Schwab, and E. Kausel, Interpretation of Lg, *Geophys. J. R. Astr. Soc.*, *33*, 389–404, 1973.
- Koper, K. D., and M. L. Pyle, Observations of PKiKP/PcP amplitude ratios and implications for Earth structure at the boundaries of the liquid core, *J. Geophys. Res.*, *109*, doi:10.1029/2003JB002,750, 2004.
- Koper, K. D., M. L. Pyle, and J. M. Franks, Constraints on aspherical core structure from PKiKP-PcP differential travel times, *J. Geophys. Res.*, *108*, doi:10.1029/2002JB001,995, 2003.
- Koper, K. D., J. Franks, and M. Dombrovskaya, Evidence for small-scale heterogeneity in Earth’s inner core from a global study of PKiKP coda waves, *Earth Planet. Sci. Lett.*, *228*, 227–241, 2004.
- Lay, T., J. Herndlund, E. J. Garnero, and M. S. Thorne, A post-perovskite lens and D” heat flux beneath the central Pacific, *Science*, *314*, 1272–1276, 2006.
- Lei, J., and D. Zhao, A new insight into the Hawaiian plume, *Earth Planet. Sci. Lett.*, *241*, 438–453, 2006.
- Leyton, F., and K. D. Koper, Using PKiKP coda to determine inner core structure: 2. Determination of  $Q_c$ , *J. Geophys. Res.*, *112*, doi:10.1029/2006JB004,370, 2007a.

- Leyton, F., and K. D. Koper, Using PKiKP coda to determine inner core structure: 1. Synthesis of coda envelopes using single-scattering theories, *J. Geophys. Res.*, *112*, doi:10.1029/2006JB004369, 2007b.
- Leyton, F., K. D. Koper, L. Zhu, and M. Dombrovskaya, On the lack of seismic discontinuities in the inner core, *Geophys. J. Int.*, *162*, 779–786, 2005.
- Li, C., R. D. van der Hilst, and M. N. Toksöz, Constraining P-wave velocity variations in the upper mantle beneath Southeast Asia, *Phys. Earth Planet Int.*, *154*, 180–195, 2006.
- Li, C., R. D. van der Hilst, E. R. Engdahl, and S. Burdick, A new global model for P wave speed variations in Earth’s mantle, *Geochem. Geophys. Geosyst.*, *9*, doi:doi:10.1029/2007GC001806, 2008a.
- Li, C., R. D. van der Hilst, A. S. Meltzer, and E. R. Engdahl, Subduction of the Indian lithosphere beneath the Tibetan Plateau and Burma, *Earth Planet. Sci. Lett.*, pp. 157–168, 2008b.
- Lithgow-Bertelloni, C., and M. A. Richards, Dynamics of Cenozoic and Mesozoic plate motions, *Reviews of Geophysics*, *36*, 27–78, 1998.
- Manchee, E. B., and D. H. Weichert, Epicentral uncertainties and detection probabilities from the Yellowknife seismic array data, *Bull. Seismol. Soc. Am.*, *58*, 1359–1377, 1968.
- Margerin, L., and G. Nolet, Multiple scattering of high-frequency seismic waves in the deep Earth: PKP precursors analysis and inversion for mantle granularity, *J. Geophys. Res.*, *108*, 2514, 2003a.
- Margerin, L., and G. Nolet, Multiple scattering of high-frequency seismic waves in the deep Earth: Modeling and numerical examples, *J. Geophys. Res.*, *108*, doi:10.1029/2002JB001974, 2003b.
- Masters, G., H. Bolton, and G. Laske, Joint seismic tomography for P and S velocities: How pervasive are chemical anomalies in the mantle?, *Eos Trans. AGU*, *80*, S14, 1999.
- Masters, G., G. Laske, H. Bolton, and A. Dziewonski, The relative behavior of shear velocity, bulk sound velocity, and compressional velocity in the mantle: Implications for chemical and thermal structure, in *Earth’s deep interior: Mineral physics and tomography from the atomic to the global scale*, edited by S.-I. Karato, pp. 63–88, Washington, D.C., American Geophysical Union, 2000.
- McNamara, A. K., and S. Zhong, Thermochemical structures within a spherical mantle: superplumes or piles?, *J. Geophys. Res.*, *109*, doi:10.1029/2003JB002847, doi:doi:10.1029/2003JB002847, 2004.

- McNamara, A. K., and S. Zhong, Thermochemical piles under Africa and the Pacific, *Nature*, *437*, 1136–1139, 2005.
- Mégnin, C., and B. Romanowicz, The shear velocity structure of the mantle from the inversion of body, surface, and higher modes waveforms, *Geophys. J. Int.*, *143*, 709–728, 2000.
- Menke, W., *Geophysical Data Analysis: Discrete Inverse Theory*, pp. 96–97, Academic Press, Inc., San Diego, 1989.
- Mori, J., and D. V. Helmberger, Localized boundary layer below the mid-Pacific velocity anomaly identified from a PcP precursor, *J. Geophys. Res.*, *100*, 20,359–20,365, 1995.
- Nakagawa, T., and P. J. Tackley, The interaction between the post-perovskite phase change and a thermo-chemical boundary layer near the core-mantle boundary, *Earth Planet. Sci. Lett.*, *238*, 204–216, 2005.
- Nolet, G., R. Allen, and D. Zhao, Mantle plume tomography, *Chemical Geology*, *241*, 248–263, 2007.
- Ren, Y., E. Stutzmann, R. D. van der Hilst, and J. Besse, Understanding seismic heterogeneities in the lower mantle beneath the Americas from seismic tomography and plate tectonic history, *J. Geophys. Res.*, *112*, doi:10.1029/2005JB004,154, 2007.
- Resovsky, J., J. Trampert, and R. D. V. der Hilst, Error bars for the global seismic Q profile, *Earth Planet. Sci. Lett.*, *230*, 413–423, 2005.
- Revenaugh, J., and R. Meyer, Seismic evidence of partial melt within a possibly ubiquitous low velocity layer at the base of the mantle, *Science*, *277*, 670–673, 1997.
- Ricard, Y., M. Richards, C. Lithgow-Bertelloni, and Y. LeStunff, A geodynamic model of mantle mass heterogeneities, *J. Geophys. Res.*, *98*, 21,895–21,909, 1993.
- Ritsema, J., and H. J. van Heijst, Seismic imaging of structural heterogeneity in Earth’s mantle: Evidence for large-scale mantle flow, *Science Progress*, *83*, 243–259, 2000.
- Rost, S., and J. Revenaugh, Small-scale ultralow-velocity zone structure imaged by ScP, *J. Geophys. Res.*, *108*, doi:10.1029/2001JB001,627, 2003.
- Rost, S., and T. Thomas, Array seismology: methods and applications, *Rev. Geophys.*, *40*, doi:10.1029/2000RG000,100, 2002.
- Rost, S., and M. Weber, A reflector at 200 km depth beneath the NW Pacific, *Geophys. J. Int.*, *147*, 12–28, 2001.

- Rost, S., and M. Weber, The upper mantle transition zone discontinuities in the Pacific as determined by short-period array data, *Earth Planet. Sci. Lett.*, *204*, 347–361, 2002.
- Rost, S., E. J. Garnero, Q. Williams, and M. Manga, Seismic constraints on a possible plume root at the core-mantle boundary, *Nature*, *435*, 666–669, 2005.
- Rost, S., E. J. Garnero, and Q. Williams, Fine scale ultra-low velocity zone structure from high-frequency seismic array data, *J. Geophys. Res.*, *111*, doi:10.1029/2005JB004,088, 2006a.
- Rost, S., M. S. Thorne, and E. J. Garnero, Imaging global seismic phase arrivals by stacking array processed short-period data, *Seismol. Res. Lett.*, *77*, 697–707, 2006b.
- Sato, H., Energy propagation including scattering effects single isotropic scattering approximation, *J. Phys. Earth*, *25*, 27–41, 1977.
- Sato, H., and M. C. Fehler, *Seismic Wave Propagation and Scattering in the Heterogeneous Earth*, Springer, 1998.
- Schimmel, M., and H. Paulssen, Noise reduction and detection of weak, coherent signals through phase-weighted stacks, *Geophys. J. Int.*, *130*, 497–505, 1997.
- Scott, P., and D. Helmberger, Applications of the Kirchhoff-Helmholtz integral to problems in seismology, *Geophys. J. R. astr. Soc.*, *72*, 237–254, 1982.
- Shearer, P. M., and P. S. Earle, The global short-period wavefield modeled with a Monte Carlo seismic phonon method, *Geophys. J. Int.*, *158*, 1103–1117, 2004.
- Shearer, P. M., M. A. H. Hedlin, and P. S. Earle, PKP and PKKP precursor observations; implications for the small-scale structure of the deep mantle and core, in *The Core-Mantle Boundary Region, Geodynamics Series 28*, pp. 37–55, American Geophysical Union, 1998.
- Smith, W. D., The application of finite element analysis to body wave propagation problems, *Geophys. J. R. astr. Soc.*, *42*, 747–768, 1974.
- Su, W. J., and A. M. Dziewonski, Simultaneous inversion for 3-D variations in shear and bulk velocity in the mantle, *Phys. Earth Planet Int.*, *100*, 135–156, 1997.
- Thomas, C., M. Weber, C. W. Wicks, and F. Scherbaum, Small scatterers in the lower mantle observed at German broadband arrays, *J. Geophys. Res.*, *104*, 15,073–15,088, 1999.
- Thomas, C., T. Heesom, and J. M. Kendall, Investigating the heterogeneity of the D" region beneath the northern Pacific using a seismic array, *J. Geophys. Res.*, *107*, doi:10.1029/2000JB00,021, 2002.

- Thorne, M. S., and E. J. Garnero, Inferences on ultralow-velocity zone structure from a global analysis of SPdKS waves, *J. Geophys. Res.*, *109*, doi:10.1029/2004JB003,010, 2004.
- Thorne, M. S., E. J. Garnero, and S. P. Grand, Geographic correlation between hot spots and deep mantle lateral shear-wave velocity gradients, *Phys. Earth Planet Int.*, *146*, 47–63, 2004.
- Tono, Y., and K. Yomogida, Complex scattering at the core-mantle boundary observed in short-period diffracted waves, *J. Phys. Earth*, *44*, 729–744, 1996.
- Tono, Y., and K. Yomogida, Origin of short-period signals following P-diffracted waves: A case study of the 1994 Bolivian deep earthquake, *Phys. Earth Planet Int.*, *103*, 1–16, 1997.
- Trampert, J., F. Deschamps, J. Resovsky, and D. A. Yuen, Probabilistic tomography maps chemical heterogeneities throughout the mantle, *Science*, *306*, 853–856, 2004.
- van der Hilst, R. D., R. Engdahl, W. Spakman, and G. Nolet, Tomographic imaging of subducted lithosphere below northwest Pacific island arcs, *Nature*, *353*, 733–739, 1991.
- van der Hilst, R. D., S. Widiyantoro, and E. R. Engdahl, Evidence for deep mantle circulation from global tomography, *Nature*, *386*, 578–584, 1997.
- Vidale, J. E., and P. Earle, Fine-scale heterogeneity in the Earth’s inner core, *Nature*, *404*, 273–275, 2000.
- Vidale, J. E., and P. S. Earle, Evidence for inner-core rotation from possible changes with time in PKP coda, *Geophys. Res. Lett.*, *32*, L01,309, doi:doi:10.1029/2004GL021240, 2005.
- Vidale, J. E., and M. A. H. Hedlin, Evidence for partial melt at the core-mantle boundary north of Tonga from the strong scattering of seismic waves, *Nature*, *391*, 682–685, 1998.
- Weichert, D. H., and K. Whitham, Calibration of the Yellowknife seismic array with first zone explosions, *Geophys. J. R. astr. Soc.*, *18*, 461–476, 1969.
- Wen, L., and D. V. Helmberger, Ultra-low velocity zones near the core-mantle boundary from broadband PKP precursors, *Science*, *279*, 1701–1703, 1998a.
- Wen, L., and D. V. Helmberger, A two-dimensional P-SV hybrid method and its application to modeling localized structures near the core-mantle boundary, *J. Geophys. Res.*, *103*, 17,901–17,918, 1998b.
- Williams, Q., and E. J. Garnero, Seismic evidence for partial melt at the base of Earth’s mantle, *Science*, *273*, 1528–1530, 1996.

- Wu, R. S., and K. Aki, Elastic wave scattering by a random medium and the small-scale inhomogeneities in the lithosphere, *J. Geophys. Res.*, *90*, 10,261–10,273, 1985a.
- Wu, R. S., and K. Aki, Scattering characteristics of elastic waves by an elastic heterogeneity, *Geophysics*, *50*, 582–595, 1985b.
- Wyssession, M. E., and E. Okal, Regional analysis of D'' velocities from the ray parameters of diffracted P profiles, *Geophys. Res. Lett.*, *16*, 1417–1420, 1989.
- Wyssession, M. E., E. A. Okal, and C. R. Bina, The structure of the core-mantle boundary from diffracted waves, *J. Geophys. Res.*, *97*, 8749–8764, 1992.
- Wyssession, M. E., T. Lay, J. Revenaugh, Q. Williams, E. Garnero, R. Jeanloz, and L. Kellogg, The D'' discontinuity and its implications, in *The Core-Mantle Boundary Region*, edited by M. Gurnis, M. Wyssession, E. Knittle, and B. A. Buffet, AGU, Washington, D.C, 1998.
- Xu, F., and J. E. Vidale, Survey of precursors to P'P': Fine structure of mantle discontinuities, *J. Geophys. Res.*, p. doi:10.1029/2001JB000817, 2003.
- Zhao, D., Global tomographic images of mantle plumes and subducting slabs: insight into deep Earth dynamics, *Phys. Earth Planet Int.*, *146*, doi:10.1016/j.pepi.2003.07.032, 2004.
- Zhao, D., Multiscale seismic tomography and mantle dynamics, *Gondwana Research*, p. doi:10.1016/j.gr.2008.07.003, 2008.

## **Vita Auctoris**

Yan Xu was born in Kunming, Yunnan, China in March 1977. She attended Yunnan University and received Bachelor degree in computational mathematics in 1999 and Master degree in seismology in 2005.

She joined the Earthquake Administration of Yunnan Province in 1999. Then she did one year middle school teaching in Dayao, Yunnan to support the education in the poor country. In 2002, she went back to school to continue her study on seismology.